REDUCED ORDER CONSTITUTIVE MODELING OF A DIRECTIONALLY-SOLIDIFIED NICKEL-BASE SUPERALLOY

A Thesis
Presented to
The Academic Faculty

by

Sean Douglas Neal

In Partial Fulfillment
of the Requirements for the Degree
Master of Science in the
George W. Woodruff School of Mechanical Engineering

Georgia Institute of Technology
May 2013

REDUCED ORDER CONSTITUTIVE MODELING OF A DIRECTIONALLY-SOLIDIFIED NICKEL-BASE SUPERALLOY

Approved by:

Richard W. Neu, Advisor
George W. Woodruff School of Mechanical Engineering
Georgia Institute of Technology

David L. McDowell
George W. Woodruff School of Mechanical Engineering
Georgia Institute of Technology

Stephen D. Antolovich
School of Materials Science and Engineering
Georgia Institute of Technology

Date Approved: 27 February 2013

ACKNOWLEDGEMENTS

The work presented in this thesis was influenced by a number of different people. Their support has contributed beyond measure both to the completion of this work and to my development as a student, researcher, and individual. To these people, I would like to express my thanks and appreciation.

I would like to thank my advisor, Dr. Richard W. Neu, for his guidance throughout my time here at Georgia Tech. His expertise, patience, and encouragement were crucial to the completion of this thesis, and I have learned a great deal from working with him. I would also like to thank my committee members, Dr. David McDowell and Dr. Stephen Antolovich, for their assistance and insight in reviewing this thesis.

The support and friendship of my coworkers, including Mike Kirka, Patxi Fernandez-Zeilaia, Matthew Siopis, and Michael Hirsch, among many others, was greatly appreciated, as was their advice concerning research and other topics as well.

I would also like to thank the sponsor for this work, Siemens Power Generation, and the people there with whom I have interacted, specifically Mr. Phillip Gravett, Dr. Sachin Shinde, Dr. Saiganesh Iyer, Mr. Sankar Nellian, and Mr. Shahid Malik. Without their support this work would not have been possible.

Finally, I would like to thank my family for their continued encouragement and support throughout my educational career, and my friends for their understanding and support as well.

TABLE OF CONTENTS

LIST OF TABLES

LIST OF FIGURES

LIST OF SYMBOLS

α	Coefficient of thermal expansion, K^{-1} or uniaxial yield offset
α_{ij}	Backstress tensor, MPa
$\dot{\alpha}$	Increment in backstress, MPa
$\bar{\alpha}$	Effective backstress, MPa
γ	Performance ratio
$\Delta\epsilon$	Increment in strain, mm/mm
$\Delta\epsilon_1$	Increment in principal strain, mm/mm
$\Delta\epsilon^e$	Increment in elastic strain, mm/mm
$\Delta\epsilon^p$	Increment in plastic strain, mm/mm
$\Delta\epsilon^{in}_{cyc,eq}$	Change in equivalent inelastic strain range, mm/mm
$\Delta\sigma$	Increment in stress, MPa
$\Delta\sigma_1$	Increment in principal stress, MPa
ΔT	Change in absolute temperature, K
ϵ	Local strain, mm/mm or %
ϵ_a	Total strain amplitude
ϵ_{elas}	Strain from elastic analysis, mm/mm
ϵ_{ten}	tensile strain range
$\epsilon^{in}_{cyc,eq}$	Equivalent inelastic strain range, mm/mm
$\dot{\epsilon}$	increment in strain, mm/mm
ζ	Temperature dependent hardening parameter
θ	Angle from DS axis (°) or spectral parameter
κ	Threshold stress, MPa
μ	Constant used for plane strain modification
ν	Poisson's ratio
ν_T	Poisson's ratio, transverse orientation

ν_Z	Poisson's ratio, longitudinal orientation
ξ	Temperature dependent hardening parameter
π	Mathematical constant pi
$\boldsymbol{\pi}$	Tensor used in backstress evolution
$\bar{\sigma}$	Effective stress, MPa
Σ_{ij}	Symmetric viscous overstress, MPa
$\sum_\alpha \lvert\dot{\gamma}^{alpha}\rvert$	Spectral CVP function
σ_0	reference stress, MPa
$\sigma_{ij}^{PK2'}$	Second Piola Kirchoff stress, MPa
σ	Local stress, MPa
σ_{elas}	Local stress from elastic analysis, MPa
σ_u	Ultimate tensile strength, MPa
$\sigma_{vm}\rvert_{cyclic}^{max}$	Maximum cyclic Von Mises stress, MPa
σ_v	Viscous overstress, MPa
$\boldsymbol{\sigma}_{rq}^{'}$	Spectral CVP function
$\dot{\sigma}$	Increment in stress, MPa
$\phi(\sigma)$	Nonlinear function from multiaxial Neuber analysis
ϕ	First Euler angle, $^\circ$
φ_1	Second Euler angle, $^\circ$
φ_2	Third Euler angle, $^\circ$
A	Leading flow rule constant, s^{-1}
$A_1^{'}$	Flow rule constant, s^{-1}
$A_2^{'}$	Flow rule constant, s^{-1}
a_i	Arbitrary ANN output value
$\boldsymbol{B}_{kn}$	Set of coefficients for spectral function $\boldsymbol{W}_{rq}^{*}$
b_j	Arbitrary neuron bias
C_{kn}	Set of coefficients for spectral function $\boldsymbol{\sigma}_{rq}^{'}$
$\mathbf{D_i^P}$	Rate of deformation tensor
D_0	Drag stress, MPa

$\boldsymbol{D_0}$	Stretch tensor
D_{cm}	Coffin-Manson damage parameter
D_n	Inelastic increment in strain
D_{ostr}	Ostregren damage parameter
D_{swt}	Smith-Watson-Topper damage parameter
D_{zr}	Zamrik and Renauld damage parameter
D_{ostr}^{eff}	Effective Ostregren damage parameter
$\overline{D}_{ostr}^{eff}$	Averaged effective Ostregren damage parameter
$\mathbb{D}$	Averaging domain, mm^2
E	Elastic modulus, MPa
E_1	Elastic modulus in plane strain, MPa
E_L	Elastic modulus in longitudinal orientation, MPa
E_R	reference stiffness, MPa
E_T	Elastic modulus in transverse orientation, MPa
e	Nominal strain, mm/mm or %
$\boldsymbol{e_j}$	Unit vector in orthogonal direction j
$\mathbf{F}$	Deformation gradient tensor
F^{θ}, F_{ij}^{θ}	Thermal deformation gradient tensor
$\mathbf{F^e}$	Elastic deformation gradient
$\mathbf{F^p}$	Plastic deformation gradient
G	Shear Modulus, MPa
G_L	Shear Modulus in longitudinal direction, MPa
G_{kn}	Set of coefficients for spectral function $\sum_{\alpha}\|\dot{\gamma}^{alpha}\|$
g^p	Spectral function variable
H	Backstress hardening paramete
$\boldsymbol{H}$	Elastic compliance tensor
K	Threshold stress or Ramberg-Osgood Parameter, MPa
K'	Cyclic Ramberg-Osgood Parameter
K_{σ}	Stress concentration factor

K_ϵ	Strain concentration factor
K_c	fracture toughness, MPa$\sqrt{m}$
K_t	Theoretical stress concentration factor
K_{th}	Threshold for crack propagation, MPa$\sqrt{m}$
K_1	Drag stress, MPa
K_2	Drag stress, MPa
L	Backstress hardening parameter or characteristic length
$\boldsymbol{L}$	Velocity gradient tensor
$\mathbf{M}$	Effective stress integrity basis dyad
MRE	Mean relative error
MSE	Mean squared error
MSE_{reg}	Modified performance function metric
MSW	Mean sum of squares of connection weights
m	Static thermal recovery exponent
$\boldsymbol{M}$	Anisotropy tensor of Hill's parameters
$\mathbf{N}$	Unit vector in the direction of plastic strain
N	Number of targets, points, etc. in summation
N_f	Number of cycles to failure
N_f^{creep}	Number of cycles to failure from creep damage
N_f^{fat}	Number of cycles to failure from fatigue damage
N_f^{ox}	Number of cycles to failure from oxidation damage
n	Strain rate sensitivity exponent
n'	Cyclic strain rate sensitivity exponent
p_1	Flow rule exponent
p_2	Flow rule exponent
$\dot{p}$	Increment in plastic strain, mm/mm or %
Q	Activation energy for dislocation bypass of obstacles, kJ/mol
R	Gas constant, kJ/mol K
R_α	Static thermal recovery constant

S	Nominal stress, MPa
T	Absolute temperature, K
t_i	Arbitrary target value
v_j	Arbitrary neuron output
$\boldsymbol{W}^*_{rq}$	Spectral CVP function
w_{ij}	Arbitrary synaptic weight
y_j	Arbitrary neuron output

LIST OF ABBREVIATIONS

ANN	Artificial Neural Network
BC	Boundary Condition
BCC	Body Centered Cubic
CAE	Computer Aided Engineering
CTE	Coefficient of Thermal Expansion
CVP	Crystal Visco-Plasticity
DS	Directionally Solidified
FCC	Face Centered Cubic
FE, FEA	Finite Element (Analysis)
GB	Grain Boundary
IP	In-Phase
ISV	Internal State Variable
L	Longitudinal
LCF	Low Cycle Fatigue
OP	Out-of-Phase
R-O	Ramberg-Osgood
RPM	Revolutions Per Minute
RVE	Representative Volume Element
Sim.	Simulation
T	Transverse
Temp.	Temperature
TIVP	Transversely Isotropic Visco-Plasticity
TMF	Thermomechanical Fatigue
UMAT	User -Defined Material Subroutine
YS	Yield Strength

1-D	One-dimensional
3-D	Three-dimensional

SUMMARY

Hot section components of land-based gas turbines are subject to extremely harsh, high temperature environments and require the use of advanced materials. Directionally solidified nickel base superalloys are often chosen as materials for these hot section components due to their excellent creep resistance and fatigue properties at high temperatures. These blades undergo complex thermomechanical loading conditions throughout their service life, and the influences of blade geometry and variable operation makes life prediction difficult. Accurate predictions of material response under thermomechanical loading conditions is essential for life prediction of these components. Complex physics-based crystal viscoplasticity (CVP) models are often used to capture the behavior of Ni-base superalloys. While accurate, these models are computationally expensive and are not suitable for all phases of design.

This work involves the calibration of a reduced-order, macroscale, transversely isotropic viscoplasticity (TIVP) model to a directionally solidified Ni-base superalloy. The unified model is capable of capturing isothermal and thermomechanical responses in addition to secondary creep behavior over the temperature range 20-1050°C. An extreme reduced order microstructure-sensitive constitutive model is also developed with an artificial neural network (ANN) to provide a rapid first-order approximation of material response under thermomechanical loading conditions. Based on uniaxial isothermal training data from more complex crystal viscoplasticity and transversely isotropic viscoplasticity models fit to a simple 1-D Ramberg-Osgood relation, the ANN model is able to generate Ramberg Osgood parameters at any arbitrary temperature, strain rate, and material orientation from the DS axis within the domain of the training data. These microstructure-sensitive parameters can then be used in a Neuber-type analysis to predict local stresses and strains at stress concentrators of components.

CHAPTER I

INTRODUCTION

1.1 Motivation

For decades, land-based gas turbines have been employed in the energy sector and are a convenient choice for numerous power generation applications. In these turbines, combustion of a compressed air/fuel mixture forces superheated gases through different stages of blade components, which then turn a rotor connected to the power transmission grid. Very high operating temperatures are desired in order to increase the thermal efficiency of these systems, which leads to harsh operating environments for turbine components. Blades in the hot section of the turbine must be able to withstand these extreme conditions. Because of their excellent strength retention and creep resistance at high temperatures, among other desirable qualities, directionally solidified (DS) nickel-base superalloys are often selected as materials for these components. An example of a gas turbine shaft with blade components attached is shown in Figure 1.1.

Figure 1.1: A partially constructed land based gas turbine [1]

1.2 CM247LC-DS Material Specifications

Directionally solidified Ni-base superalloys have far fewer transverse grain boundaries with respect to the direction of solidification when compared to their polycrystalline (also called equiaxed) counterparts. This reduction in tranverse grain boundaries leads to better creep resistance, and the resulting lower modulus in this direction allows for better fatigue resistance at high temperatures [2]. Developed by the Cannon-Muskegon Corporation [3], CM247LC-DS is descended from a parent alloy Mar-M247 when an effort was made to reduce cracking at grain boundaries through lowering the carbon content of the alloy. The average chemical composition of CM247LC-DS is given in Table 1.1.

Table 1.1: Chemical composition of CM247LC-DS

	Composition by Weight Percent											
Material	Al	B	C	Co	Cr	Hf	Mo	Ta	Ti	W	Zr	Ni
CM247LC-DS	5.6	0.015	0.07	9.2	8.1	1.4	0.5	3.2	0.7	9.5	0.015	Bal.

CM247LC-DS is a two-phase material consisting of hard FCC Ni_3Al (γ') phase precipitates in a softer γ phase FCC matrix comprised mostly of Ni. This structure is shown in Figure 1.3.

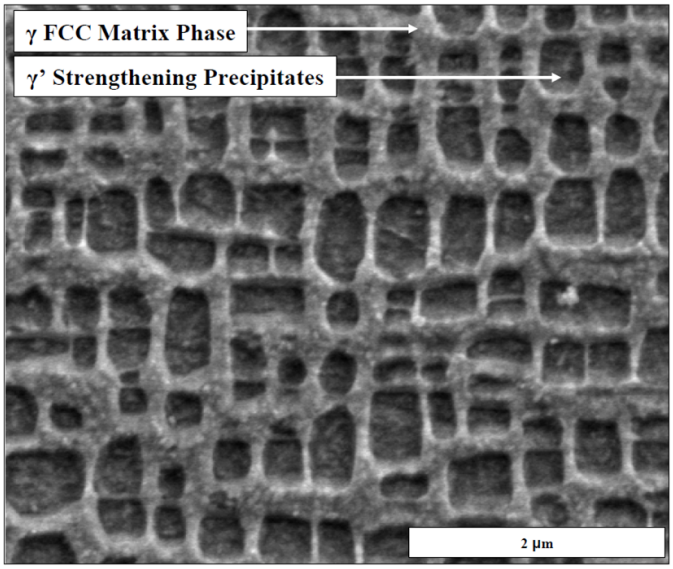

Figure 1.2: SEM image of two-phase structure of CM247LC-DS [4]

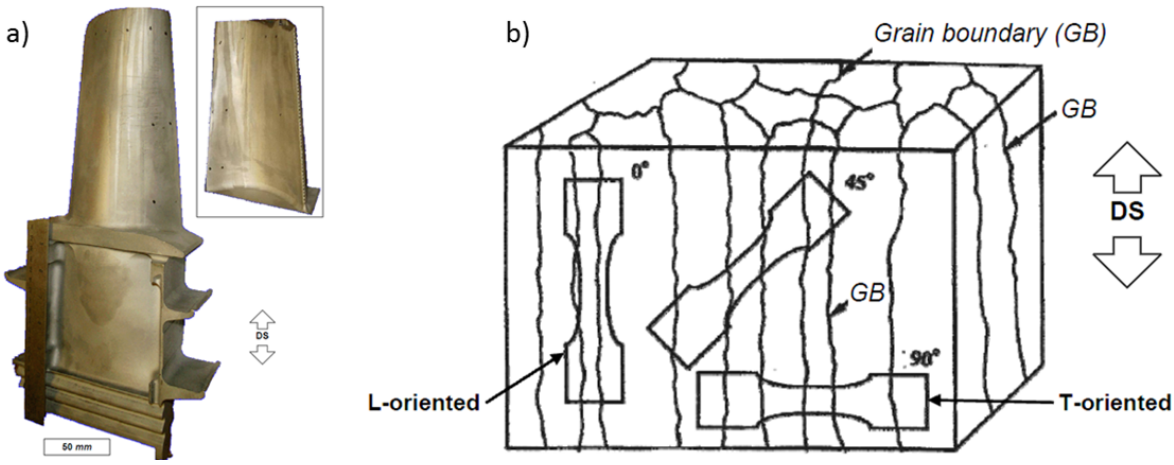

Figure 1.3: (a) A DS turbine blade and (b) convention for off-axis specimens [5]

For design and life prediction of these components, it is essential to be able to predict material behavior under a variety of conditions. Of particular interest is the material response under thermomechanical fatigue (TMF) conditions, in which both temperature and load change simultaneously. These conditions are experienced by blade components during startup and shutdown, where temperature variations across the airfoil have a detrimental effect by inducing thermal cycling in sections of the component. Both in-phase (IP) and out-of-phase (OP) TMF loading conditions are experienced by different sections of the component during operation. In addition, it is also important to predict creep behavior at higher temperatures, since at base operating conditions the components are subjected to centrifugal stresses arising from the 3000 or 3600 RPM required to provide power to the transmission grid. Since the grain size is relatively large (0.5 mm), a crystal viscoplasticity (CVP) constitutive model that explicitly considers 3-D grain structure is ideal for capturing the important features of the microstructure.

However, these models are computationally expensive and, in general, are not suitable for design analysis. The aim of this project is to evaluate more computationally efficient approaches that still capture the important microstructural features which govern the response.

1.3 Research Objectives

The research presented in this thesis will focus on exploring reduced order methods of predicting Ni-base superalloy behavior under TMF loading conditions and making comparisons between these reduced order constitutive models and ones that include additional microstructural attributes, but are computationally expensive. The specific objectives of this research are as follows:

1. **Calibrate a transversely isotropic viscoplasticity (TIVP) model to capture the response of a DS Ni-base superalloy for isothermal, thermomechanical, and creep conditions.** Developed previously by Shenoy et al. [6], this continuum-based model is much less computationally expensive than crystal viscoplasticity (CVP) models which are currently used. Since the TIVP model is a unified creep-plasticity model, it is much more representative of material behavior and preferable to built-in finite element models in which creep and plasticity are considered separately while still providing significant improvements in computation time.

2. **Develop an extreme reduced order constitutive model to rapidly approximate DS Ni-base superalloy behavior under a variety of conditions.** An extreme reduced order model consisting of a feedforward artificial neural network (ANN) is intended to approximate the local response almost instantly, which could be used in systems level design or life model. This model would be trained using the output from a CVP model and approximate material response under a range of temperatures, strain rates, and material grain orientations by predicting parameters for a much simpler analytical model. The effects of temperature, strain rate, and orientation would be captured through the model parameters themselves.

3. **Compare the reduced order and extreme reduced order constitutive models to the more complex crystal viscoplasticity (CVP) model in terms of relative accuracy and computational expense.** It is important to understand the comparative performance of each of the three material models in terms of both

accuracy and computational expense in order to determine their prescribed usage in component and systems level design.

1.4 Thesis Overview

Chapter 2 is a background and literature review on constitutive modeling of Ni-base superalloys and the utlization of the function fitting capabilities of feedforward artificial neural networks in the materials science field. Chapter 3 is an overview of a transversely isotropic viscoplasticity model and provides details pertaining to its calibration to CM247LC-DS and verification/validation cases. Chapter 4 discusses the development of an extreme reduced order microstructure-sensitive constitutive model. Chapters 6 and 7 conclude the thesis and provide suggestions for future work, respectively.

CHAPTER II

BACKGROUND

Accurate prediction of high temperature and thermomechanical behavior of directionally solidified Ni-base superalloys is essential for reliable life prediction of turbine components made from these materials. Life prediction of these components can be a nontrivial task due to the variety of damage mechanisms present under thermomechanical fatigue conditions, which are primarily fatigue, creep, and environmental effects [5]. These have been previously studied [4,5,7–9] and the extent of each varies depending upon the nature of test conditions [4]. The methods presented in this research deal primarily with life prediction through predicting the cyclic response and then correlating to life. Included here is an overview of life prediction methods for components subjected to thermomechanical fatigue, as well as methods to account for stress concentrators and non-local computational approaches. Previous work on reduced order modeling techniques is presented also.

2.1 Stress Concentration Effects

In addition to numerous empirical approaches suggested to account for notch effects, classic analytical approaches to predicting the local stresses and strains for notched components involve a relation between linear elastic pseudo stresses/strains (values that are from a purely elastic analysis) and actual elastic-plastic stresses/strains at the notch. One such relation was proposed by Neuber [10]. Known as Neuber's rule, it is given as

$$\sigma_{elas}\epsilon_{elas} = \sigma\epsilon \tag{2.1}$$

where σ_{elas} and ϵ_{elas} are the linear elastic stress and strain, respectively, and σ and ϵ are the local stress and strain, respectively. A geometrical interpretation of this relation is that the area under the theoretical linear elastic stress-strain curve (a triangular area) is equivalent to the area under a second triangle formed by the origin, the point on the true

local stress-strain curve [ϵ,σ], and the point [ϵ,0]. This is depicted in Figure 2.1.

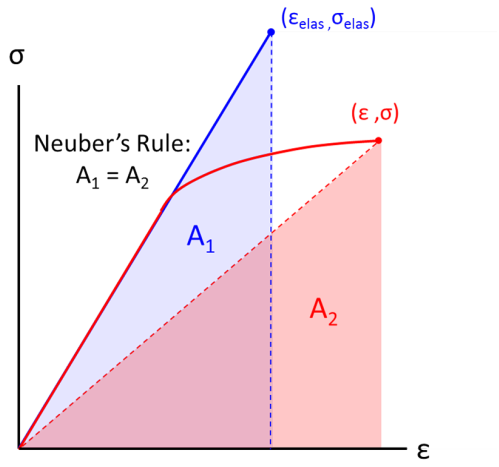

Figure 2.1: Geometrical interpretation of Neuber's Rule

Neuber showed that the stress concentration factor can be expressed as

$$K_t = \sqrt{K_\sigma K_\epsilon} \tag{2.2}$$

where the theoretical stress concentration factor, K_t, is the geometric average of the stress concentration factor, K_σ, and the strain concentration factor, K_ϵ. The stress concentration factor and strain concentration factor are defined

$$K_\sigma = \frac{\sigma}{S} \tag{2.3}$$

and

$$K_\epsilon = \frac{\epsilon}{e} \tag{2.4}$$

respectively, where σ is the local stress at the notch feature, S is the nominal stress, ϵ is the local strain at the notch, and e is the nominal strain. Using this relation, Equation 2.2 can be rewritten as in Equation 2.5.

$$K_t^2 Se = \sigma\epsilon \tag{2.5}$$

Using a substitution with the stress concentration factor definition and assuming nominal elastic behavior, Equation 2.5 can be rewritten as

$$\frac{\sigma_{elas}^2}{E} = \sigma\epsilon \tag{2.6}$$

where σ_{elas} is the local stress using an elastic analysis. Using the simple Ramberg-Osgood relation [11] [12]

$$\epsilon = \frac{\sigma}{E} + \left(\frac{\sigma}{K}\right)^{\frac{1}{n}} \tag{2.7}$$

where E is the elastic modulus, K is a strength coefficient, and n is an exponent capturing strain hardening behavior, Equation 2.6 can be rewritten again as

$$\frac{\sigma_{elas}^2}{E} = \sigma\left[\frac{\sigma}{E} + \left(\frac{\sigma}{K}\right)^{\frac{1}{n}}\right] \tag{2.8}$$

Using this relation, the value of σ can be solved through iteration, and then the value of ϵ can be computed using Equation 2.6.

Alternatively, a relation proposed by Molski and Glinka [13] can be used instead of Equation 2.8.

$$\frac{\sigma_{elas}^2}{E} = \sigma\left[\frac{\sigma}{E} + \frac{2}{1+n}\left(\frac{\sigma}{K}\right)^{\frac{1}{n}}\right] \tag{2.9}$$

This approach is generally less conservative than a Neuber relation and assumes the magnitude of the strain energy density near the elastic-inelastic notch root is equivalent to nominally elastic behavior [14]. A geometrical interpretation of Glinka's rule is shown in Figure 2.2, where the area under the theoretical linear elastic stress-strain curve (the strain energy density) is equal to the area under the true stress-strain curve.

It has been shown that the Glinka or modified Glinka relation gives a better approximation of stresses and strains at notch roots than Neuber's relation, in the case of plane strain, although the Neuber relation is more conservative for LCF conditions [15]. Both

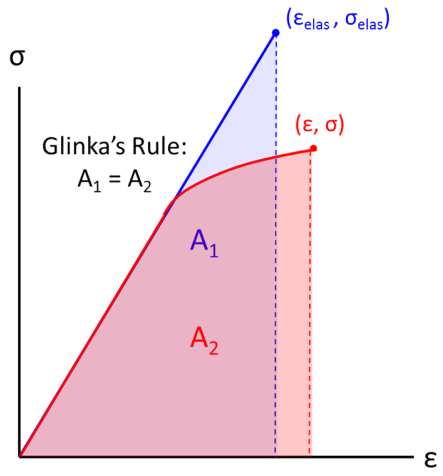

Figure 2.2: Geometrical interpretation of Glinka's Rule

relations may be extended to cyclic stress-strain curves by replacing the monotonic form of the Ramberg-Osgood equation with the cyclic, incremental form

$$\Delta\epsilon = \frac{\Delta\sigma}{E} + 2\left(\frac{\Delta\sigma}{2K'}\right)^{\frac{1}{n'}} \tag{2.10}$$

where $\Delta\epsilon$ is the increment in strain, $\Delta\sigma$ is the increment in stress, and K' and n' are the cyclic strength coefficient and cyclic strain hardening exponent, respectively. Neuber's relation now is given by

$$\frac{\Delta\sigma_{elas}^2}{2E} = \Delta\sigma\left[\frac{\Delta\sigma}{2E} + \left(\frac{\Delta\sigma}{2K'}\right)^{\frac{1}{n'}}\right] \tag{2.11}$$

and Glinka's relation is now

$$\frac{\Delta\sigma_{elas}^2}{2E} = \Delta\sigma\left[\frac{\Delta\sigma}{2E} + \frac{2}{1+n'}\left(\frac{\Delta\sigma}{2K'}\right)^{\frac{1}{n'}}\right] \tag{2.12}$$

Both Neuber's Rule and Glinka's Rule provide a method to analytically determine the local stresses and strains at a notch root, although approximating these stresses and strains without a known stress concentration factor may be difficult. Finite element methods may be used to determine the local elastic pseudo-stress at a region of interest and avoid the use of a stress concentration factor altogether. Moore [16] developed a model for high

temperature LCF of a DS Ni-base superalloy that incorporated a multiaxial Neuber model from the work of Mucke and Bernhardi [17] based on a multiaxial Ramberg-Osgood relation generalized from the simple 1-D relation

$$\epsilon = \frac{\sigma}{E} + \alpha \left(\frac{\sigma}{\sigma_0} \right)^{n-1} \sigma \tag{2.13}$$

This form of the Ramberg-Osgood is common and is used as the built-in classical plasticity model in ABAQUS [18]. A 3-D generalization of this relation is given by

$$\boldsymbol{\epsilon} = \mathbf{H} : \boldsymbol{\sigma} + \frac{\alpha}{E_R} \left(\frac{\sigma_{eq}}{\sigma_0} \right)^{n-1} \mathbf{M} : \boldsymbol{\sigma}^{\boldsymbol{dev}} \tag{2.14}$$

The multiaxial Neuber model is then expressed as the nonlinear function $\phi(\sigma)$ given as

$$\phi(\sigma) := \sigma_{elas}^2 - \sigma^2 \left[1 + \frac{\mathbf{D}^{*\mathbf{dev}} : \mathbf{M} : \mathbf{D}^{*\mathbf{dev}}}{\mathbf{D}^{*\mathbf{dev}} : \mathbf{H} : \mathbf{D}^{*\mathbf{dev}}} \frac{\alpha}{E_R} \left(\frac{\sqrt{\mathbf{D}^{*\mathbf{dev}} : \mathbf{M} : \mathbf{D}^{*\mathbf{dev}} \sigma}}{\sigma_0} \right)^{n-1} \right] = 0 \tag{2.15}$$

where $\mathbf{D}^{*\mathbf{dev}}$ is the unit direction tensor associated with deviatoric stresses, $\mathbf{M}$ is the anisotropy tensor of Hill's parameters, $\mathbf{H}$ is the elastic compliance tensor, α is the yield offset corresponding to the uniaxial case, E_R is a suitable reference stiffness, and σ_0 is the reference stress. Details of its derivation can be gathered from Moore [16] with additional details from Mucke and Bernhardi [17]. Equation 2.15 can be solved through iteration for σ, whose value may be used to determine the elastic-plastic stress state through the unit direction tensor and the strain state through the multiaxial Ramberg-Osgood relation.

To account for time-dependent loads and their effect on the local response at a notch, Chaudonneret and Culie [19] proposed a method based on a differential version of Neuber's rule, given by

$$\dot{\sigma} = \frac{1}{2\sigma + E\epsilon_p} \left(2\sigma_{elas} \dot{\sigma}_{elas} - E\sigma\epsilon_p \right) \tag{2.16}$$

where $\dot{\sigma}$ is the increment in stress at the notch, ϵ^p is the plastic strain at the notch, and $\dot{\sigma}_{elas}$ is the increment in stress from the elastic analysis. The authors used a unidimensional

flow rule for plastic strain with evolution equations for backstress and drag stress in the manner of Chaboche [20]. This method was shown to give reasonably good results for creep and fatigue, in addtion to cycles with holds. For multiaxial loading conditions, the second invariants of the deviatoric stress and strain tensors were used to characterize the state of stress and deformation.

Moftakhar et al. used a strain energy density type method to predict time-dependent stresses and strains at notches under creep [21] as well as time-dependent stresses and strains under generalized multiaxial conditions [22]. These methods involve the use of strain energy density concentration factors to relate nominal stresses and strains to local stresses and strains. This method and other time-dependent notch analysis methods are discussed in detail by Moore [16].

2.2 TMF Life Prediction

Thermomechanical loading conditions in blade components arise from both applied loads and thermal gradients present in the component during engine operation. TMF is generally classified as either in-phase (IP) or out-of-phase (OP) and simple situations are tested in the laboratory, usually with linear waveforms, although endless combinations of nonlinear temperature and load changes are possible. An example of both IP and OP TMF waveforms is given in Figure 2.3.

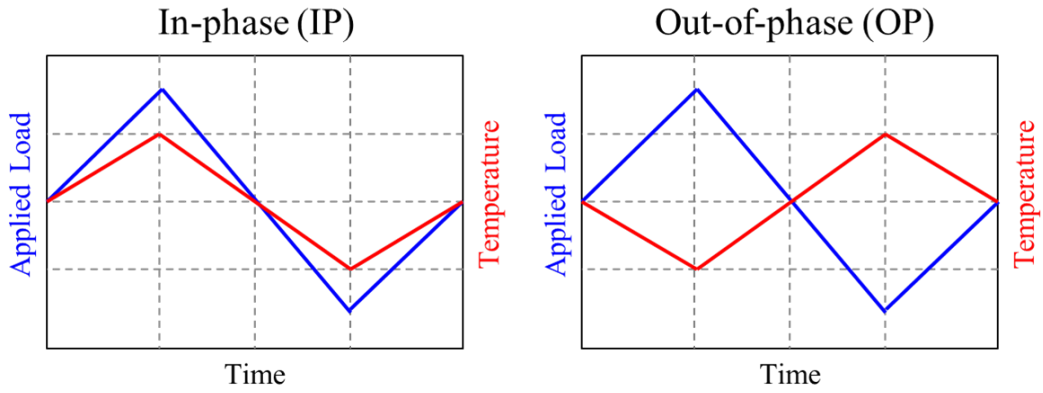

Figure 2.3: Out-of-phase (OP) and in-phase (IP) TMF cycles with linear waveforms [23]

For low-cycle fatigue (LCF) conditions, the classic Coffin-Manson relation [24] is often used for life prediction and serves as the basis for numerous life models. Its associated damage parameter is given by

$$D_{cm} = \Delta\epsilon_p = f(N_f) \tag{2.17}$$

where $\Delta\epsilon_p$ is the inelastic strain range and N_f is the number of cycles to failure. In this relation, only the inelastic strain range, $\Delta\epsilon_p$ is used to predict life. For TMF life prediction, an energy-based approach was proposed by Ostergren [25] with a damage parameter given by

$$D_{ostr} = \Delta\epsilon_p\sigma_{max} = f(N_f) \tag{2.18}$$

where σ_{max} is the maximum stress seen by the component in the half cycle. Mean stress effects are captured by adding the σ_{max} parameter [4] in the model, which assumes crack propagation is the driving force for failure in low cycle fatigue [25]. Zamrik and Renauld [26] further modified the Ostergren model by normalizing the product of the maximum tensile stress and strain ranges at midlife cycle by the product of the ultimate strength and strain to failure at the OP TMF cycle minimum temperature. The damage parameter was then term defined as

$$D_{zr} = \Delta W = \frac{\sigma_{max}\epsilon_{ten}}{\sigma_u\epsilon_f} \tag{2.19}$$

where ΔW is the dimensionless damage term, σ_{max} is the maximum tensile stress range at midlife, ϵ_{ten} is the tensile strain range at midlife, σ_u is the ultimate tensile strength, and ϵ_f is the strain to failure. This term was then fitted to a power law relationship to predict cycles to crack initiation.

The weakness of these types of models is that isothermal LCF data does not take into account the presence of other damage mechanisms under TMF conditions. McDowell et al. [27] suggested that life models which consider damage from fatigue, creep, and oxidation

explicitly were more promising than models which either included the effects of oxidation only implicitly or ignored them altogether. A more comprehensive linear accumulation model for high temperature damage for TMF was proposed by Neu and Sehitoglu [7,28,29] which incorporated the effects of oxidation and creep, in addition to fatigue. This model is given as

$$\frac{1}{N_f} = \frac{1}{N_f^{fat}} + \frac{1}{N_f^{ox}} + \frac{1}{N_f^{creep}} \tag{2.20}$$

where the superscript of each N_f term denotes the mechanism with which it is associated. For fatigue, the N_f^{fat} term is given by a relation typical of strain life in which the damage parameter consists of one half of the mechanical strain range. In work done with DS GTD-111, Gordon [5] modified this fatigue life term further to incorporate the effects of material orientation from the DS axis through a shape function.

Neu and Sehitoglu [29] used a creep damage term that is a function of both effective stress and hydrostatic stress, with an Arrhenius-type relation to include temperature effects. Gordon [5] used a different relation based on the Larson-Miller Parameter [30]. Kupkovits [4] extended this sort of definition to TMF conditions by modifying a leading constant to account for temperature changes through taking an average value using integration over time. An additional constant was added to account for phasing using a functional form previously used by Neu and Sehitoglu [29]. It is important to note that one limitation of this sort of creep model is that it decouples creep from fatigue. Thus it cannot capture stress relaxation effects or changes in material compliance with temperature [4].

For environmental fatigue, Neu and Sehitoglu [29] used a term based on the contribution of crack formation and growth in the oxide layer that accounted for both the length at which damage from the environment lags behind the crack tip and the ductility within the envinronmentally affected zone. Gordon [5] used an environmental fatigue damage term that accounted for orientation effects through a shape function as before, in addition to a constant to incorporate the effects of phasing and constants to capture high temperature

dwell oxidation. Domas and Antolovich [31] developed a high temperature LCF life prediction model based on oxidation kinetics for smooth specimens of a Ni-base superalloy. This model was later extended to life predictions of notched specimens by incorporating a power series approximation of the stress distribution in the notch region and showed good correlation with experimental data.

2.3 Non-local Methods

Methods that use finite element analysis are an alternative means of predicting component life. FE analysis has allowed non-local methods that take into account the stress or strain gradients of notches to be used, especially for cases where the stress concentration factor is unknown. These methods have been shown to yield better fatigue life predictions under LCF conditions [32].

In addition, the theory of critical distances (TCD) is a very powerful and practical theory and is well-described by Taylor [33]. Variations of this method have been used for over 50 years, having been suggested by Neuber [10] and Peterson [34]. This approach utilize a characteristic length scale derived from the fracture toughness as

$$L = \frac{1}{\pi}\left(\frac{K_c}{\sigma_u}\right)^2 \tag{2.21}$$

where K_c is the fracture toughness and σ_u is the tensile strength. For fatigue crack formation, it is more relevant to use a charateristic length based on threshold values

$$L = \frac{1}{\pi}\left(\frac{K_{th}}{\sigma_0}\right)^2 \tag{2.22}$$

where K_{th} is the threshold for crack propagation and σ_0 is the fatigue limit. Applications of this method include the line method, the first critical distance method invented and used by Neuber [10] and the point method suggested by Peterson [34]. In this method, the stress for failure is determined by averaging the stress values along a line a certain distance from the notch root, theoretically shown to be $2L$. Area and volume integrals have also been suggested [33]. More recently, TCD methods have been used to predict life in

medium cycle fatigue [35] and LCF by using strain as the controlling parameter [36]. Domas and Antolovich [37] developed an integrated local energy density (ILED) approach for life prediction of notched LCF specimens which utilized an average strain energy density for the notch region.

Another approach is the critical plane approach, which uses the material plane with maximum shear strain and the stresses normal to this plane in conjunction with other criteria to predict component life. This approach and others have been studied extensively by Fatemi and Socie [38]. Moore [16] provides a good overview of typical critical plane parameters and used this sort of method in his life model by using a Smith-Watson-Topper (SWT) damage parameter defined as

$$D_{swt} = \sigma_{max}\epsilon_a \tag{2.23}$$

where σ_{max} is the maximum normal stress resolved on the critical plane and ϵ_a is the total strain amplitude resolved on the critical plane. A critical value of this parameter is used to captures the aniotropic material resistance. Kupkovits [4] showed that the actual damage mechanisms encountered during TMF tests were not accounted for in Moore's simplified model.

Fernandez-Zelaia and Neu [39] [23] used a nonlocal method of area averaging to predict lives for notched specimens under OP TMF. In this case an effective Ostergren parameter was used, defined as

$$D_{ostr}^{eff} = \Delta\epsilon_{cyc,eq}^{in}\sigma_{vm}|_{cyclic}^{max} \tag{2.24}$$

where $\epsilon_{cyc,eq}^{in}$ is the equivalent inelastic strain range and $\sigma_{vm}|_{cyclic}^{max}$ is the maximum value of the Von Mises stress occurring in tension over one cycle. The average value of this parameter was taken over an invariant domain as

$$\overline{D}_{ostr}^{eff} = \frac{1}{\mathbb{D}}\int_{\mathbb{D}} D_{ostr}^{eff}|_{cyclic} d\mathbb{D} \tag{2.25}$$

where $\mathbb{D}$ is the domain over which the parameter was averaged. The domain was taken as a critical area since 1) cracks were found to initiate at some distance from the notch root and 2) the location of maximum Von Mises stresses and cyclic inelastic strains were found at some distance away from the notch root depending on notch severity [39]. This method of averaging over an invariant area was demonstrated to work reasonably well for both areas taken using surface sweep and circular sweep paths. Averaging over a fixed area took into account the stress and strain gradients present near the notch, and the area was selected such that the averaged effective Ostergren parameters for $K_t = 2$ and $K_t = 3$ were nearly identical, which was consistent with experimental observation [39].

2.4 Reduced Order Constitutive Modeling Techniques

Crystal viscoplasticity models are advanced materials models that are useful for capturing complex behavior of metals, including time and temperature dependent effects. These models relate observed macroscopic deformation to deformation occurring at a microscopic/atominstic scale by explicitly taking into account three-dimensional grain structure and individual slip systems of the material. A background on CVP models can be gathered from McGinty [40] Shenoy [41]. McDowell [42] also provides a thorough background on CVP models and recent advances in crystal plasticity modeling.

The basis for this type of model is a multiplicative decomposition of the deformation gradient [43] given as follows:

$$\mathbf{F} = \mathbf{F^e} \cdot \mathbf{F^p} \tag{2.26}$$

where $\mathbf{F}$ is the deformation gradient tensor and $\mathbf{F^e}$ and $\mathbf{F^p}$ are corresponding elastic and plastic deformation gradients, respectively. This is shown graphically in Figure 2.4.

Since the flow rule for this sort of model is formulated in terms of shearing rates on active slip systems and must be evaluated on each one, the computational expense related to implementing a CVP model is one of its primary drawbacks. Kalidindi et al. [44] and Knezevic et al. [45, 46] have done extensive work in capturing crystal plasticity through spectral frameworks. In one approach, discrete Fourier transforms (DFTs) are used to interpolate

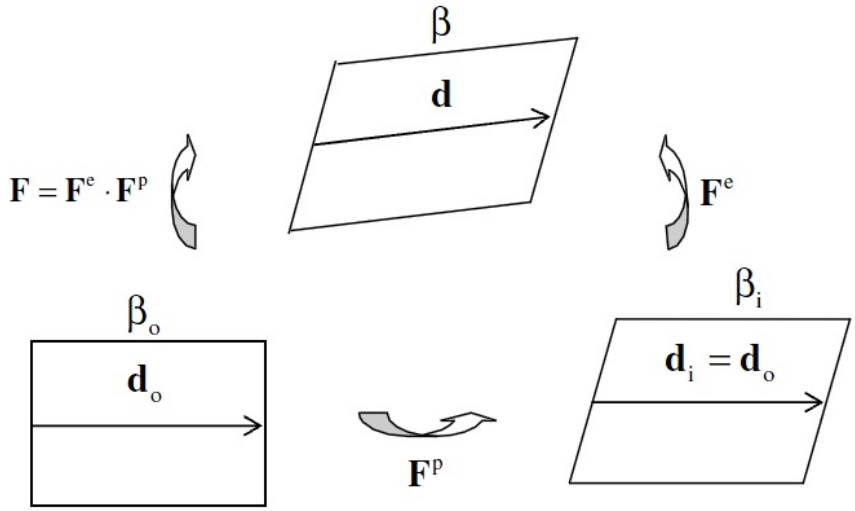

Figure 2.4: Decomposition of the deformation gradient tensor [6]

functions that relate stresses, lattice spins, and strain hardening to lattice orientation and mode of deformation [45]. This was accomplished by decomposing the velocity gradient tensor into a sum of symmetric stretching and antisymmetric spin components,

$$\mathbf{L} = \dot{\epsilon}\mathbf{D_0} + \mathbf{W}^{app} \qquad \mathbf{D_0} = \sum_{j=1}^{3} D_j \mathbf{e}_j^p \otimes \mathbf{e}_j^p \qquad \dot{\epsilon} = |\mathbf{D}| \tag{2.27}$$

The stretch tensor $\mathbf{D}$ was then parameterized using a single angular variable θ

$$D_1 = \sqrt{\frac{2}{3}}\cos(\theta - \frac{\pi}{3}), D_2 = \sqrt{\frac{2}{3}}\cos(\theta + \frac{\pi}{3}), D_3 = -\sqrt{\frac{2}{3}}\cos(\theta) \tag{2.28}$$

This method was used as the basis for constructing the spectral database, along with a crystal orientation parameter. DFTs were then used to construct spectral representations of three functions $\boldsymbol{\sigma}'(g^p, \theta)$, $\mathbf{W}^*(g^p, \theta)$ and $\Sigma_\alpha|\dot{\gamma}^{alpha}|(g^p, \theta)$ that captured the rigid-viscoplastic crystal plasticity solutions and are given as

$$\mathbf{W}^*{}_{rq} = \dot{\epsilon}\frac{1}{N_g N_\theta}\sum_k \sum_n \mathbf{B}_{kn} e^{\frac{2\pi i k r}{N_g}} e^{\frac{2\pi i n q}{N_\theta}} + \mathbf{W}^{app} \tag{2.29}$$

$$\boldsymbol{\sigma}'{}_{rq} = s|\dot{\epsilon}|^m sgn(\dot{\epsilon})\frac{1}{N_g N_\theta}\sum_k \mathbf{C}_{kn} e^{\frac{2\pi i k r}{N_g}} e^{\frac{2\pi i n q}{N_\theta}} \tag{2.30}$$

$$\left(\sum_{\alpha}|\dot{\gamma}^{alpha}|\right) = |\dot{\epsilon}|\frac{1}{N_g N_\theta}\sum_{k} G_{kn} e^{\frac{2\pi i k r}{N_g}} e^{\frac{2\pi i n q}{N_\theta}} \tag{2.31}$$

where r and q define the points of the grid upon which the values are stored, and $\mathbf{B}_{kn}$, $\mathbf{C}_{kn}$, and G_{kn} form the set of coefficients. Additional details related to the calculation of these tranforms can be found in Knezevic et al. [45]. The crystal plasticity equations were not solved directly; rather, the approximate solutions for any arbitrary deformation mode and lattice orientation were obtained by evaluating the dominant DFTs at points of interpolation on the $r - q$ grid. This approach of using spectral representation of crystal plasticity equations was shown to drastically decrease the computation time by two orders of magnitude when compared to conventional implementations. Limitations of this relatively new approach are that it has not been extended beyond isotropic plasticity. In addition, this method has not been extended to account for changes in temperature.

Other attempts at reduced order constitutive models have involved the use of artificial neural networks (ANNs) to model material behavior. An ANN consists of group of processing elements called neurons (also called nodes or units) which are arranged in successive layers and receive inputs from other neurons as the signal works forward from an input layer to an output layer. A typical feedforward ANN layout is shown in Figure 4.2.

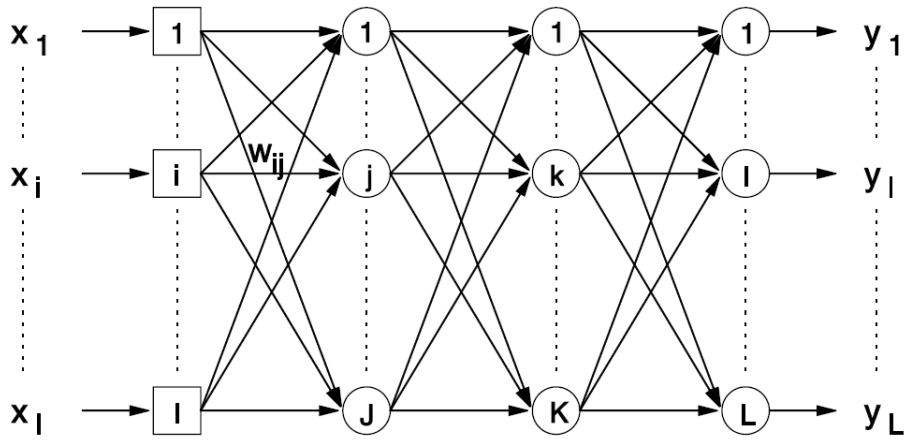

Figure 2.5: A typical multilayer feedforward artificial neural network layout [47]

where $\mathbf{X_i}$ are the inputs to the ANN, $\mathbf{W_{ij}}$ are the connection (synaptic) weights between neurons, and $\mathbf{Y_i}$ are the outputs from the ANN. These networks are able to automatically produce nonlinear mappings between multiple input and output data through learning from a so-called training set, and are able to generalize well for new data not appearing in the training set while requiring minimal computational resources [48]. A thorough background on ANN research is summarized by Anderson [49] and Lau [50].

Jung and Ghaboussi [51] used an ANN as a constitutive model for a simulated viscoelastic solid (using a standard solid model for viscoelasticity) in which the ANN gave the increment in stress after being given the stress and strain values from the previous increment and the increment in strain. Al-Haik et al. [52, 53] used an ANN as a constitutive model to capture the viscoplastic behavior of a carbon-fiber/polymer matrix composite under thermomechanical loading conditions. Liang and Chandrashekhara [54] also used an ANN as a constitutive model for elastomeric foams. The neural network was used to implicitly define the strain energy function by first being given the first and second deviatoric strain invariants and the total volume ratio, and returning the value of the strain energy function. A drawback to this sort of approach is it requires extensive amounts of experimental data to be used for training, which can be expensive and time-consuming.

ANNs have also been used to predict parameters of simple constitutive relations, such as in the work of Ghajar et al. [55] where an ANN was used to predict the Ramberg-Osgood parameters of various types of steels given material properties. Gupta et al. [56] used an ANN to model the high temperature creep behavior of a rotating composite Al-SiC_p disk. In this case, the ANN was used to correlate radial and tangential stresses and strain rates to temperature, radial distance, particle size and particle content of reinforcement, an example of correlating observed behavior at the macroscale with a parameter characterizing material at a smaller scale. Shenoy et al. [57] combined these sorts of approaches and used an artificial neural network to predict parameters of a macroscale model given microstructural parameters. The training set was comprised of simulations from a more complex crystal plasticity model, where the response was fitted to a simpler macroscale model with two-term flow rule from Chaboche [20] for an intially isotropic material given as

$$D^n = \left\{ A_1^{'} \left\langle \frac{\sigma_v - \kappa}{K_1} \right\rangle^{p_1} + A_2^{'} \left\langle \frac{\sigma_v}{K_2} \right\rangle^{p_2} \right\} sgn(\sigma - \tilde{\Omega}) \tag{2.32}$$

where D^n is the inelastic strain increment, $A_1^{'}$ and $A_2^{'}$ are temperature dependent viscosity coefficients, K_1 and K_2 are drag stresses, p_1 and p_2 are hardening exponents, κ is the threshold stress, and σ_v is the viscous overstress. Further details may be found in Shenoy et al. [57]. This process was repeated for each microstruture, and the microstructural parameters and their corresponding macroscale model parameters were used as a training set for the ANN. The network was then able to generate approximate macroscale model parameters given any arbitrary microstructure within the domain of the training set. Limitations of this approach are associated with the confidence in interpolating between microstructures, including interpolated microstructures that may not be stable in a thermodynamic sense [57]. In addition, potentially significant computational expense is required in the initial stages of this process in order to create an adequate training set for the ANN. Although ANNs may provide a convenient way to predict material model parameters, they are essentially a method of interpolation and generally do not provide any insight into the physical processes occurring at the microstructural level.

Shenoy et al. [6] also developed a macroscale transversely isotropic viscoplasticity (TIVP) model for a directionally solidified Ni-base superalloy based on homogenizing the response of several grains with random secondary orientation. The flow rule for this TIVP model is given as

$$\mathbf{D_i^p} = \dot{p}\mathbf{N} = Aexp\left(\frac{-Q}{RT}\right) \left\langle \frac{\bar{\sigma} - K}{D_0} \right\rangle^n \mathbf{N} \tag{2.33}$$

where $\mathbf{D_i^p}$ is the rate of deformation tensor, $\mathbf{N}$ is the unit vector in the direction of plastic strain, A is a constant, Q is the activation energy for the thermally activated dislocation bypass of obstacles, R is the gas constant, T is absolute temperature, $\bar{\sigma}$ is the effective stress, and D_0 is the drag stress. The temperature dependent parameters are the threshold stress K and the strain rate sensitivity exponent n. Further details of the formulation of this model may be found in Shenoy et al. [6].

This macroscale model showed better computational efficiency when compared against a CVP model while still capturing the aggregate material response from thermomechanical fatigue experiments, as well as capturing secondary creep behavior at high temperatures. In addition to averaging the response of multiple grains, another drawback to this sort of model is that it cannot capture tension-compression asymmetry, which could be significant near transition temperatures [6].

For prediction of material response under thermomechanical loading, Skelton [58] and Skelton et al. [59] suggested both graphical and analytical techniques that could be used to approximate the TMF hysteresis loops from isothermal fatigue data. It was found that modeling TMF curves was complex due to the history effects present in each half cycle and that constructing hysteresis loops be done first on stabilized material [58]. Later it was shown that using a cyclic energy parameter could resolve some of the difference in stress-strain prediction in TMF using isothermal data. A weakness of this method is that it does not work well for materials that exhibit history dependence.

2.5 Summary

Accurate life prediction under TMF must take into account each of the damage mechanisms and their contribution to overall damage of a component, since these mechanisms may vary depending on temperature and phase. Linear damage accumulation models with varying damage term definitions have been developed. Models which take into account stress concentrators, such as multiaxial Neuber models, have been used to attempt to predict life of notched components under TMF. Non-local computational methods which often utilize critical distance-type approaches, have also been used with some success. Spectral representation of crystal plasticity is an example of a powerful reduced order modeling method. Artificial neural networks have been used in reduced order constitutive modeling approaches at various levels of implementation, from transitioning from microscale to macroscale models to implicitly defining material constitutive behavior itself.

CHAPTER III

CALIBRATION OF A TRANSVERSELY ISOTROPIC VISCOPLASTICITY MODEL TO CM247LC-DS

3.1 Introduction

In order to reduce computational cost associated with life modeling of CM247LC-DS using a crystal viscoplasticity (CVP) Model [60], alternative modeling methods were explored. One such model is a transversely isotropic viscoplasticity (TIVP) Model for directionally solidified Ni-base superalloys. Like the CVP model, the TIVP model is implemented as a user material subroutine (UMAT) Fortran source code for ABAQUS [18] with a semi-implicit integration scheme. The model is calibrated using isothermal uniaxial test data in the temperature range 20°C to 1050°C generated by the CVP model and captures the homogenized aggregate response of multiple grains in the material. This model is also capable of performing TMF simulations and shows good correlation to IP and OP TMF data for CM247LC-DS.

3.2 TIVP Model Details

Developed by Shenoy, McDowell, and Neu [6], the TIVP model is a continuum-based model originally calibrated to a different directionally solidified Ni-base superalloy, DS GTD-111. Unlike the CVP model, the TIVP model does not explicitly consider individual grain orientation or slip systems across crystallographic planes and instead considers a representative volume element (RVE) that adequately describes material behavior, which is in effect assuming a large enough number of grains with random secondary orientation about the direction of solidification in order to homogenize the material response [6]. This model works well to predict elastic behavior of a DS alloy assuming there are 6-10 grains being considered [61] [6]. The flow rule and evolution equations are formulated in the intermediate configuration (using the second Piola-Kirchoff stress as a stress measure) to take into

account finite deformation effects [6].

The flow rule for the transversely isotropic viscoplasticity model is of the form

$$\mathbf{D_i^p} = \dot{p}\mathbf{N} = Aexp\left(\frac{-Q}{RT}\right)\left\langle\frac{\bar{\sigma}-K}{D_0}\right\rangle^n \mathbf{N} \tag{3.1}$$

where $\mathbf{D_i^p}$ is the rate of deformation tensor, $\mathbf{N}$ is the unit vector in the direction of plastic strain, A is a constant, Q is the activation energy for the thermally activated dislocation bypass of obstacles, R is the gas constant, T is absolute temperature, and D_0 is the drag stress. The temperature dependent parameters are the threshold stress K and the strain rate sensitivity exponent n. The effective stress $\bar{\sigma}$ is given by

$$\bar{\sigma} = \sqrt{3\left(J_2 - \xi\left(J - J_0^2\right) - \frac{3}{4}\zeta\left(J_0^2\right)\right)} \tag{3.2}$$

where

$$J_2 = \frac{1}{2}\Sigma_{ij}\Sigma_{ij} \tag{3.3}$$

$$J_0 = M_{ij}\Sigma_{ij} \tag{3.4}$$

$$J = M_{ij}\Sigma_{jk}\Sigma_{ki} \tag{3.5}$$

following Robinson and Binienda [62] where Σ_{ij} is the symmetric overstress defined as

$$\Sigma_{ij} = \sigma_{ij}^{PK2'} - \alpha_{ij} \tag{3.6}$$

where $\sigma_{ij}^{PK2'}$ is the second Piola-Kirchoff stress and α_{ij} is the backstress. Also, ξ and ζ are temperature dependent parameters specific to the material. The values of the parameters ξ and ζ have certain thermodynamic restrictions, which are

$$\xi \leq \frac{1}{2} \tag{3.7}$$

$$\xi \geq \frac{3}{4}\zeta \tag{3.8}$$

Details of this derivation can be found in Shenoy et al [6]. In order to capture kinematic hardening, back stress is used as an internal state variable (ISV). The back stress evolution is of the form

$$\dot{\alpha} = H\left(L\mathbf{D}_{\mathbf{i}}^{\mathbf{p}} - \boldsymbol{\pi}\dot{p}\right) - R_{\alpha}\bar{\alpha}^{m}\boldsymbol{\pi} \tag{3.9}$$

where H, L, m, and R_{α} are temperature dependent constants. The hardening and dynamic recovery is characterized by the first part of the evolution equation, whereas the second part captures the static thermal recovery of the material. The short-term viscoplastic response of the material is captured by the strain rate dependence of the flow rule and is minimally influenced by the back stress evolution. The components of $\boldsymbol{\pi}$ are given as

$$\boldsymbol{\pi_{ij}} = \alpha_{ij} - \xi\left(M_{ki}\alpha_{jk} - 2\hat{J}_0 M_{ij}\right) - \frac{3}{2}\zeta\hat{J}_0\left(M_{ij} - \frac{1}{3}\delta_{ij}\right) \tag{3.10}$$

where $\mathbf{M}$ is a dyad of the irreducible integrity basis of $\bar{\sigma}$ given as

$$\mathbf{M} = \mathbf{d_0} \otimes \mathbf{d_0} \tag{3.11}$$

Here $\mathbf{d_i}$ is the direction vector corresponding to the $\langle 001 \rangle$ direction in the reference configuration. The effective backstress $\bar{\alpha}$ is defined similarly to $\bar{\sigma}$ as

$$\bar{\alpha} = \sqrt{3\left(\hat{J}_2 - \xi\left(\hat{J} - \hat{J}_0{}^2\right) - \frac{3}{4}\zeta\left(\hat{J}_0{}^2\right)\right)} \tag{3.12}$$

where

$$\hat{J}_2 = \frac{1}{2}\alpha_{ij}\alpha_{ij} \tag{3.13}$$

$$\hat{J}_0 = M_{ij}\alpha_{ij} \tag{3.14}$$

$$\hat{J} = M_{ij}\alpha_{jk}\alpha_{ki} \tag{3.15}$$

For further details on this model and its formulation, see Shenoy et al. [6].

3.3 Calibration

Since the TIVP model was originally calibrated to a similar Ni-base superalloy, DS GTD-111, the original temperature dependent parameters determined by Shenoy et al. [6] were used as a starting point. The new parameters were fitted manually to stabilized cyclic isothermal hysteresis loops obtained from the most current version of the CVP model calibrated by Kirka [60]. Calibration curves can be found in Appendix A. The model was calibrated at nine different temperatures: 20°C, 150°C, 300°C, 650°C, 750°C, 850°C, 950°C, 1000°C, and 1050°C, with additional temperatures of 800°C, 900°C used for secondary creep calibration. An example calibration curve is shown in Figure 3.1. The calibration was performed on a unit cube, a single element of type C3D8, with boundary conditions such that three adjacent orthogonal faces were fixed on rollers in their respective normal directions.

For material orientation within the UMAT, the Euler angle convention used is a right-handed Z-Y′-Z′ transformation, as shown in Figure 3.2. The three angles ϕ , φ_1 , φ_2 correspond to counterclockwise rotation about the Z, Y′, and Z′ axes, respectively. In the UMAT, the ⟨001⟩ direction of solidification in the model is along the global Z-axis. In order to simulate a longitudinal loading case, the FEA model must either be loaded in the global Z-direction, or proper Euler angles corresponding to an equivalent loading must be specified. For example, if an FEA model is loaded in the Y-direction and longitudinal response is desired, the Euler angles 90°, 90°, 0° must be used to properly rotate the material coordinates and ensure the ⟨001⟩ direction is aligned with the Y-axis. Alternatively, a local material orientation may be specified within ABAQUS through the *ORIENTATION keyword. If this option is used, the material coordinates may be assigned within ABAQUS to desired directions and the three Euler angles given to the UMAT are simply (0°, 0°, 0°).

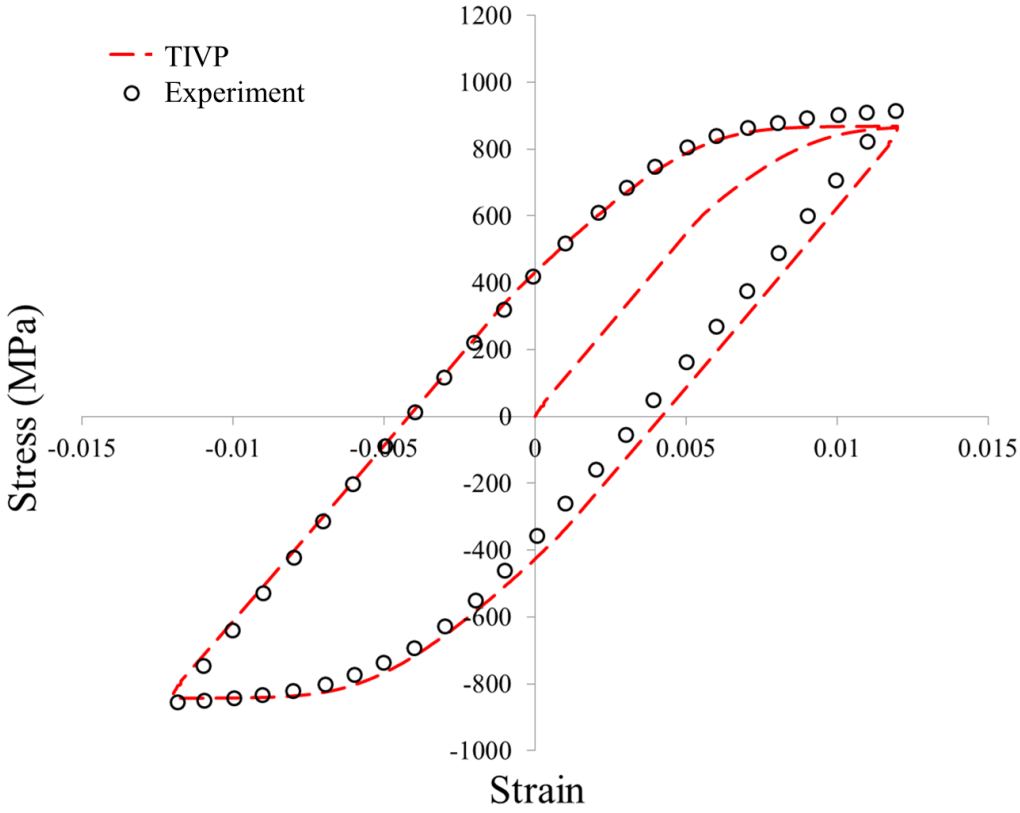

Figure 3.1: TIVP model calibration curve for 650°C, longitudinal orientation

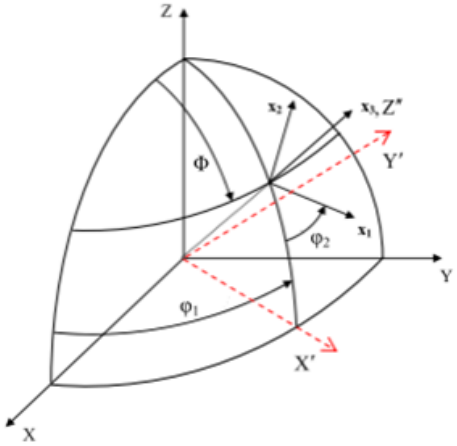

Figure 3.2: Rhoe convention for Euler angles specifying rotation [40]

For initial calibration, the parameters R_α and m were set to zero (i.e. the secondary creep behavior was ignored) since the calibration was done at an intermediate strain rate of $10^{-4}s^{-1}$. The first parameter that was determined was the threshold stress, K. Although K is sometimes used as an ISV, it was treated as a temperature dependent constant following

Shenoy et. al. [6], since CM247LC-DS is cyclically stable. The values of K were selected such that they followed the general trend of yield stress with increasing temperature, an example of which is shown in Figure 3.3.

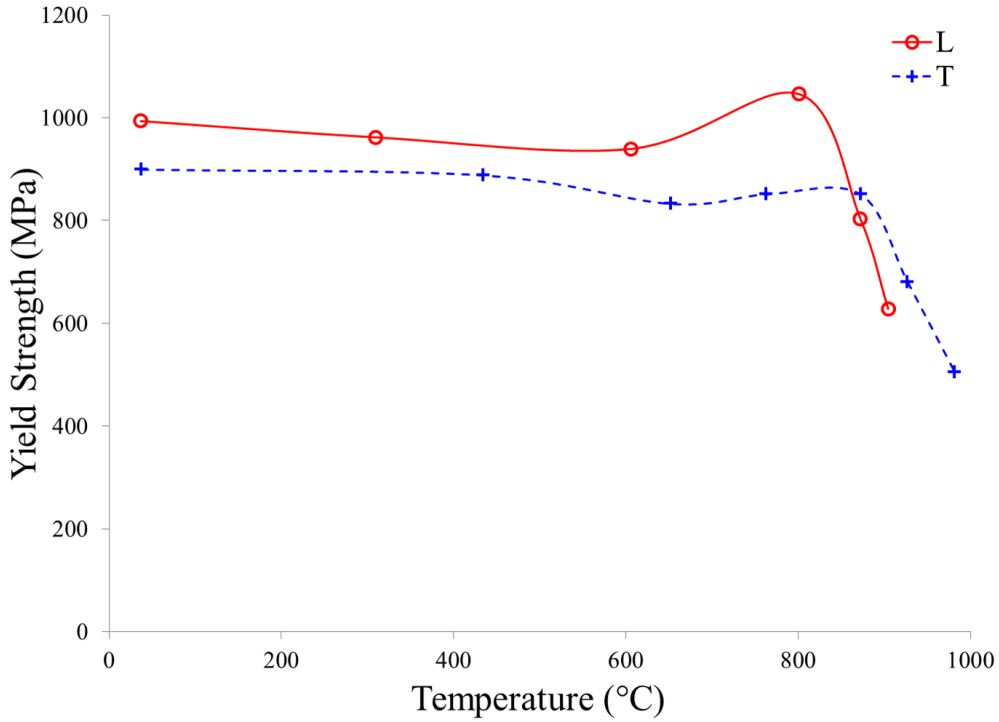

Figure 3.3: 0.2% offset yield strength of CM247LC-DS as a function of temperature for longitudinal and transverse orientations [63]

After the values of K are selected, the other model parameters are found. All of the parameters are interdependent; that is, changing one usually requires changing all of the others to give the same response. The parameter ξ does not affect the uniaxial response of the material and was unimportant for calibration to uniaxial data, although it was assigned a value that satisfied the thermodynamic restrictions outlined in Equations 3.7 and 3.8. That is,

$$\xi = \frac{3}{4}\zeta \tag{3.16}$$

The parameter ζ controls the rate of dissipation through the effective stress term, and, similar to ξ, potential assigned values are also restricted. Visually, increasing the value of ζ will increase the slope of the stress-strain curve just after yielding. The values of ξ and ζ

decrease with increasing temperature. The back stress constants H and L were calibrated after suitable values of other parameters were found. The parameter L controls the slope of the stress-strain curve after yielding, more so than ζ. Decreasing L decreases the rate of hardening and widens the hysteresis loop slightly. For H, increasing its value widens the hysteresis loop and vice versa. From there, iteration was required to obtain a good set of parameters that matched the experimental data well.

.

Table 3.1: Elastic and inelastic model parameters for CM247LC-DS

Temp. (°C)	E_L (MPa)	E_T (MPa)	G_L (MPa)	ν_T	ν_Z	K (MPa)
20	129,453	178,138	125,929	0.4	0.2	200
150	126,529	174,606	124,179	0.4	0.2	200
300	121,689	164,015	118,300	0.4	0.2	200
650	104,317	139,944	104,400	0.4	0.2	200
750	97,776	130,587	99,700	0.4	0.2	400
800	94,249	125,528	97,200	0.4	0.2	*280
850	90,560	121,557	94,300	0.4	0.2	160
900	86,672	115,860	91,100	0.4	0.2	*110
950	82,623	111,583	87,500	0.4	0.2	60
1000	78,399	107,975	82,900	0.4	0.2	38
1050	74,020	100,586	77,400	0.4	0.2	15

Temp. (°C)	n	ξ	ζ	H	L (MPa)	R_α (MPa^{-3})	m
20	95	0.28	0.35	420	120	0	0
150	60	0.28	0.35	470	120	0	0
300	40	0.28	0.35	520	120	0	0
650	20	0.24	0.3	840	180	0	0
750	18	0.21	0.26	625	180	0	0
800	17*	0.14*	0.17*	523*	200*	2.00E-7	1
850	16	0.06	0.08	420	220	4.75E-7*	1*
900	15*	0.05*	0.065*	335*	220	7.50E-7	1
950	14	0.04	0.05	250	220	1.38E-6*	1*
1000	8	0.04	0.05	185	160	2.00E-6	1
1050	4	0.04	0.05	100	20	2.00E-6	1

A (1/s)	Q (kJ/mol)	R (J/molK)	D_0 (MPa)
5.006825E+11	450	8.314	102

Note: * Value determined by linear interpolation

It is important to note that the set of parameters that may be selected to match observed material response is non-unique, which is why parameters were chosen such that they made physical sense. This was important for the linear interpolation utilized in the UMAT between calibration temperatures; if parameters were selected which do not make sense physically, the model would not interpolate well between calibration temperatures and thermo-mechanical simulations would be unreliable. A plot of each parameter as a function of temperature is shown in Figures 3.4 through 3.7. At the transition temperature of 750°C, the threshold stress jumps significantly. Although the large jump could be partly a consequence of the parameters chosen for calibration, it also reflects the hardening of the γ' precipitates with a rise in temperature.

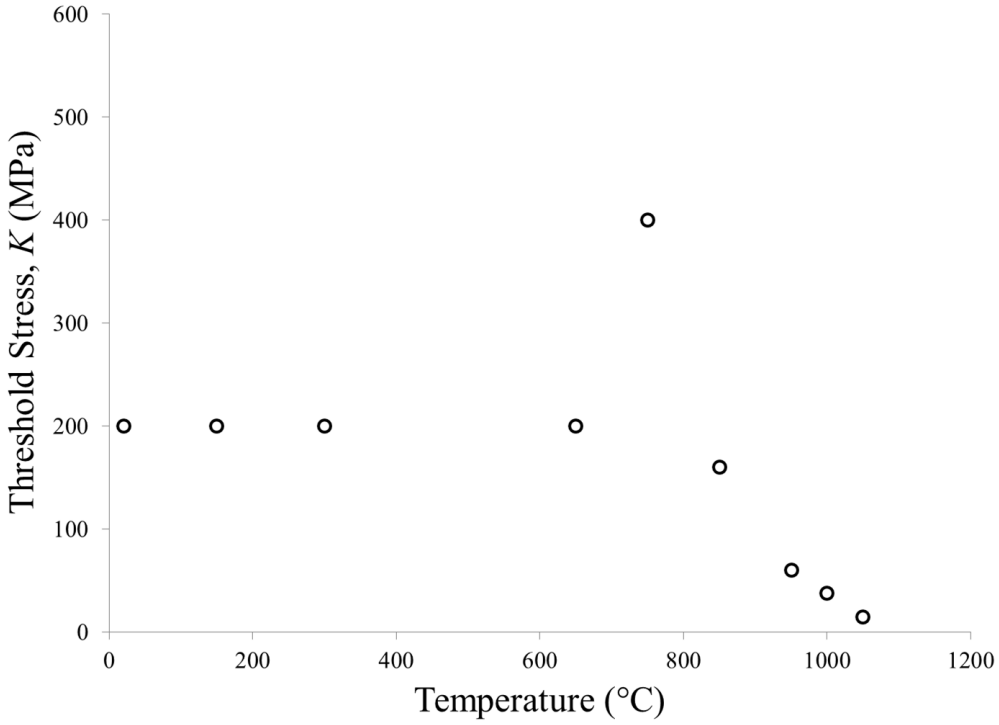

Figure 3.4: Threshold stress K as a function of temperature

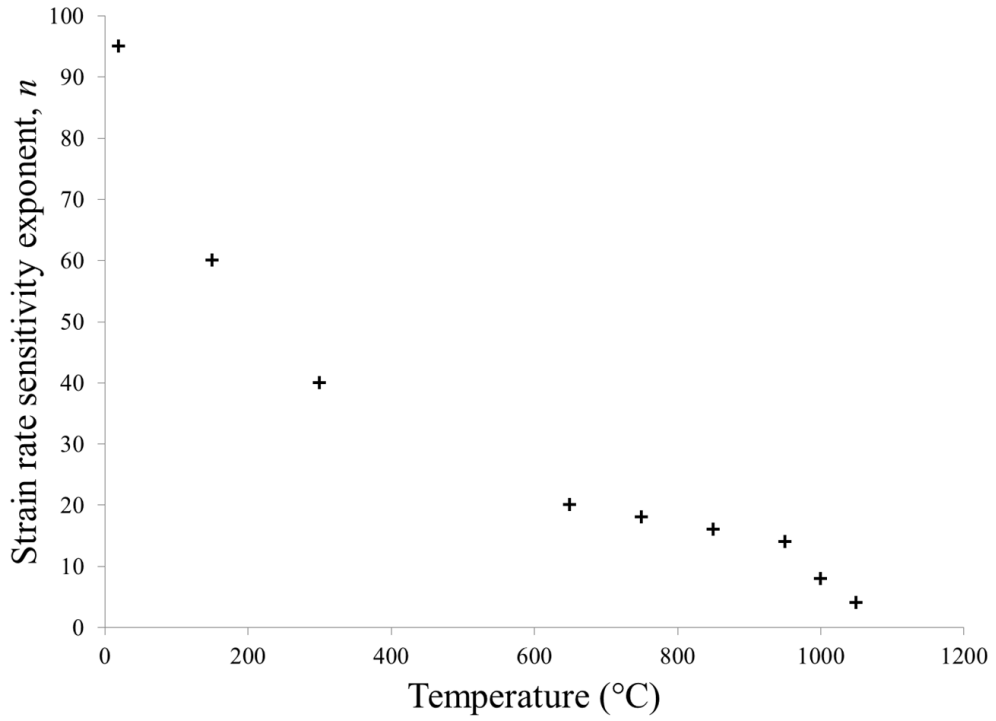

Figure 3.5: Strain rate sensitivity exponent n as a function of temperature

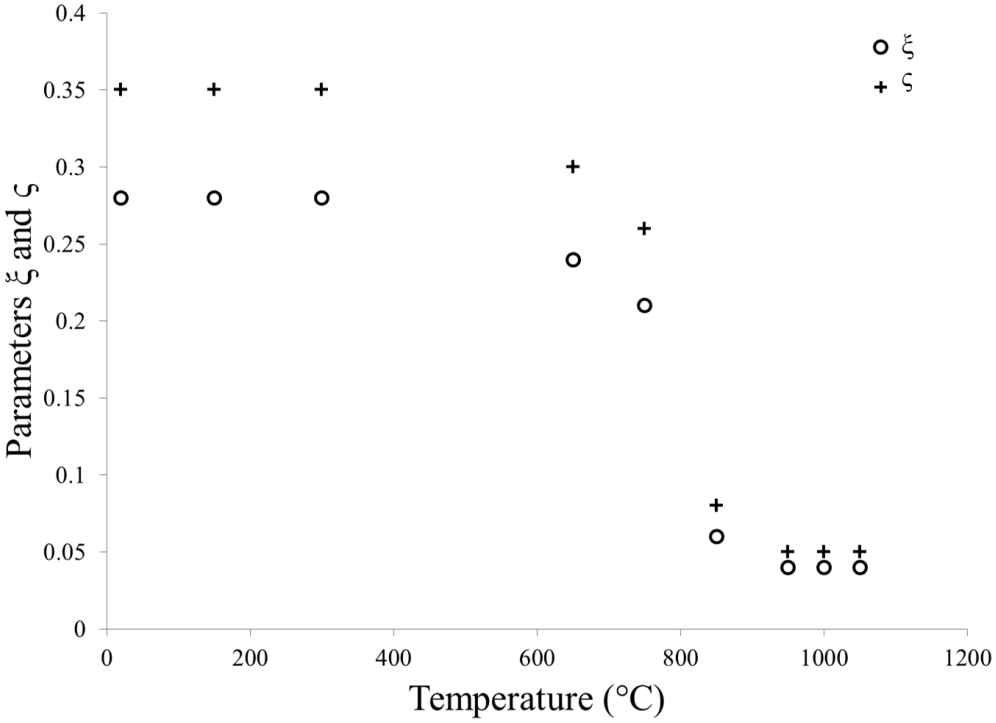

Figure 3.6: Dimensionless parameters ξ and ζ with temperature

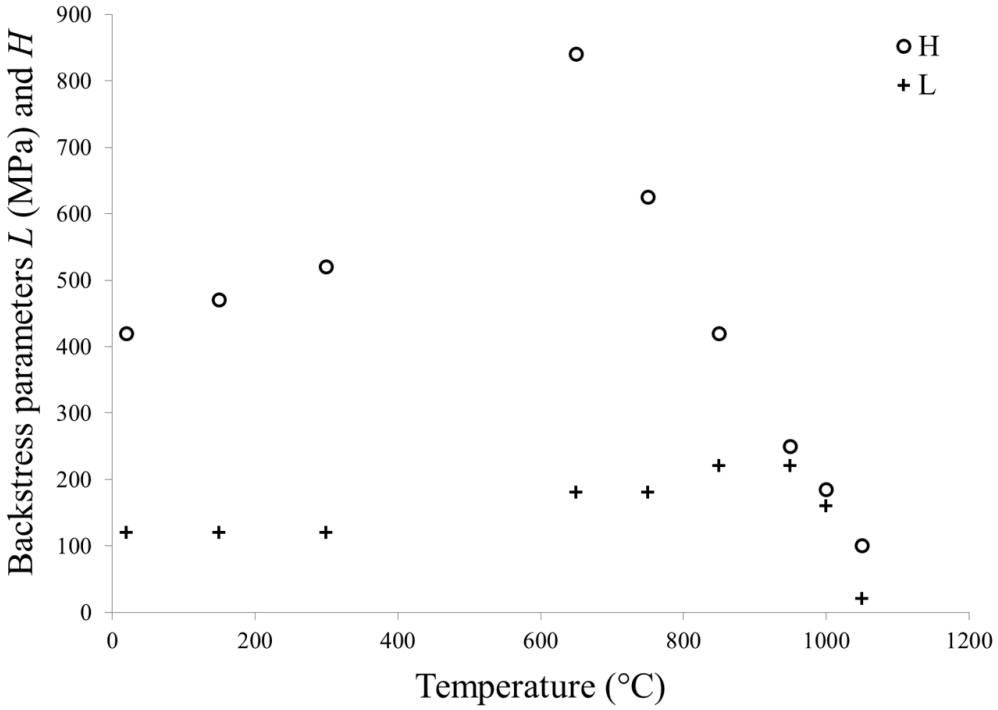

Figure 3.7: Back stress hardening parameters H and L as functions of temperature

The only model parameters which were not predicted through linear interpolation at intermittent temperatures were the elastic modulus for both longitudinal and transverse orientations, E_L and E_T respectively, and the shear modulus G_L. The temperature dependence of the elastic properties with temperature is well-understood and follows a negative quadratic trend, which is captured using a second degree polynomial. Poissons ratios with respect to the longitudinal and transverse orientations, ν_L and ν_T respectively, are assumed independent of temperature.

After initial calibration, the thermal recovery parameters were adjusted to match secondary creep behavior at three different temperatures: 800°C, 900°C, and 1000°C, at different stress levels within the elastic domain. Originally, the value of m was set to 3 in accordance with Shenoy et al. [6] , but it was found that the corresponding values of the parameter R_α did not fit the data well across different stress levels. The value of the exponent m was lowered to 1 and new values for R_α were determined. Plots of the creep predictions for each calibration temperature at separate normalized stress levels can be seen in Figures 3.8 through 3.10. The model is not able to capture tertiary creep, as this is normally associated with damage and would require an additional ISV in conjunction with some sort of damage model.

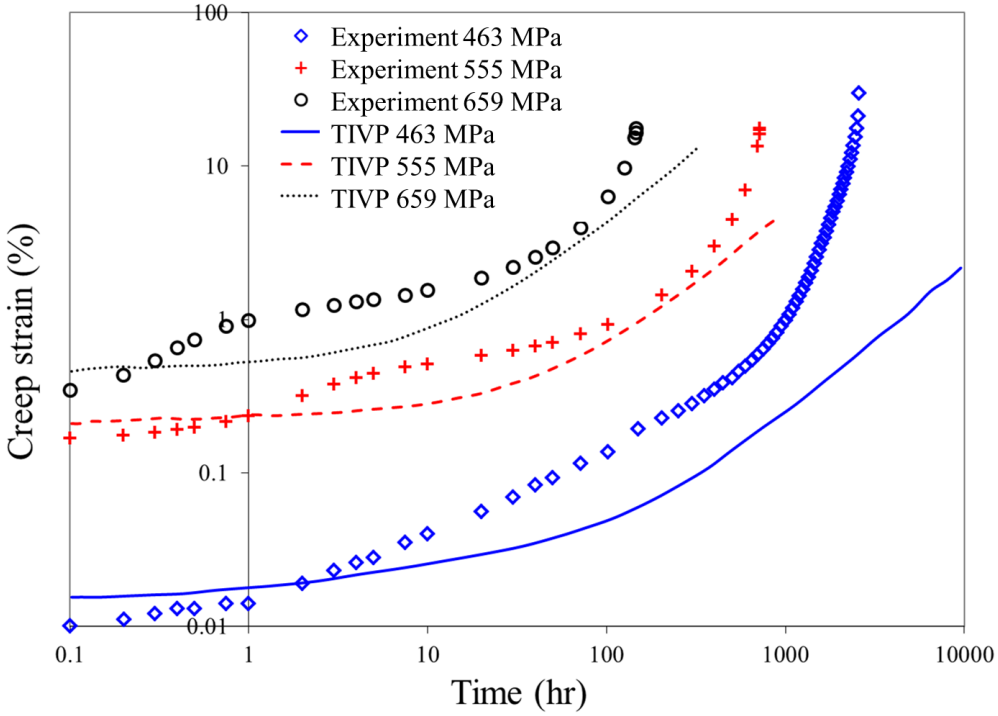

Figure 3.8: Comparison of TIVP model creep strain prediction to test data, 800°C

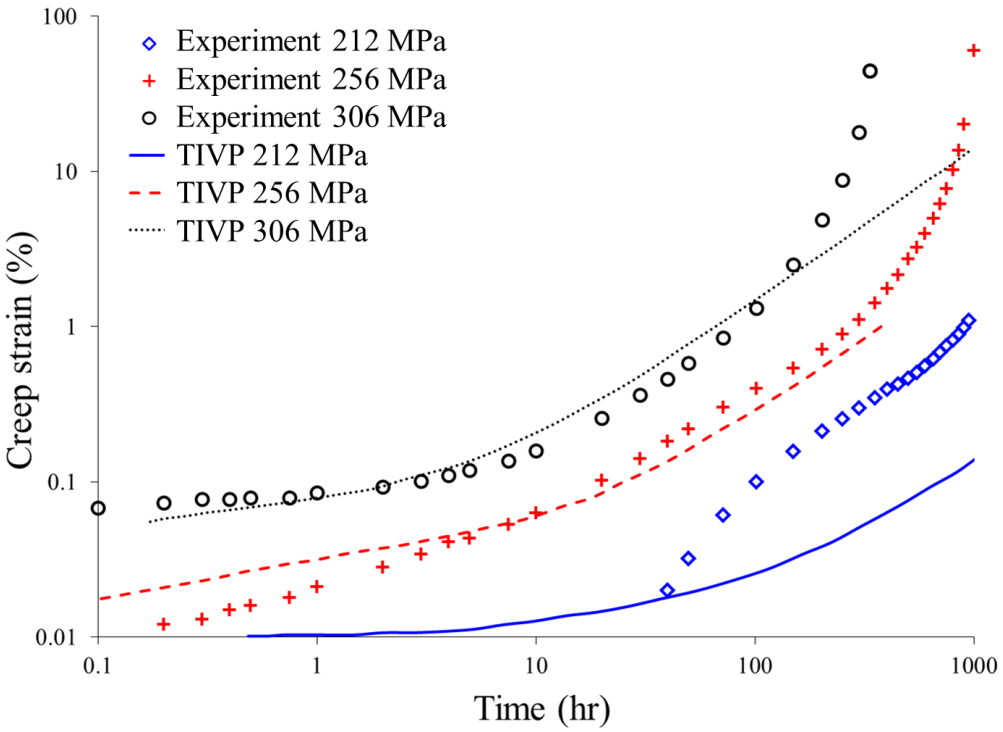

Figure 3.9: Comparison of TIVP model creep strain prediction to test data, 900°C

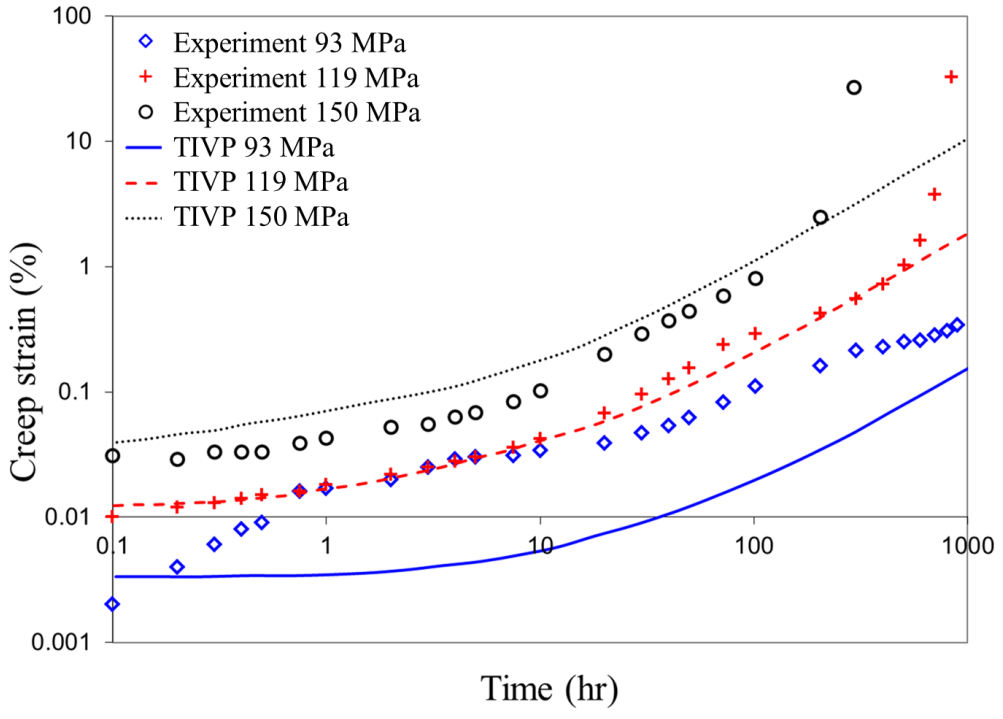

Figure 3.10: Comparison of TIVP model creep strain prediction to test data, 1000°C

Isothermal response was then checked at a slower strain rate of $4 \cdot 10^{-6} s^{-1}$ at higher temperatures to see if backstress parameters needed readjustment to fit the data, which they did not. An example of a TIVP model prediction at a slower strain rate is shown in Figure 3.11.

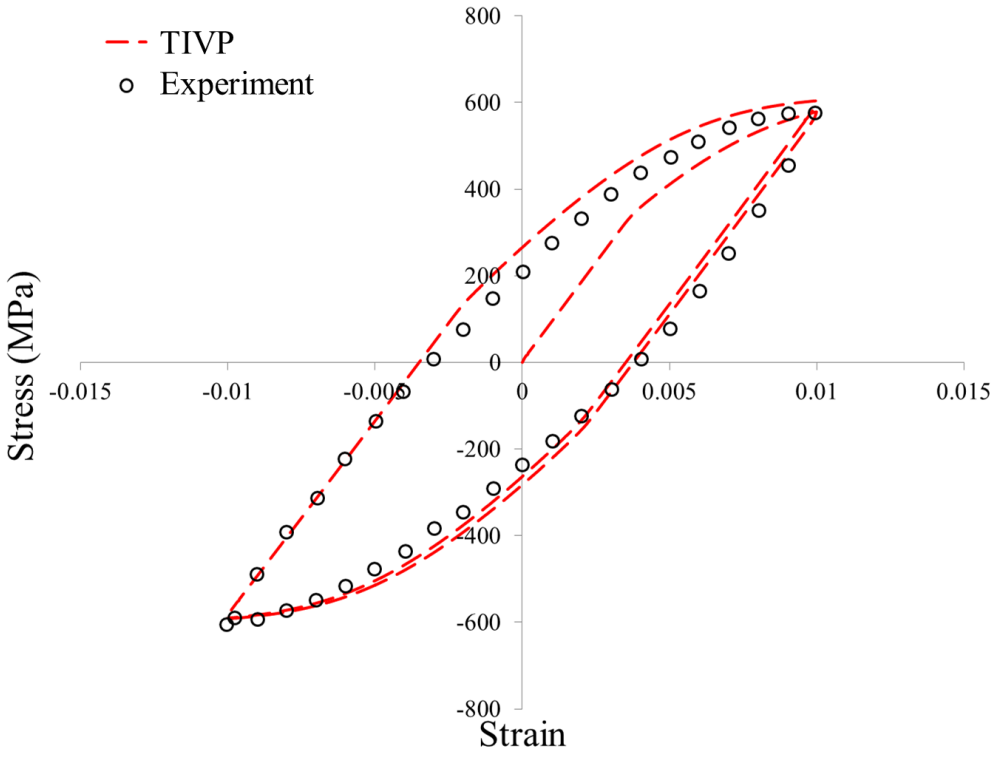

Figure 3.11: TIVP model prediction at 850°C, strain rate $4 \cdot 10^{-6} s^{-1}$, compared to experimental data

Once parameters were determined for the model, the UMAT was altered to include a thermal deformation gradient to account for thermal strain. Thermal strain was calibrated using data from a free thermal expansion test conducted over the temperature range 100°C to 950°C using a tangent method. Fitting a third order polynomial to a plot of thermal strain as a function of temperature and taking the derivative with respect to temperature yielded a second order polynomial that described the coefficient of thermal expansion as a function of temperature. This coefficient of thermal expansion was used to define a thermal deformation gradient whose form is given in Equation 3.17.

$$\mathbf{F}^{\theta}_{\mathbf{n+1}} = exp(\alpha \Delta T \mathbf{I}) \mathbf{F}^{\theta}_{\mathbf{n}} \tag{3.17}$$

A comparison of the raw thermal strain data to the TIVP model prediction can be seen in Figure 3.12.

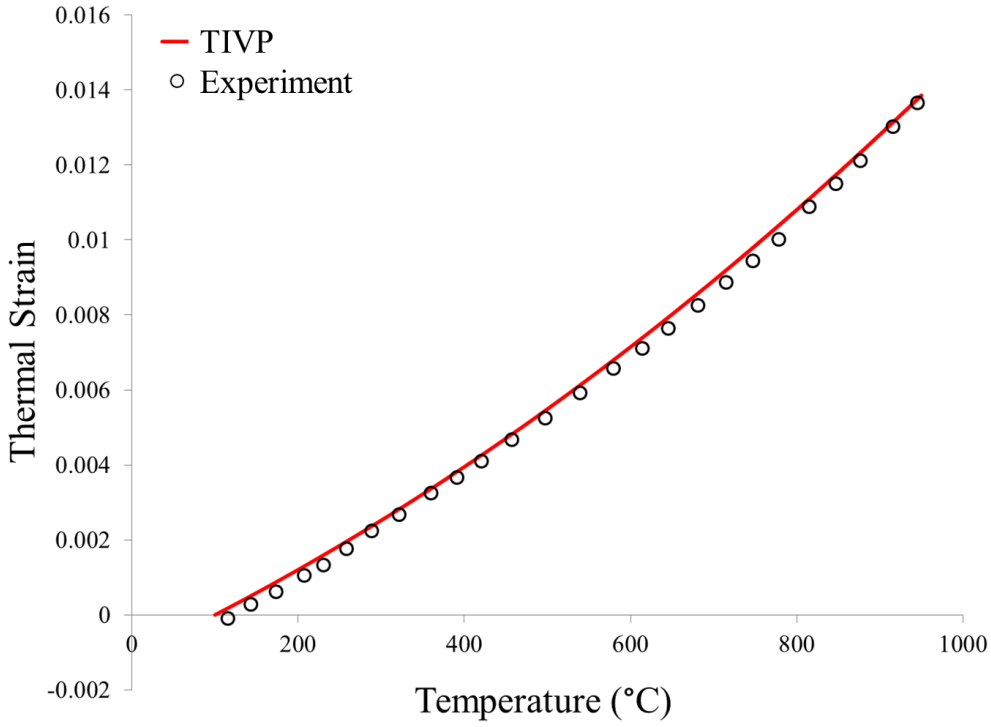

Figure 3.12: Comparison of thermal strain experimental data to TIVP prediction, 100-950°C temperature range

3.4 Model Verification

To verify that the model is predicting results consistently with finite element models consisting of multiple elements as opposed to just a single element, a few comparisons were made between the single element isothermal simulations used for calibration of the model and multi-element simulations of an eight-element cube. Free expansion and TMF simulations were also conducted in order to compare the results. Results for the eight element cube were collected through the use of reference nodes, in the manner of Zhang [64] and Alley [65]. This is depicted in Figure 3.13.

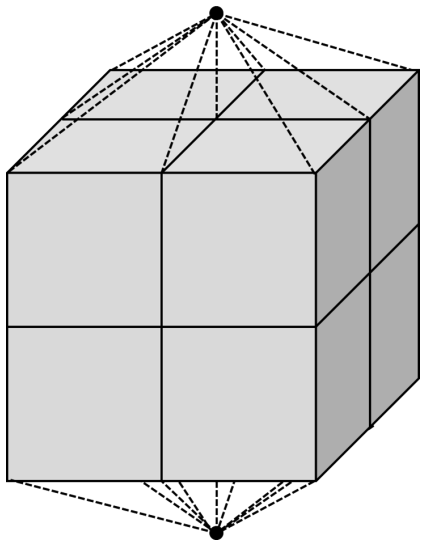

Figure 3.13: Placement of reference nodes used to record response

The forces and displacements recorded at the reference nodes were converted to stresses and strains, respectively, using the dimensions of the cube. The responses of both the single element and eight element cubes are indentical under isothermal and TMF conditions, as well as thermal expansion cases. These can be seen in Figures 3.14 through 3.17.

In addition, a more complex asymmetric model was run using the TIVP UMAT in order to verify that the code was working properly and giving reasonable results for different geometries. The case used for this verification of the TIVP UMAT is a three dimensional plate with a circular hole in the center, which is represented using a one-eighth symmetry model, similar to the model used by Shenoy et al. [6]. This model is shown in Figure 3.18 and consists of 2114 elements and 3381 nodes. For the plate model, boundary conditions that

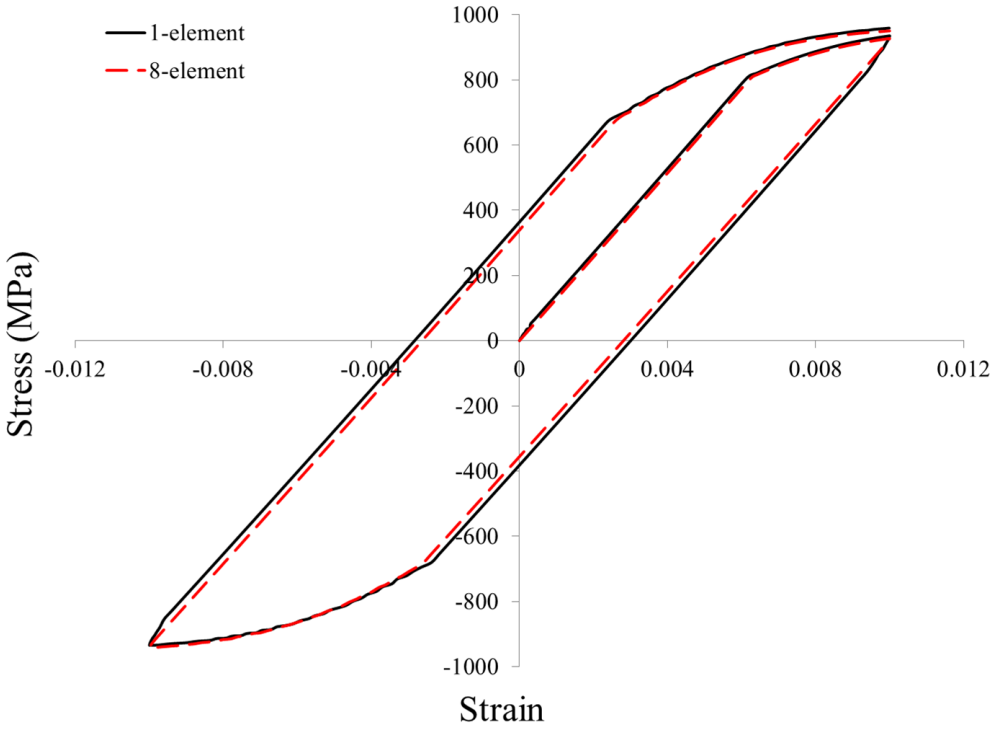

Figure 3.14: Comparison of single element and eight element responses at 100°C

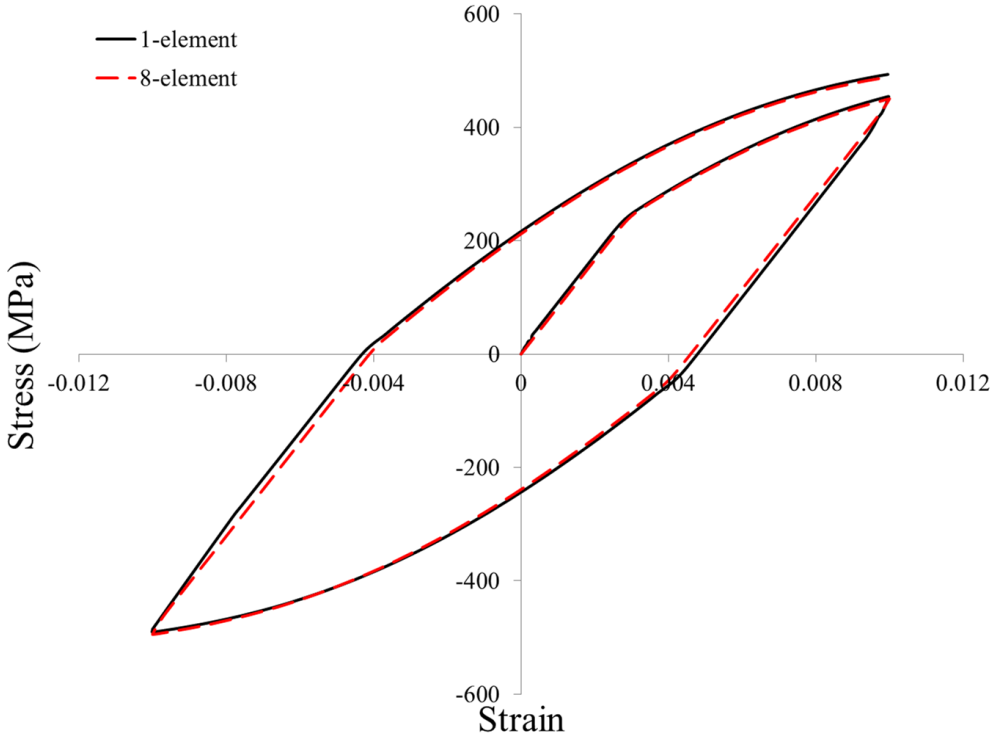

Figure 3.15: Comparison of single element and eight element responses at 950°C

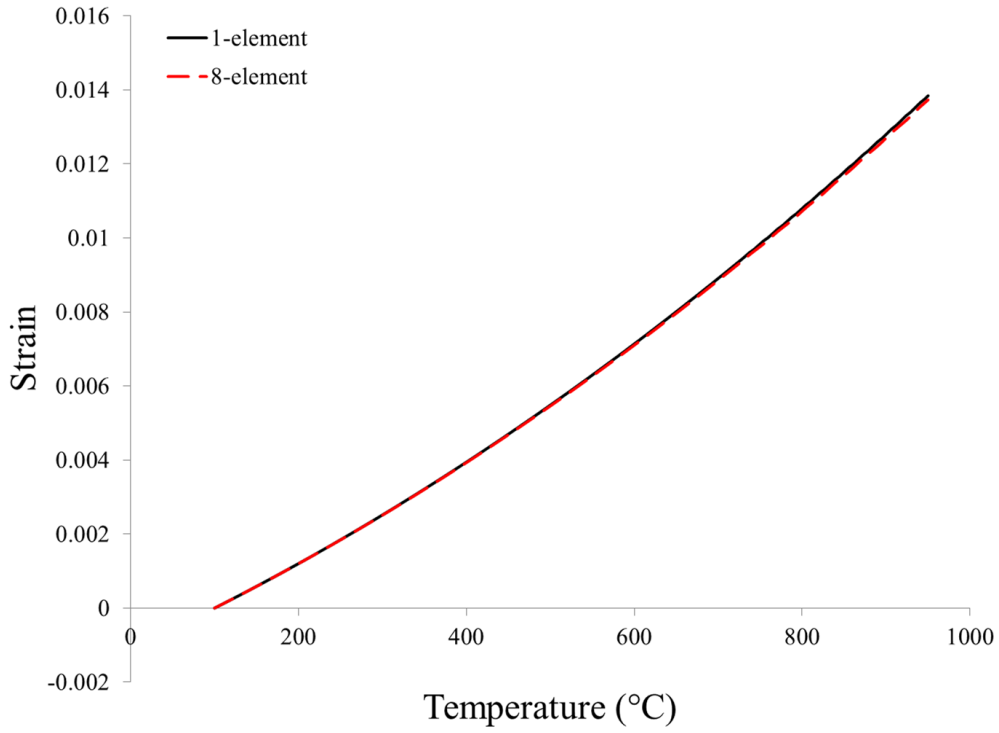

Figure 3.16: Comparison of single element and eight element responses, free thermal expansion from 100-950°C

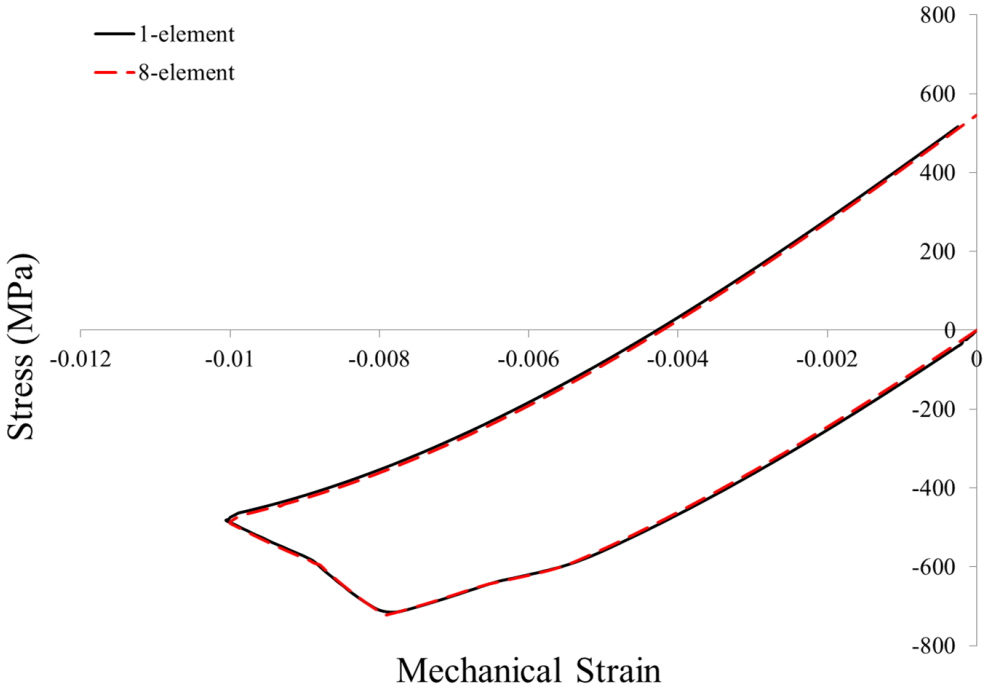

Figure 3.17: Comparison of single element and eight element responses, OP TMF 100-950°C, $R = -\infty$

reflected the full plate with circular hole in the center were chosen. This was accomplished through the use of ABAQUS commands XSYMM, YSYMM, and ZSYMM on three of the planar faces that would be exposed if the entire plate were to be cut into eight identical pieces. All other surfaces were traction free. For isothermal simulations, a displacement of 0.3 mm is specified on the top surface in a single step over 2 seconds. Free thermal expansion and OP TMF simulations were conducted over a 100-second step. The material is oriented such that the direction of solidification is aligned with the Y-direction of the plate. These simulations therefore correspond to a longitudinal loading case.

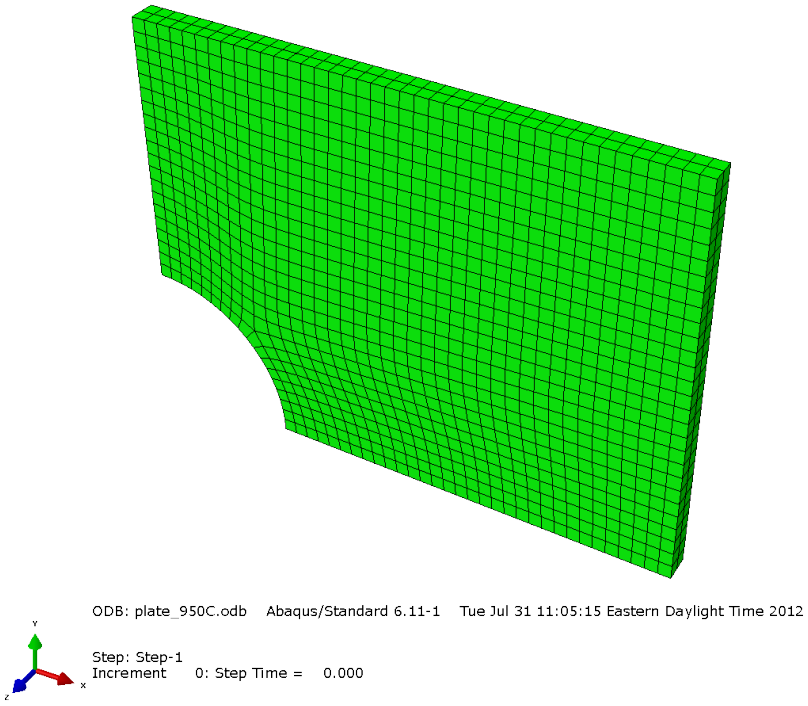

Figure 3.18: Plate model used for TIVP UMAT verification in ABAQUS

For off-axis loading (i.e. loading at angles not aligned with the direction of solidification), simulations were performed on the single cube element with boundary conditions used for calibration of the model. To check elastic behavior, simulations were conducted where the $\langle 001 \rangle$ direction of solidification was varied from zero to 90 degrees (longitudinal to transverse orientations). Simulation results can be seen in Figure 3.22, compared to experimental data for elastic modulus with respect to orientation at 850°C for CM247LC-DS.

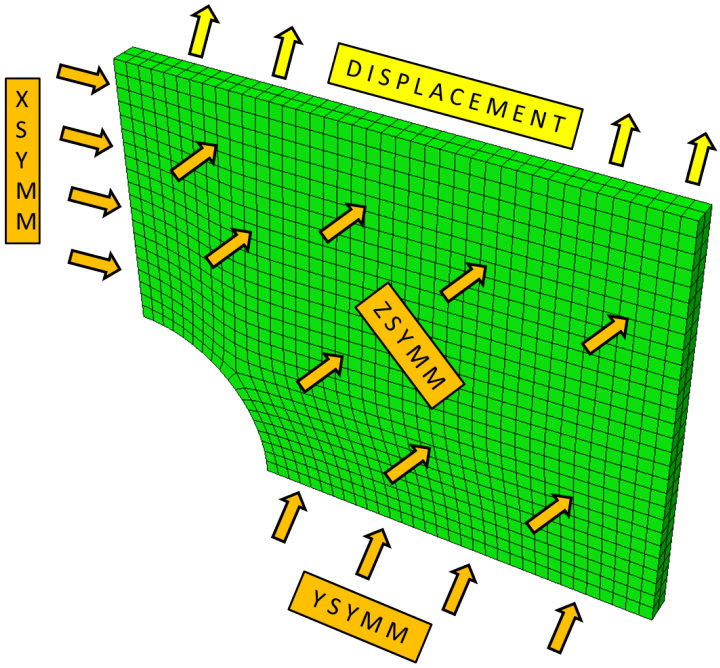

Figure 3.19: Boundary conditions assigned to the plate model, reflected through ABAQUS commands

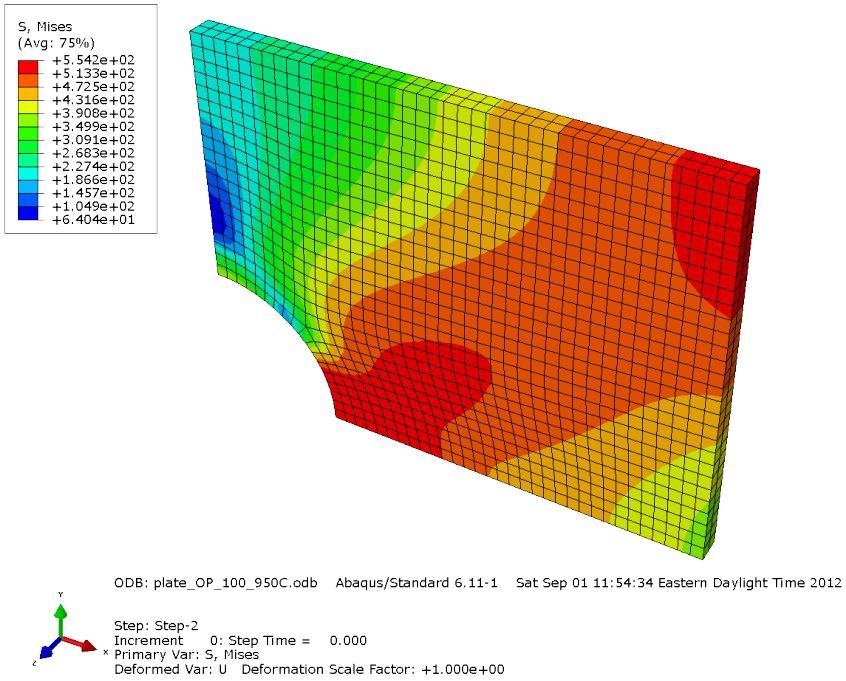

Figure 3.20: Von Mises stress after monotonic compressive loading to 0.3 mm mechanical displacement under OP TMF 100-950°C conditions at maximum temperature, ramp time 100 s

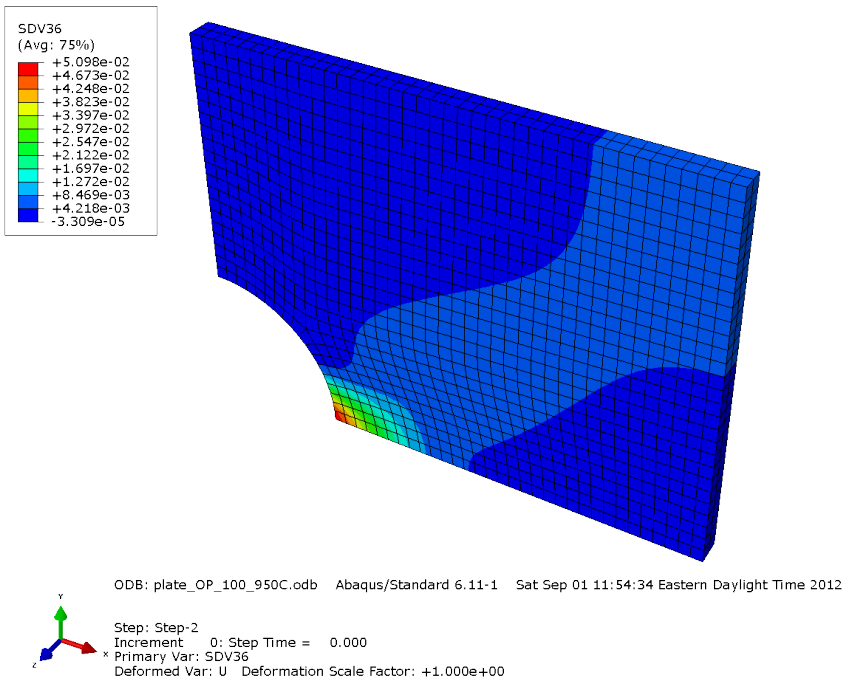

Figure 3.21: Effective plastic strain after monotonic compressive loading to 0.3 mm mechanical displacement under OP TMF 100-950°C conditions at maximum temperature, ramp time 100 s

The difference in the values for elastic modulus in the longitudinal orientation are due to differences between the data presented from the literature and the Siemens data used to calibrate the model. TIVP model predictions for elastic modulus at several temperatures as a function of orientation are shown in Figure 3.23. TIVP model predictions of 0.2% offset yield strength as a function of orientation at different temperatures are shown in Figure 3.24.

3.5 Validation

The validity of the model for TMF conditions was tested by comparing the TIVP model predictions to experimental TMF data, both IP and OP and at different R ratios. For completed reversed loading at $R_\epsilon = -1$, the model showed good predictions for the mid-life cycle hysteresis loops, although the model predicted a mean stress closer to zero than was observed in experiment. For a different R ratio of $R_\epsilon = -\infty$, OP TMF simulations showed good agreement with experimental data.

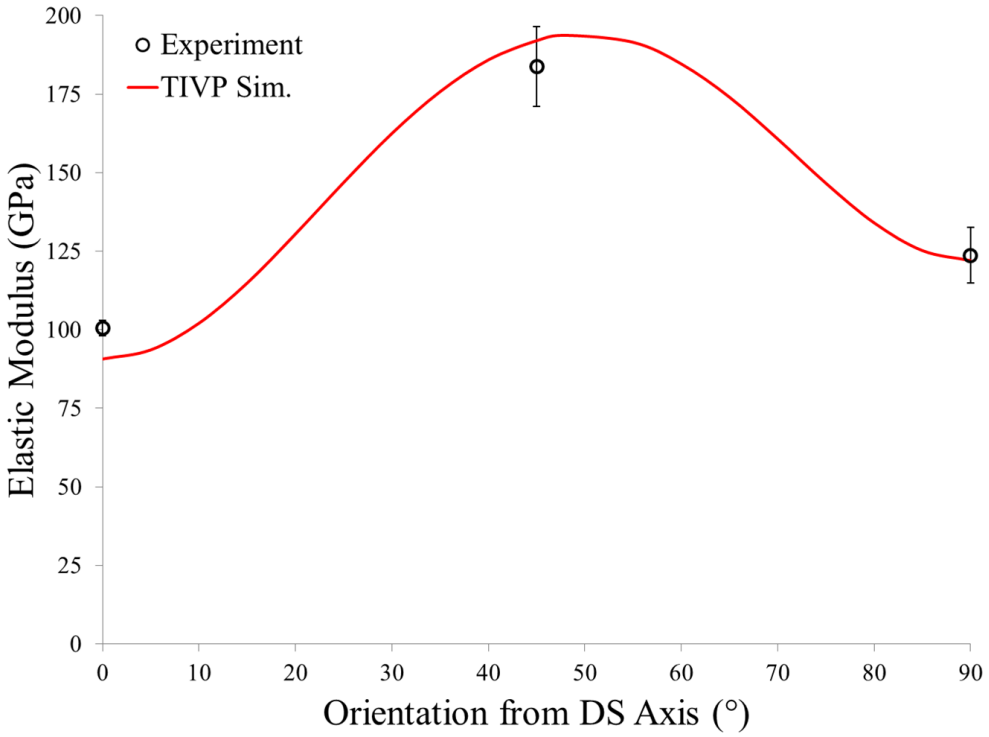

Figure 3.22: Elastic modulus of CM247LC-DS at 850°C as a function of orientation, TIVP sim. compared to literature [63]

Limitations of this model are discussed at length in Shenoy et al. [6]. In addition to these limitations, since the TIVP model was calibrated to as-received CM247LC-DS, the model would be unable to capture any behavior associated with microstructural changes due to stress and temperature; for example, observed decreased yield strength after compressive holds in OP TMF.

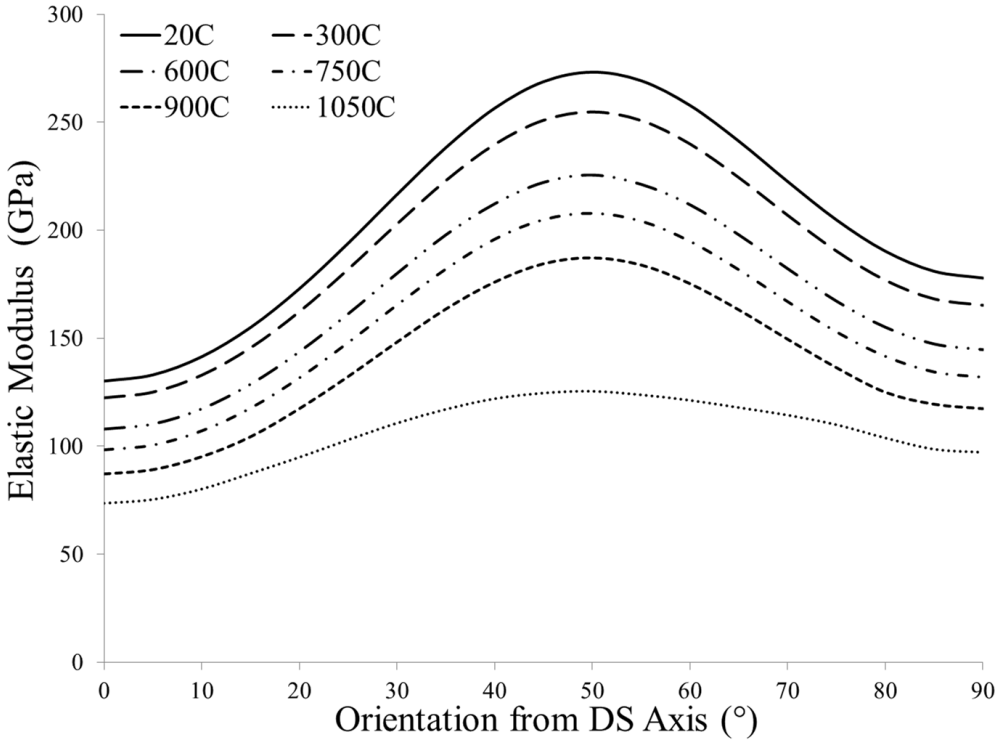

Figure 3.23: Elastic modulus of CM247LC-DS as a function of orientation for various temperatures, TIVP sim.

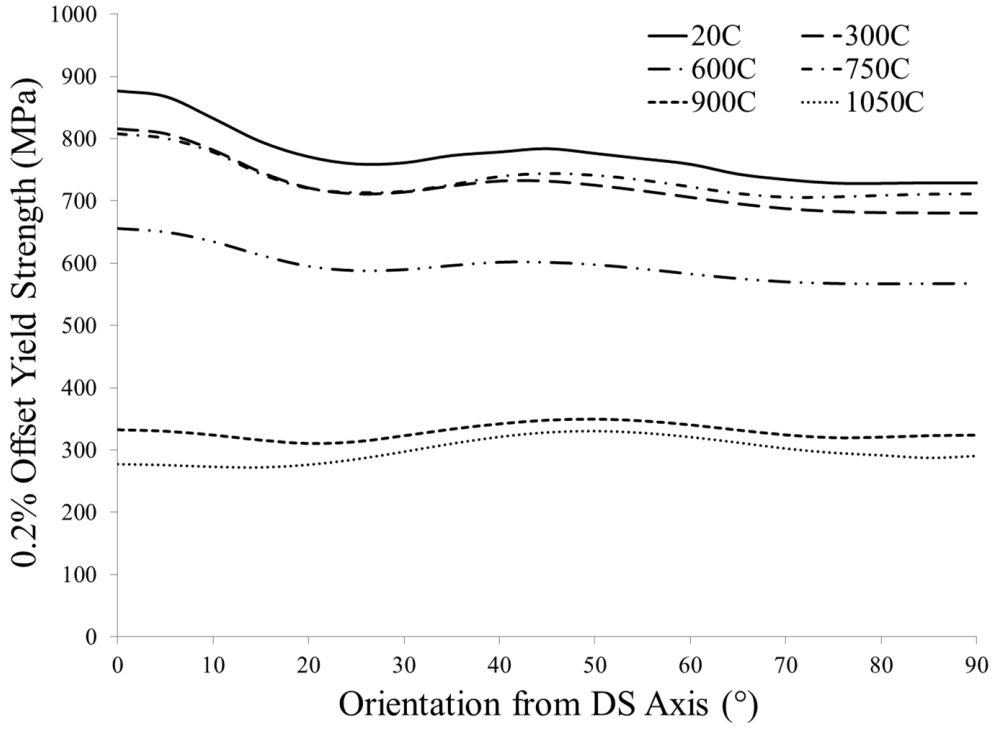

Figure 3.24: 0.2% offset yield strength of CM247LC-DS as a function of orientation for various temperatures, TIVP sim.

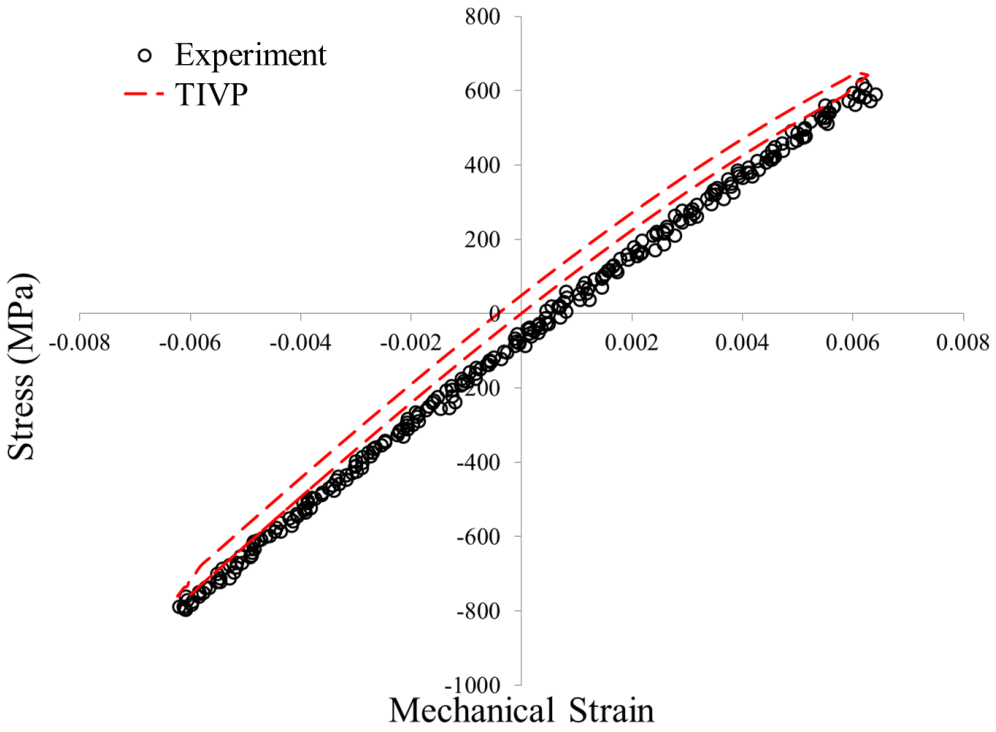

Figure 3.25: Mid-life cycle comparison under IP TMF conditions for single element, 0.0625 strain amplitude, min. temp. 100°C, max. temp 750°C, $R_\epsilon = -1$

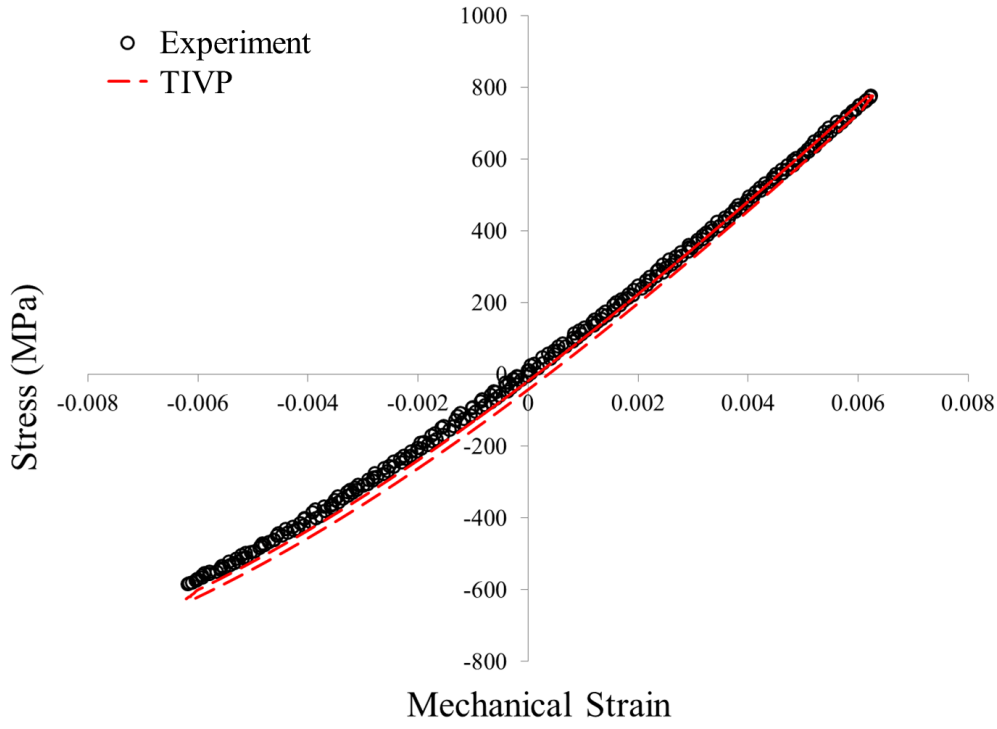

Figure 3.26: Mid-life cycle comparison under OP TMF conditions for single element, 0.0625 strain amplitude, min. temp. 100°C, max. temp 750°C, $R_\epsilon = -1$

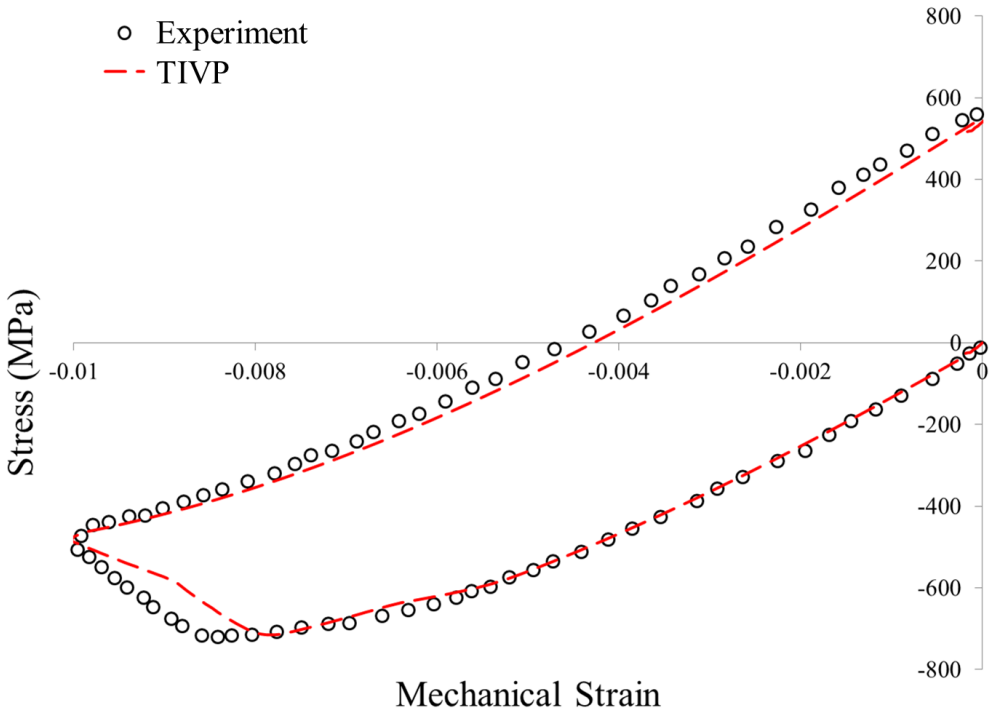

Figure 3.27: First cycle comparison under OP TMF conditions for single element, 0.01 strain range, min. temp. 100°C, max. temp 950°C, $R_\epsilon = -\infty$

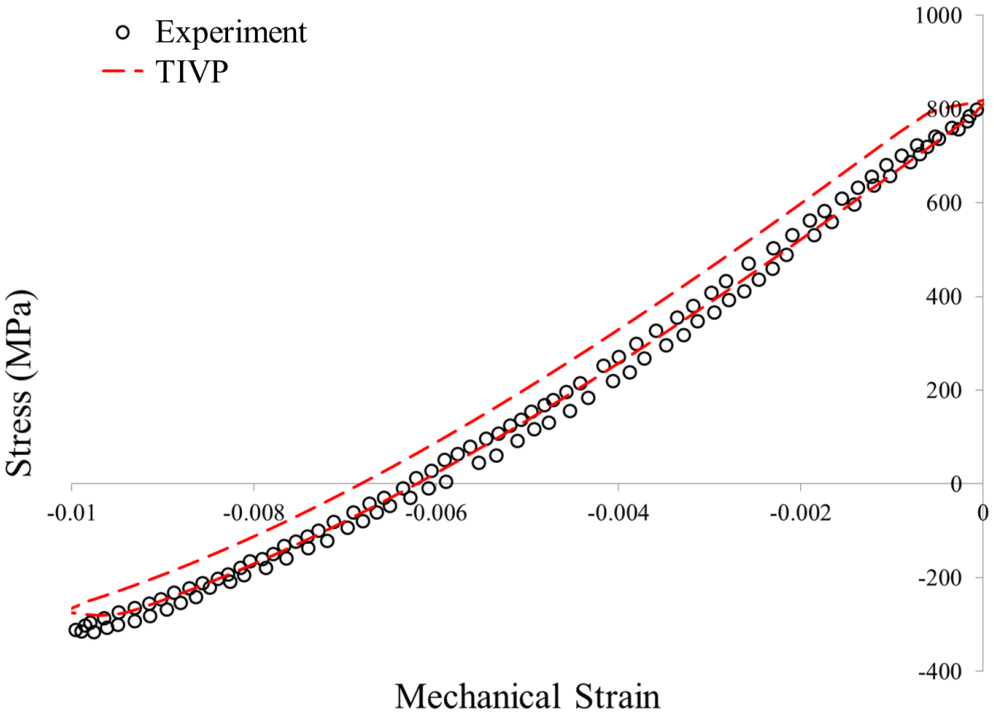

Figure 3.28: Mid-life cycle comparison under OP TMF conditions for single element, 0.01 strain range, min. temp. 100°C, max. temp 950°C, $R_\epsilon = -\infty$

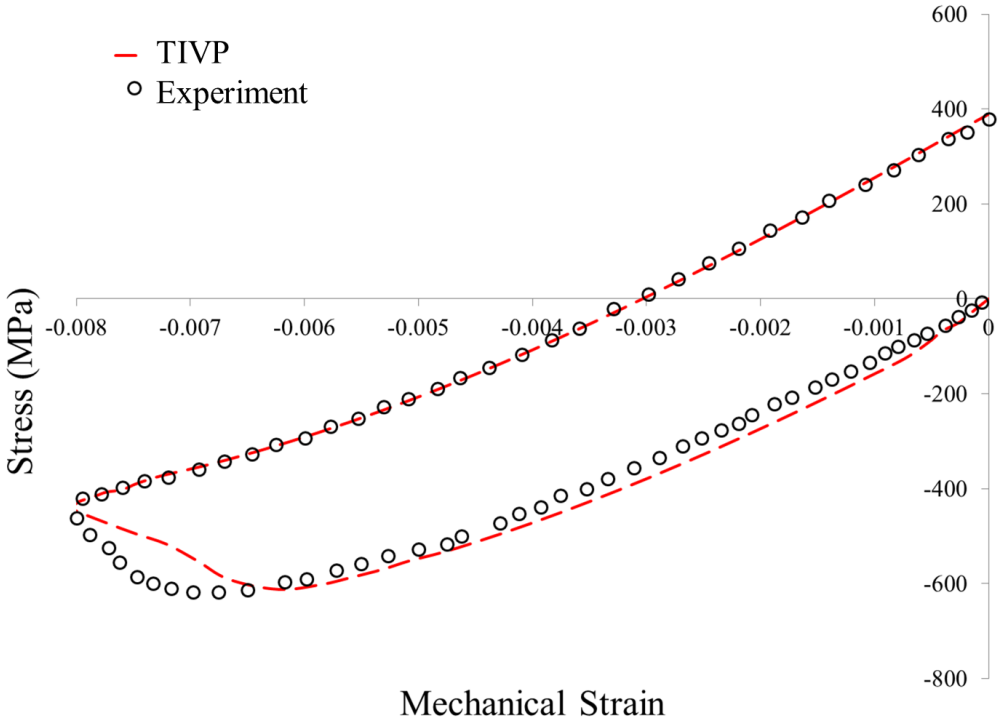

Figure 3.29: First cycle comparison under OP TMF conditions for single element, 0.008 strain range, min. temp. 100°C, max. temp 950°C, $R_\epsilon = -\infty$

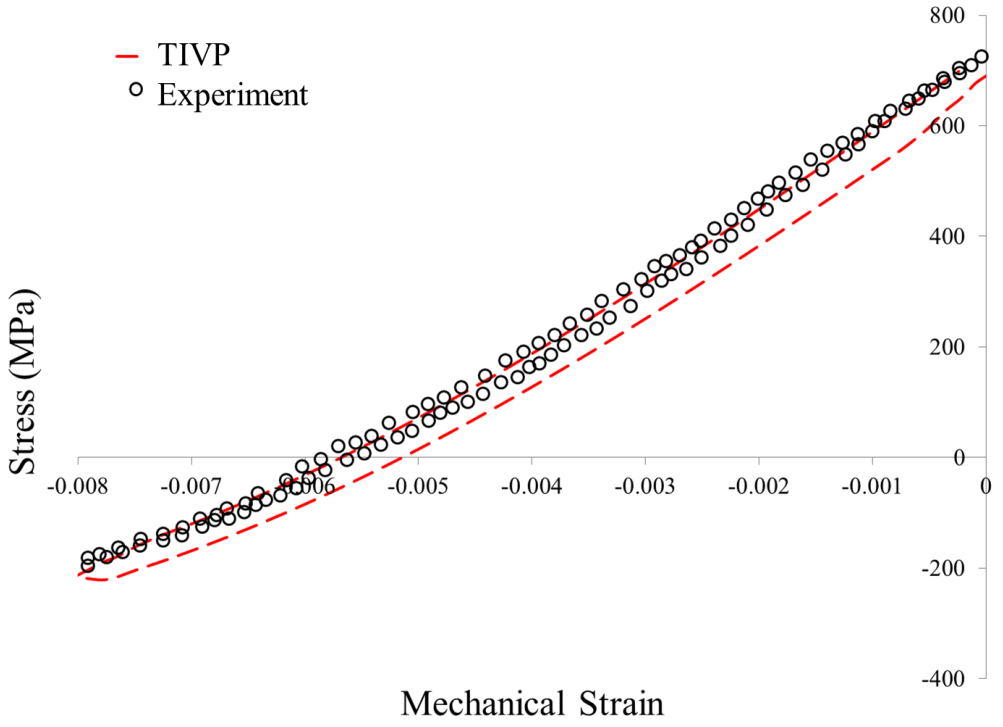

Figure 3.30: Mid-life cycle comparison under OP TMF conditions for single element, 0.008 strain range, min. temp. 100°C, max. temp 950°C, $R_\epsilon = -\infty$

CHAPTER IV

DEVELOPMENT OF AN EXTREME REDUCED ORDER MICROSTRUCTURE SENSITIVE CONSTITUTIVE MODEL

4.1 Introduction

For design of components at a systems level, a rapid first-order estimate of material response is sometimes more useful than full finite element simulations which incorporate advanced material models. The ability to predict endpoint stresses almost instantaneously under a variety of loading conditions can be beneficial to designers, especially when strain-based life models are employed to predict component life. Current methods to predict inelastic strain range and mean stresses, such as Neuber or Glinka approaches, do not capture the effects of material anisotropy or rate dependence, nor do they capture any microstructural dependence. To address this need, an extreme reduced order microstructure-sensitive constitutive model was developed through utilizing the function-fitting capabilities of a feedforward artificial neural network (ANN). This ANN model is capable of predicting isothermal behavior of a directionally solidified Ni-base superalloy through predicting Ramberg-Osgood model parameters for the temperature range 20-1050°C at arbitrary off-axis loading scenarios from longitudinal to transverse material orientations and strain rates ranging from 10^{-3} to 10^{-8} s^{-1}. These responses are then used to predict endpoint stresses under in-phase (IP) and out-of-phase (OP) thermomechanical (TMF) loading conditions and are used to analyze notch features in engineering components.

4.2 Background

In order to capture the response of a Ni-base superalloy in a format suitable for ANN prediction, isothermal, uniaxial monotonic data generated from a more complex, physics-based crystal viscoplasticity (CVP) model [60] was fitted to a simple 1-D Ramberg-Osgood relation. The parameters obtained through this process, each capturing temperature, rate,

and orientation effects, were used to construct a training set for an artifical neural network. Figure 4.1 outlines the methodology for deveoping this extreme reduced order model and is based on the work done by Shenoy et al. [57].

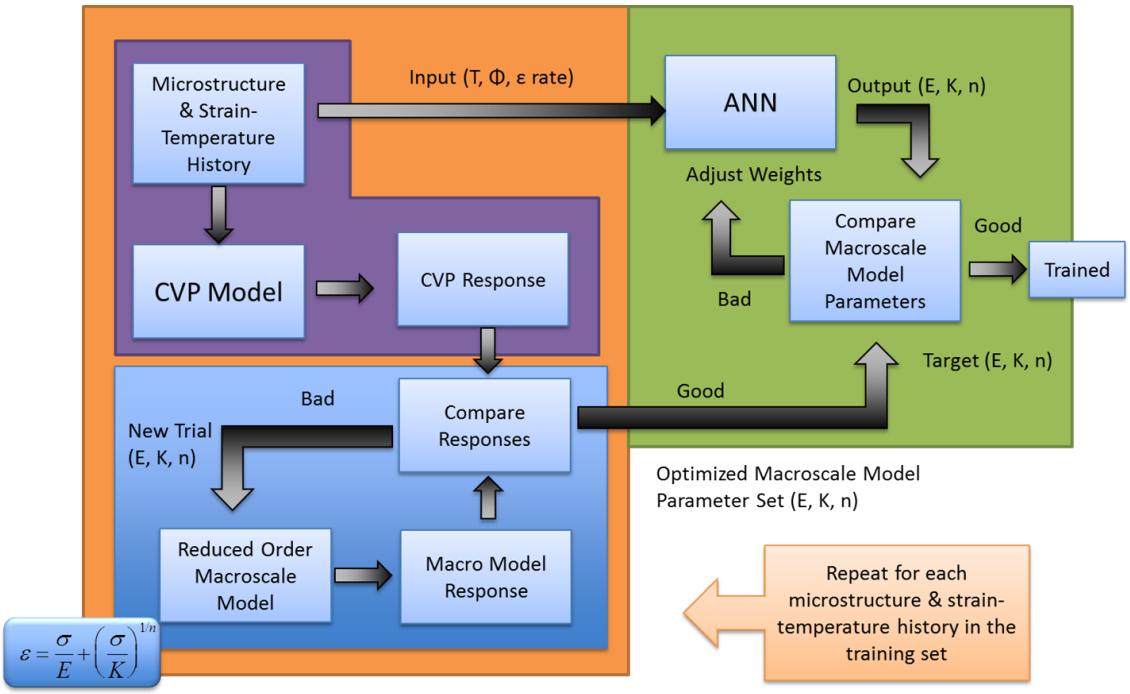

Figure 4.1: Training methodology for ANN model

Artificial neural networks have been used to solve problems of different type and levels of complexity [66] and have been applied to problems in the materials science field such as predicting material properties [55, 67, 68] and material behavior [51, 54, 56, 69]. A typical feedforward ANN layout is shown in Figure 4.2.

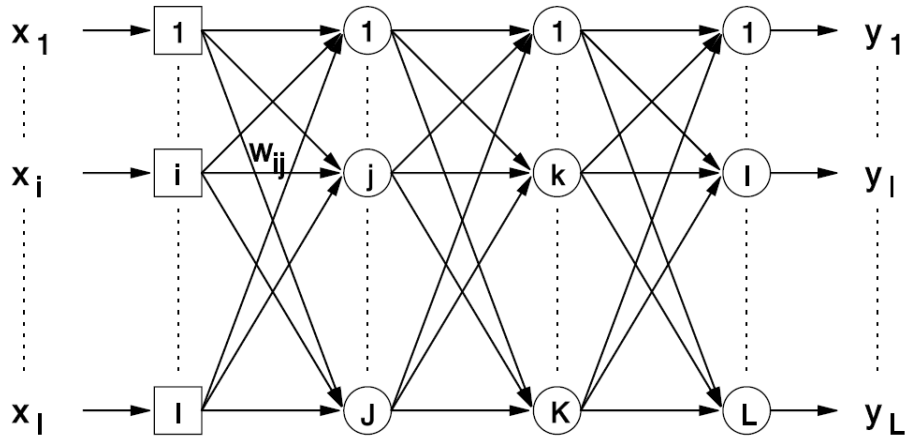

Figure 4.2: A typical multilayer feedforward artificial neural network layout [47]

Yagawa and Okuda [48] summarize the advantages of using hierarchical feedforward artificial neural networks as follows:

- One can automatically construct a nonlinear mapping from multiple input data to multiple output data in the network through a learning process of some or many sample input vs. output relations.
- The network has a capability of the so-called "generalization", i.e. a kind of interpolation, such that the trained network estimates appropriate output data even for unlearned input data.
- The trained network operates quickly in an application phase. The CPU power required to operate it may be equivalent only to that of a personal computer.

An ANN consists of group of processing elements called neurons (also called nodes or units) which are arranged in successive layers and receive inputs from other neurons as the signal works forward from an input layer to an output layer. Once an input is received by

a neuron from another neuron in the previous layer, it is multiplied by a synaptic weight and added to a bias value.

$$v_j = \sum w_{ij} y_i + b_j \tag{4.1}$$

where v_j is the sum of the weighted input signals, w_{ij} is the synaptic weight between neurons i and j, and b_j is the bias associated with neuron j. The scalar output from hidden layer neuron j is given by a tan-sigmoidal activation function.

$$y_j = \frac{2}{1 + e^{-2v_j}} - 1 \tag{4.2}$$

where y_j is the output signal from neuron j. In the output layer, the activation function for neurons is a simple linear function.

$$y_j = v_j \tag{4.3}$$

It has been proven that a single hidden layer feedforward ANN can map between any m and n dimensional space to any desired degree of accuracy, provided there is a sufficient amount of neurons in the hidden layer [70] although they are not necessarily as efficient as networks with multiple hidden layers [66].

4.3 ANN Implementation

The isothermal response from the CVP model was fitten to a Ramberg-Osgood relation [11], given by

$$\epsilon = \frac{\sigma}{E} + \left(\frac{\sigma}{K}\right)^{\frac{1}{n}} \tag{4.4}$$

in monotonic form and

$$\Delta\epsilon = \frac{\Delta\sigma}{E} + 2\left(\frac{\Delta\sigma}{2K'}\right)^{\frac{1}{n'}} \tag{4.5}$$

in cyclic forms [12]. The data in this exercise consists of 605 simulations in which temperature, strain rate, and material orientation were varied. Since CM247LC-DS is cyclically stable, the monotonic responses are used to approximate the cyclic stress-strain curve.

$$\Delta\epsilon = \frac{\Delta\sigma}{E} + 2\left(\frac{\Delta\sigma}{2K'}\right)^{\frac{1}{n'}} \tag{4.6}$$

where ϵ and $\Delta\epsilon$ are the strain and increment in strain, respectively, σ and $\Delta\sigma$ are the stress and the increment in stress, respectively, E is the elastic modulus, K is a strength coefficient, and n is an exponent which characterizes strain hardening. To fit the CVP data to the simplified Ramberg-Osgood model, MATLAB [71] was used to determine the values of E, K, and n using linear regression. This is accomplished by separating the elastic and plastic portions of the stress-strain curve,

$$\Delta\epsilon^e = \frac{\sigma}{E} \tag{4.7}$$

and

$$\Delta\epsilon^p = \left(\frac{\sigma}{K}\right)^{\frac{1}{n}} \tag{4.8}$$

respectively, where $\Delta\epsilon^e$ and $\Delta\epsilon^p$ are the increments in elastic and plastic strains, respectively. In MATLAB, linear regression was first used to find the modulus using the elastic portion of the curve, then K and n were determined by applying a linear regression fit to log $\Delta\sigma$ versus log $\Delta\epsilon^p$ [72].

The training set for the ANN is composed of these values of E, K, and n, which are set as targets corresponding to their respective temperatures, strain rates, and orientations with respect to the $\langle 001 \rangle$ direction. A total of 605 data points form the training set, where the strain rate was replaced by its log in base 10 for linearization.

For the network architecture, two hidden layers, each with 12 neurons, are chosen and encompassed by an input and output layer of three neurons each. A schematic of this ANN is shown in Figure 4.3. Although it would be preferable to perform a convergence study in order to determine a more optimal ANN architecture, it is beyond the scope of this research

and, consequently, a large enough network to capture the nonlinear relations between input and output variables is selected. Certain training methods are utilized to prevent overfitting and are discussed in section 4.4.

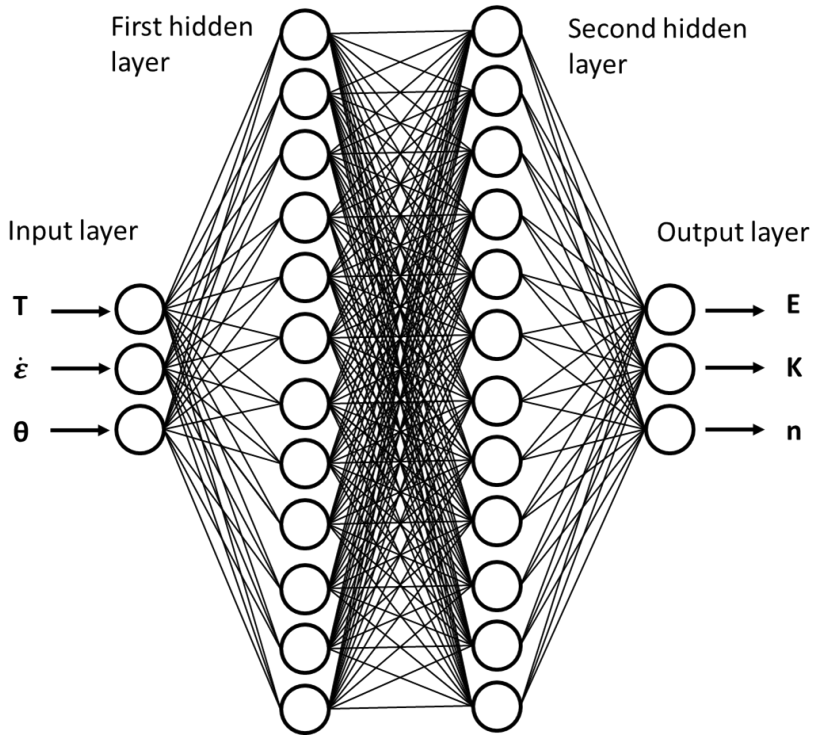

Figure 4.3: Schematic of ANN used for extreme reduced order model

The Neural Network Toolbox in MATLAB [71] is used to generate and train the ANN. Generally the data is divided into three sets when training ANNs: one each for training, validation, and testing. The training set is used to update the weights and biases during the backpropagation training method. The validation set is used to check for overfitting by monitoring its error, and training is ended when the error associated with the validation set begins to rise after a specified number of iterations. The test set is never seen by the ANN until training is complete and is used to check the accuracy of the trained ANN. In this exercise, 90% of the data was used for training and 10% used for testing. There is no general agreement on how much data should be placed into these sample groups when training ANNs [73].

4.4 Training

For training, the backpropagation technique is applied [74] in which the connection weights and biases of the neurons in the hidden layers are adjusted so as to minimize the difference between the target values and the network output. Bayesian regularization [75] is used within a Levenberg-Marquardt algorithm to train the ANN while minimizing overfitting. To track error, two measurements were used. The first, MSE, is the mean squared error defined as

$$MSE = \frac{1}{N}\sum_{i=1}^{N}(t_i - a_i)^2 \tag{4.9}$$

Although MSE is used to measure performance during training, predictive performance of the ANNs is eventually measured using mean relative error, MRE, defined as

$$MRE = \frac{1}{N}\sum_{i=1}^{N}\left|\frac{t_i - a_i}{t_i}\right| \tag{4.10}$$

where N is the number of points in the training set, t_i is the target value of the parameter under consideration, and a_i is the value predicted by the ANN corresponding to the same inputs as the target value t_i. This has been used as a measure of performance for very similar applications of ANNs [55,76,77] and is chosen because it is a more intuitive measure of error.

Overfitting is one of the most reported problems with ANNs and can occur when the network is too large [73]. Since the performance of the ANN is measured by its accuracy with respect to the targets, a network may show a low error when compared to target values and yet not capture the general trend of the data. This is shown in Figure 4.4 using a test case where a trained ANN is used to fit a sine waveform.

Detecting ANN overfitting may be difficult, especially when the ANN is used to map between higher dimensional spaces. In order to check for overfitting, two of the three input variables are fixed and each output variable plotted as a function of the free independent variable (in effect, this is looking at the projection of the ANN prediction onto several selected subspaces). These functions are then compared to the entire data set and the natural spline

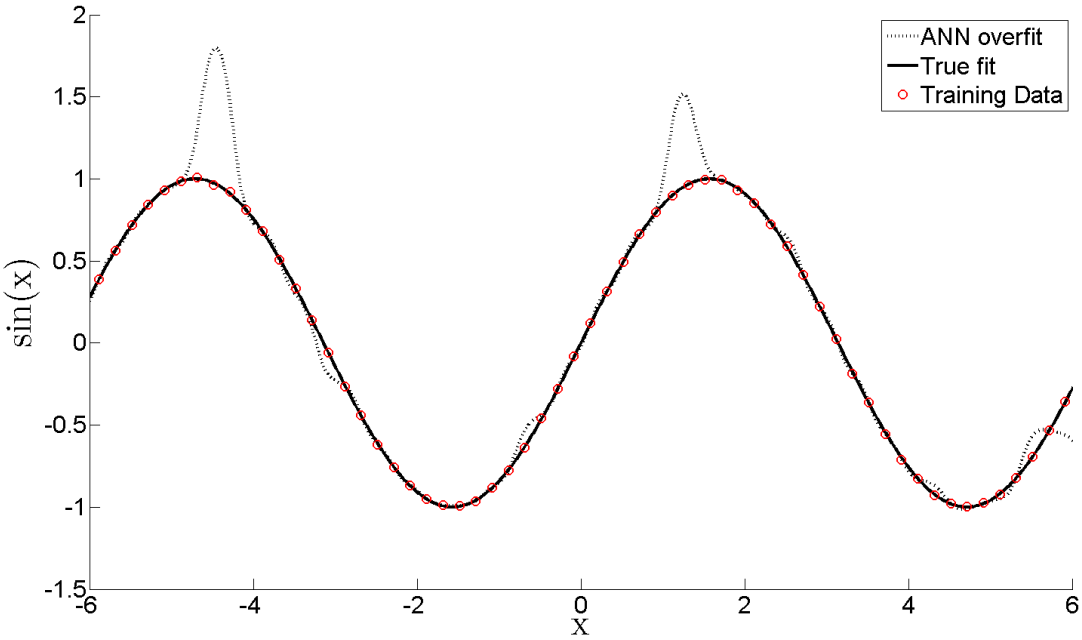

Figure 4.4: Example of ANN overfitting when trained to a sine waveform

interpolating polynomial. An example of this sort of check is shown in Figure 4.5, where the three Ramberg-Osgood parameters are normalized by a constant and are plotted as functions of the off-axis angle in order to compare to points in the data set. These ANN predictions are compared to the natural spline interpolation of the same points to check for consistency.

Although not an absolute standard to which to compare the ANN output, the natural spline seems to serve as a good indicator as to whether or not the ANN is capturing the trend of the Ramberg-Osgood parameters as a function of orientation for a given temperature and strain rate. If overfitting is suspected, the ANN may be retrained and checked again in the same manner.

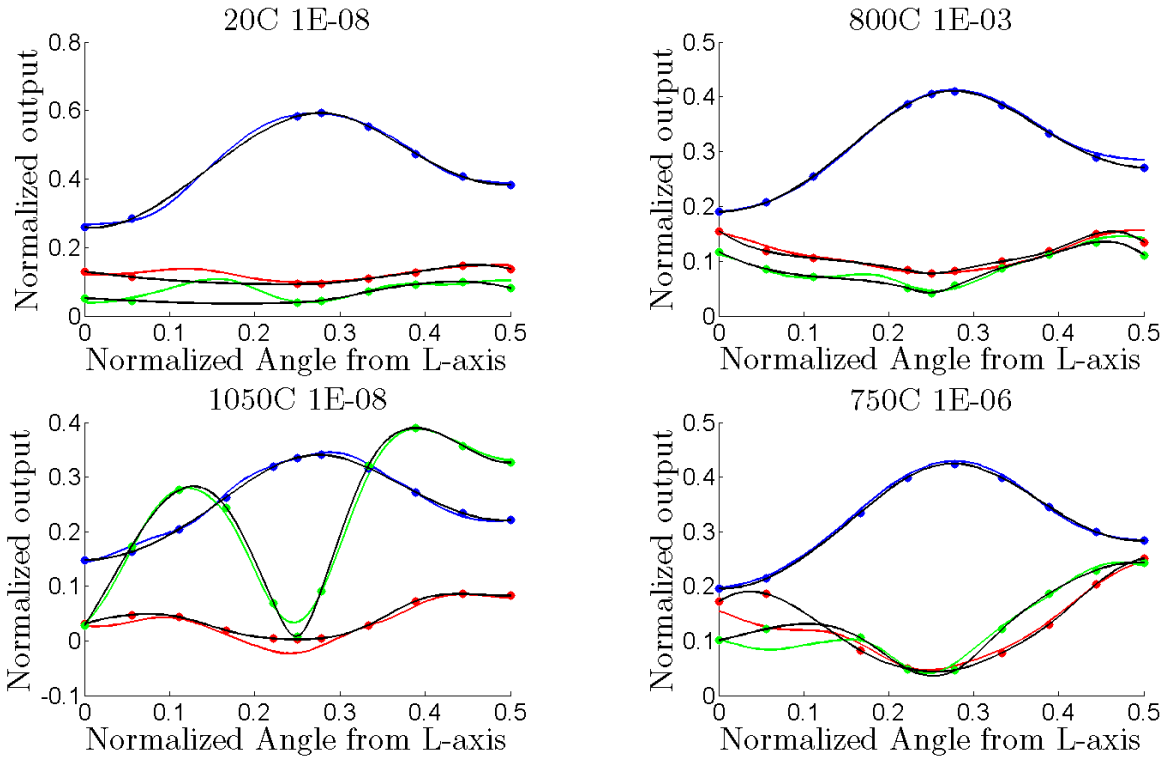

Figure 4.5: Comparisons of ANN prediction to natural splines to check for overfitting

4.5 Results

As mentioned in Section 4.3, the monotonic stress-strain curves produced by the CVP model are assumed to approximate the cyclic stress-strain curves, i.e. $K' = K$ and $n' = n$. The trained ANN shows good correlation with the CVP model predictions at arbitrary temperatures, strain rates, and orientations, since these effects are captured in the Ramberg-Osgood parameters. A few comparisons between the responses predicted by the CVP and ANN are shown in Figures 4.6 through 4.8, using Massing's hypothesis [78] to generate cyclic curves.

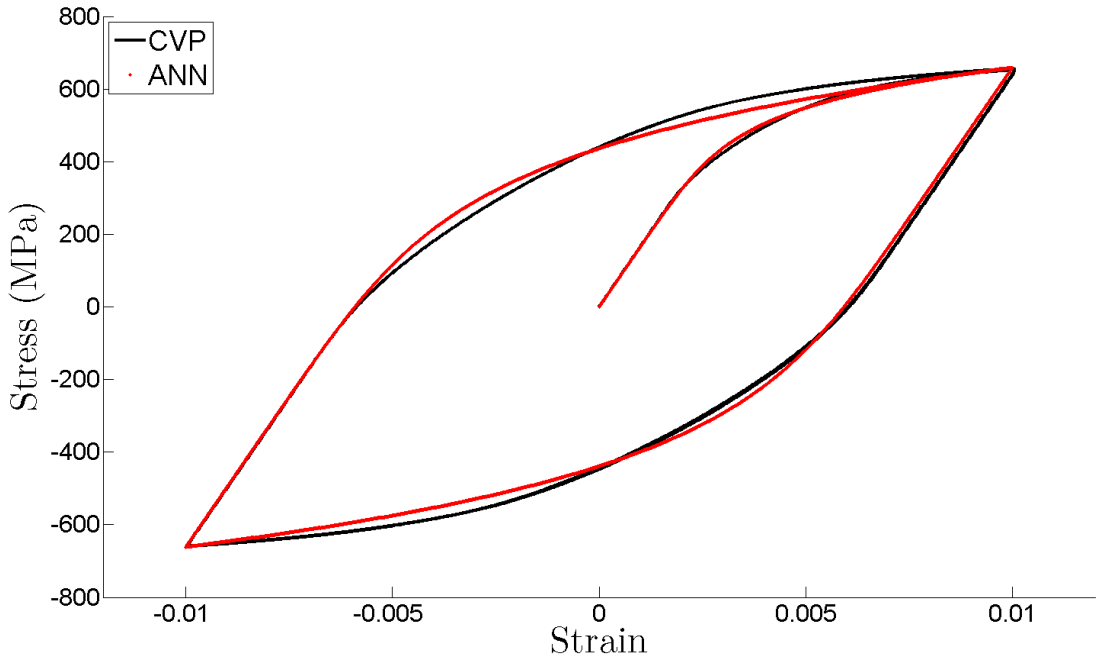

Figure 4.6: Comparisons of CVP and ANN predictions at 623°C, $2 \cdot 10^{-5} s^{-1}$, 78° off-axis

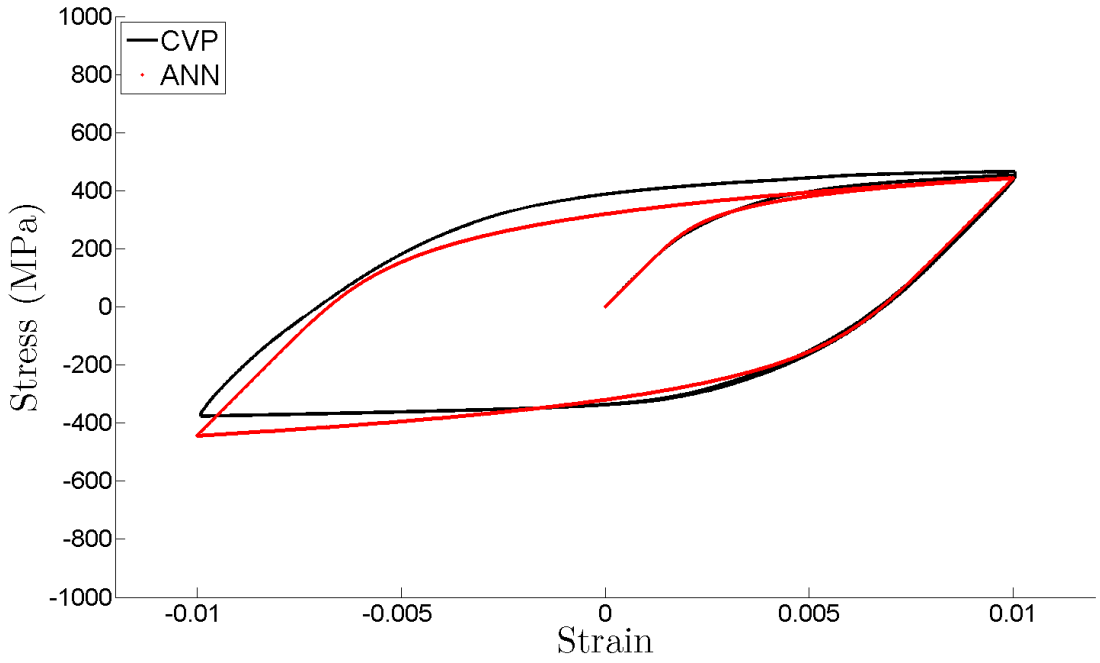

Figure 4.7: Comparisons of CVP and ANN predictions at 886°C, $5 \cdot 10^{-6}$ s^{-1}, 27° off-axis

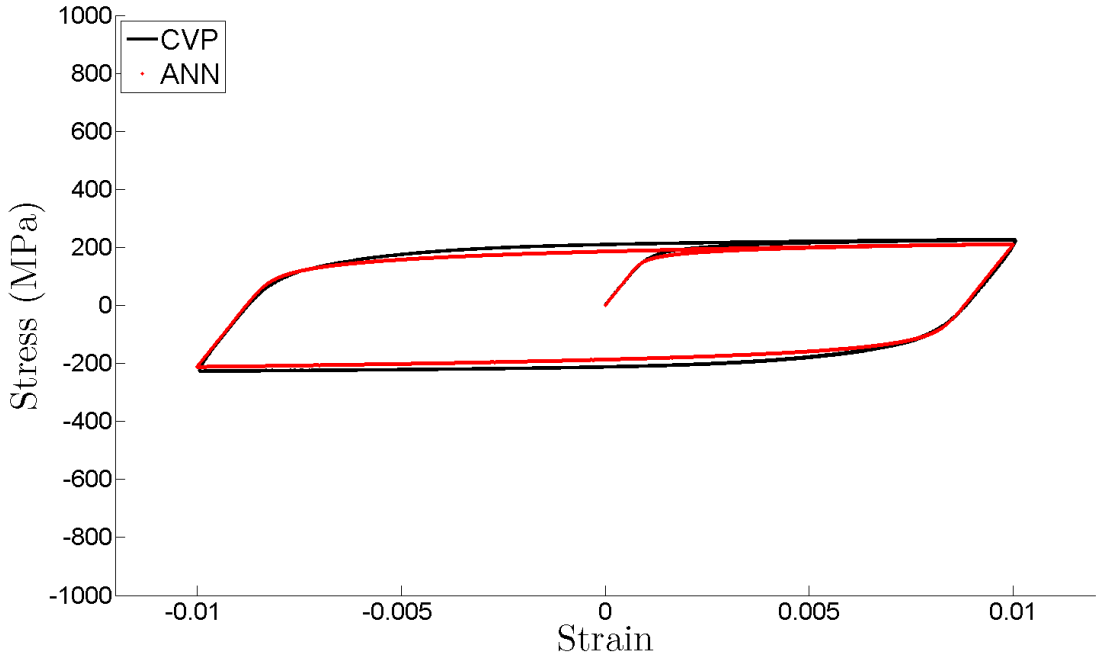

Figure 4.8: Comparisons of CVP and ANN predictions at 1031°C, $5 \cdot 10^{-4}$ s^{-1}, 53° off-axis

To predict TMF response for fully reversed cycling (i.e. $R_\epsilon = -1$), the isothermal curves of the endpoint temperatures were used to approximate the stresses at the endpoints, in the manner of Skelton et al. [59]. An example of this sort of prediction is shown in Figures 4.9 and 4.10.

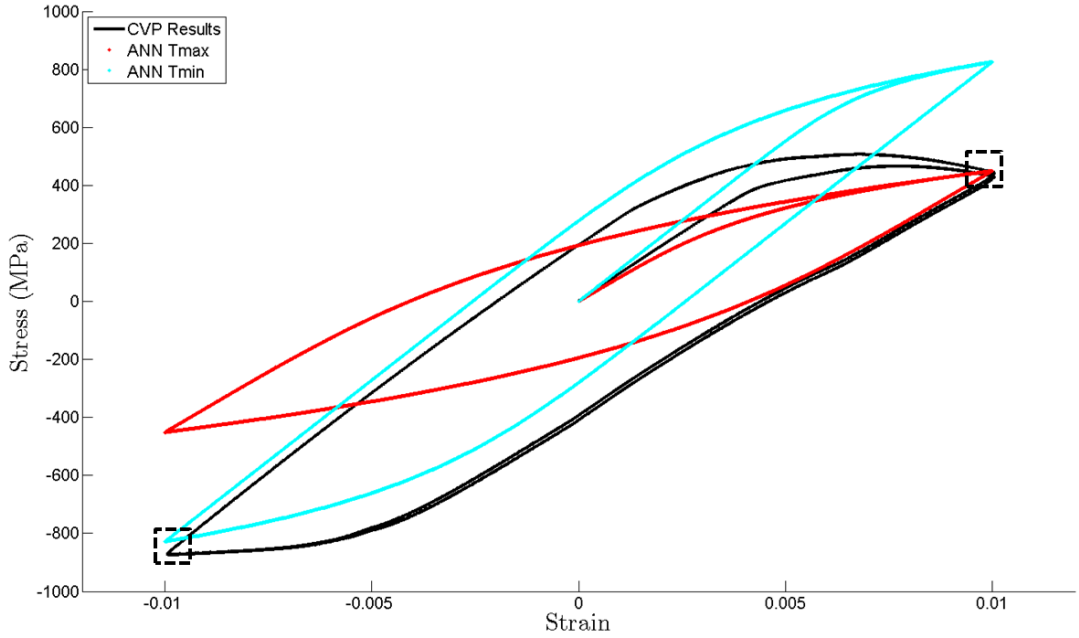

Figure 4.9: Determination of endpoint stresses for 550-950°C IP TMF, $R_\epsilon = -1$

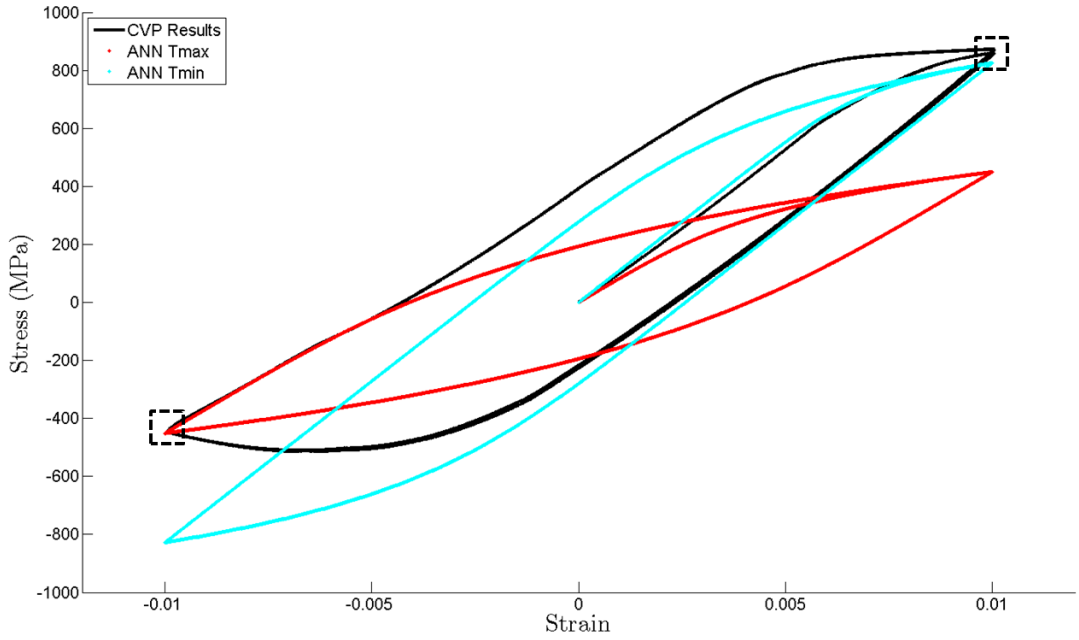

Figure 4.10: Determination of endpoint stresses for 550-950°C OP TMF, $R_\epsilon = -1$

Under strain ratios of $R_\epsilon = 0$ and $R_\epsilon = -\infty$, the isothermal curve endpoint of the temperature at loading endpoint is taken, and the material is assumed to unload elastically with an effective modulus at a mean temperature. This approach appears to work well in approximating the stabilized hysteresis loop for these strain ratios, as seen in Figures 4.11 through 4.12.

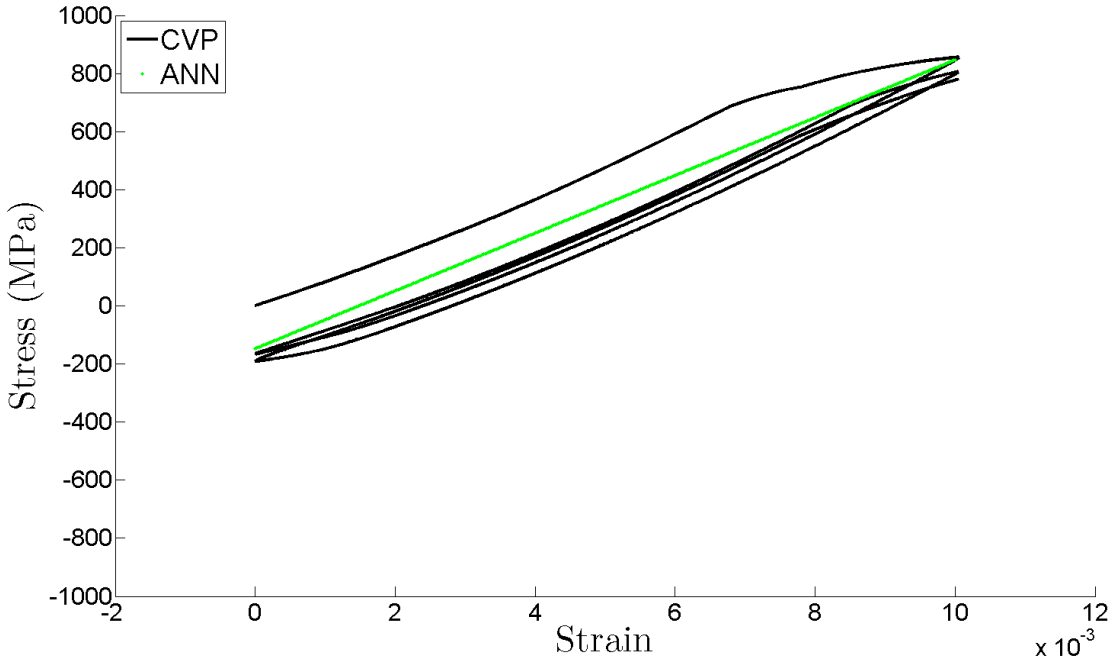

Figure 4.11: Determination of stabilized hysteresis loop for 550-950°C OP TMF, $R_\epsilon = 0$

To predict the hysteresis curves at half life, an equivalent loading ramp method was used. The strain rate given to the ANN was equivalent to the strain amplitude divided by the equivalent cycle time at half life. Comparisons between the mid-life approximation using the ANN model and experimental results are shown in Figures 4.13 and 4.14.

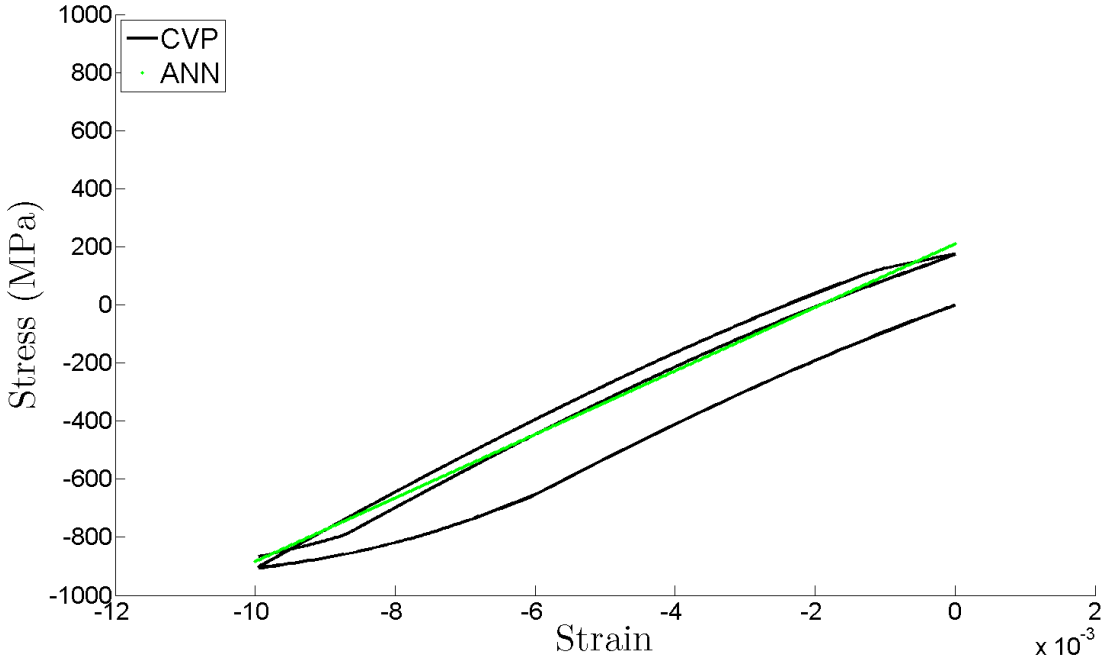

Figure 4.12: Determination of stabilized hysteresis loop for 327-892°C IP TMF, $R_\epsilon = -\infty$

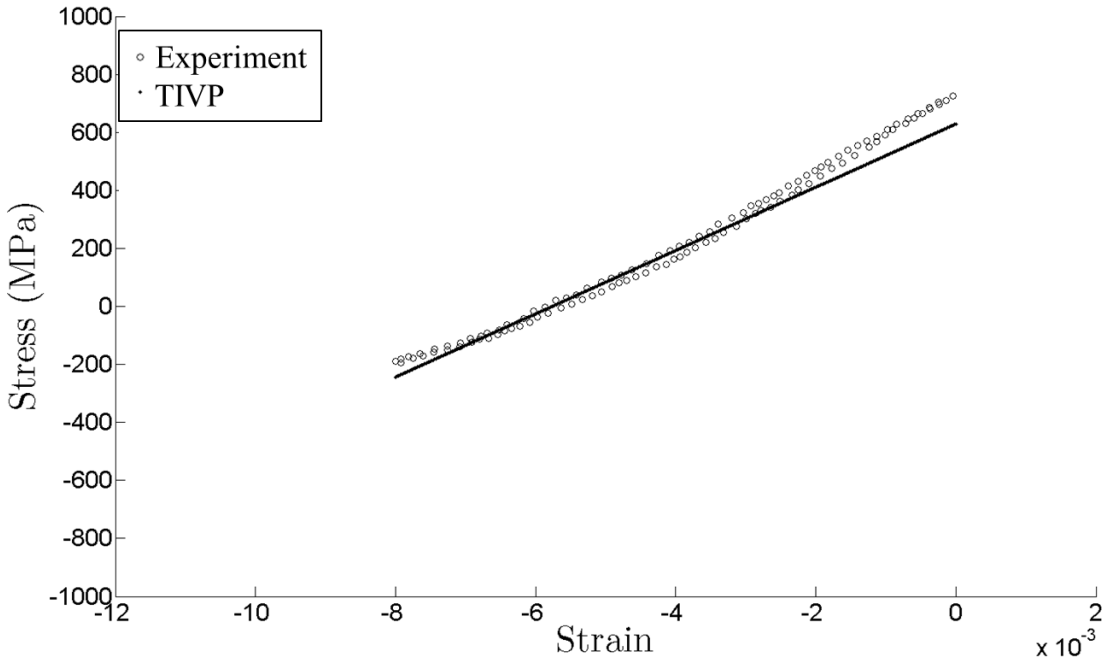

Figure 4.13: Mid-life hysteresis loop at 903 cycles, mean stress and endpoint stress approximation using ANN model compared to experiment, 100-950°C OP TMF, $R_\epsilon = -\infty$, $\Delta\epsilon = 0.8\%$

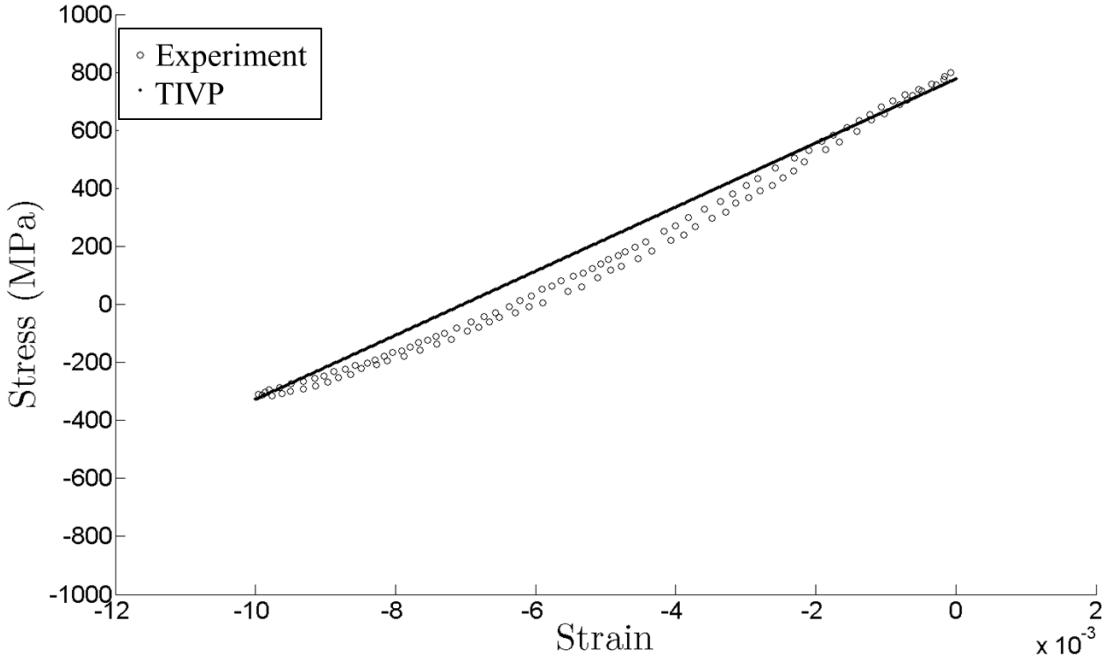

Figure 4.14: Mid-life hysteresis loop at 377 cycles, mean stress and endpoint stress approximation using ANN model compared to experiment, 100-950°C OP TMF, $R_\epsilon = -\infty$, $\Delta\epsilon = 1\%$

4.6 Extension to Component Analysis

In order to extend the functionality of the extreme reduced order model to a component level, a Neuber-type analysis method is proposed, outlined in Figure 4.15. This would involve conducting a trnsversely isotropic elastic finite element analysis of the component in question in order to determine the local of the highest stressed element.

The basis for this method is identifying the highest stressed element in the component model and using it as a limiting factor for the entire component. For example, to illustrate, a cylindrically-notched specimen model is studied. The highest stressed element would likely occur on the surface at some angle from the notch root in a DS alloy. Knowing that one side of the element is the free surface, the direction of principal stresses is known, and the information for the highest stressed element concerning temperature, orientation, and strain rate may be passed into the ANN model to give the approximate Ramberg-Osgood curve for that element. These curve endpoints can be used to determine peak endpoint stresses and strains for the element, in addition to mean stresses. This information could be used in a strain-based lifing approach such as Neuber's rule.

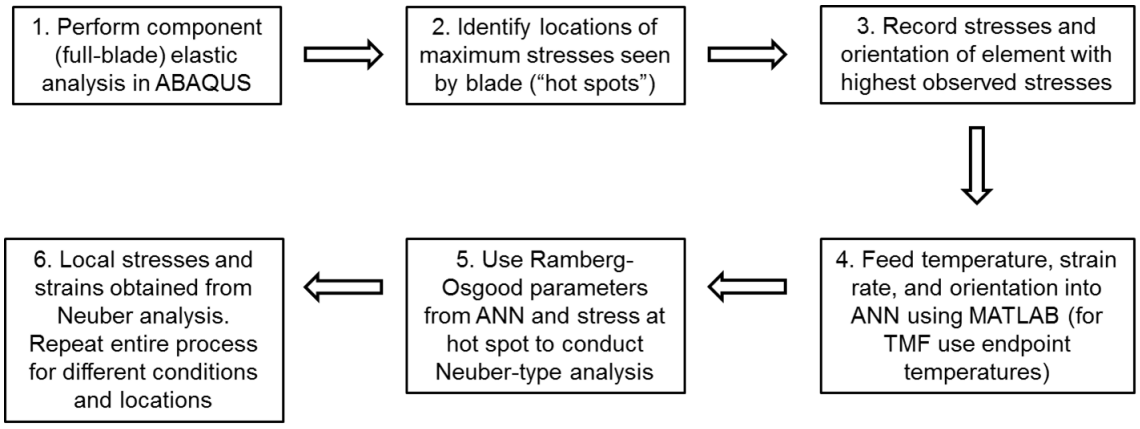

Figure 4.15: Procedure for component analysis using ANN

Although plane stress conditions are assumed for uniaxial tests, plane strain conditions may dominate at the notch root if the notch radius is sufficiently small [72, 79, 80]. In these cases, biaxial stress conditions are present and the principal stress-strain relation can be modified accordingly. One modification suggested by Dowling et al. [81] is given as

$$\frac{\Delta\epsilon_1}{2} = \frac{\Delta\sigma_1}{2E} + \left(\frac{\Delta\sigma_1}{2K'}\right)^{\frac{1}{n'}} \tag{4.11}$$

where

$$\frac{\Delta\epsilon_1}{2} = \frac{\Delta\epsilon}{2}\frac{(1-\mu^2)}{\sqrt{1-\mu+\mu^2}} \tag{4.12}$$

$$\frac{\Delta\sigma_1}{2} = \frac{\Delta\sigma}{2}\frac{1}{\sqrt{1-\mu+\mu^2}} \tag{4.13}$$

$$E_1 = \frac{E}{1-\nu^2} \tag{4.14}$$

and

$$\mu = \frac{\nu + \frac{E\Delta\epsilon_p}{2\Delta\sigma}}{1 + \frac{E\Delta\epsilon_p}{\Delta\sigma}} \tag{4.15}$$

Equation 4.11 is used in conjunction with the Neuber and Glinka relations to approximate the stress-strain behavior of the critical element of a cylindrically notched specimen model with $K_t = 2.0$. The Abaqus FE model is shown in Figure 4.16 and is comprised of 4813 axially symmetric elements (type CAX4) with 4960 nodes.

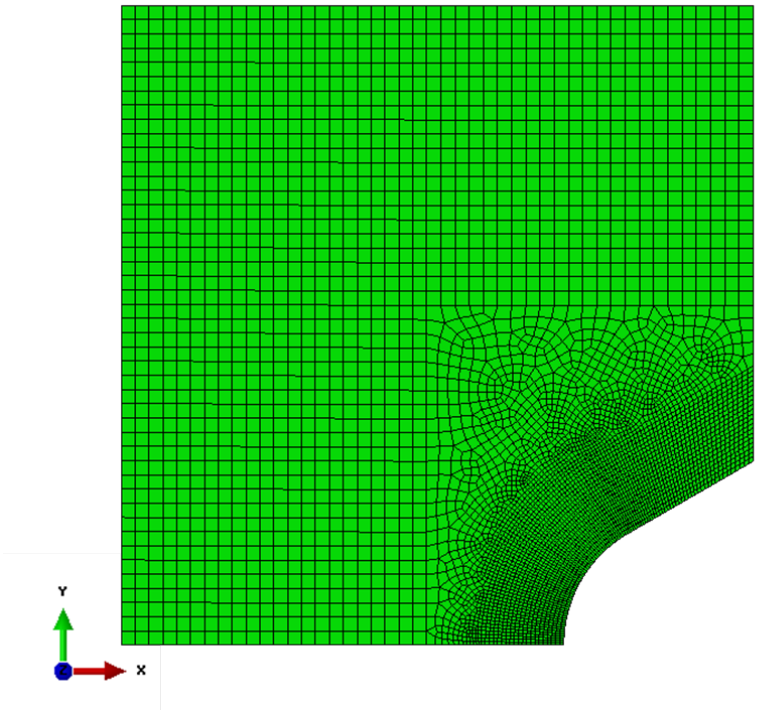

Figure 4.16: FE model of cylindrically notched specimen, $K_T = 2.0$

To verify the approach, an isothermal simulation is conducted using the TIVP UMAT and built-in Abaqus elastic material models at 950°C under completely reversed conditions ($R_\sigma = -1$) with a net section stress amplitude of 250 MPa. The elastic modulus and Poisson's ratio in the longitudinal and transverse orientations, taken from experiment at 950°C, are given to Abaqus in order to define a transversely isotropic elastic material. The methodology outlined in Figure 4.15 is applied in order to approximate the stress-strain behavior of the element with the highest Mises stress in the elastic analysis. Figure 4.17 shows the location of this element at third reversal.

Using the nodal locations of this element, its orientation from the DS axis (the Y-axis in this model) can be determined and given to the ANN in order to acquire the Ramberg-Osgood parameters defining the relation between the principal stresses and strains. These parameters are then used in the Neuber-type analysis to approximate the local response of the element when using the TIVP UMAT by using only the local reponse from the built-in Abaqus elastic analysis.

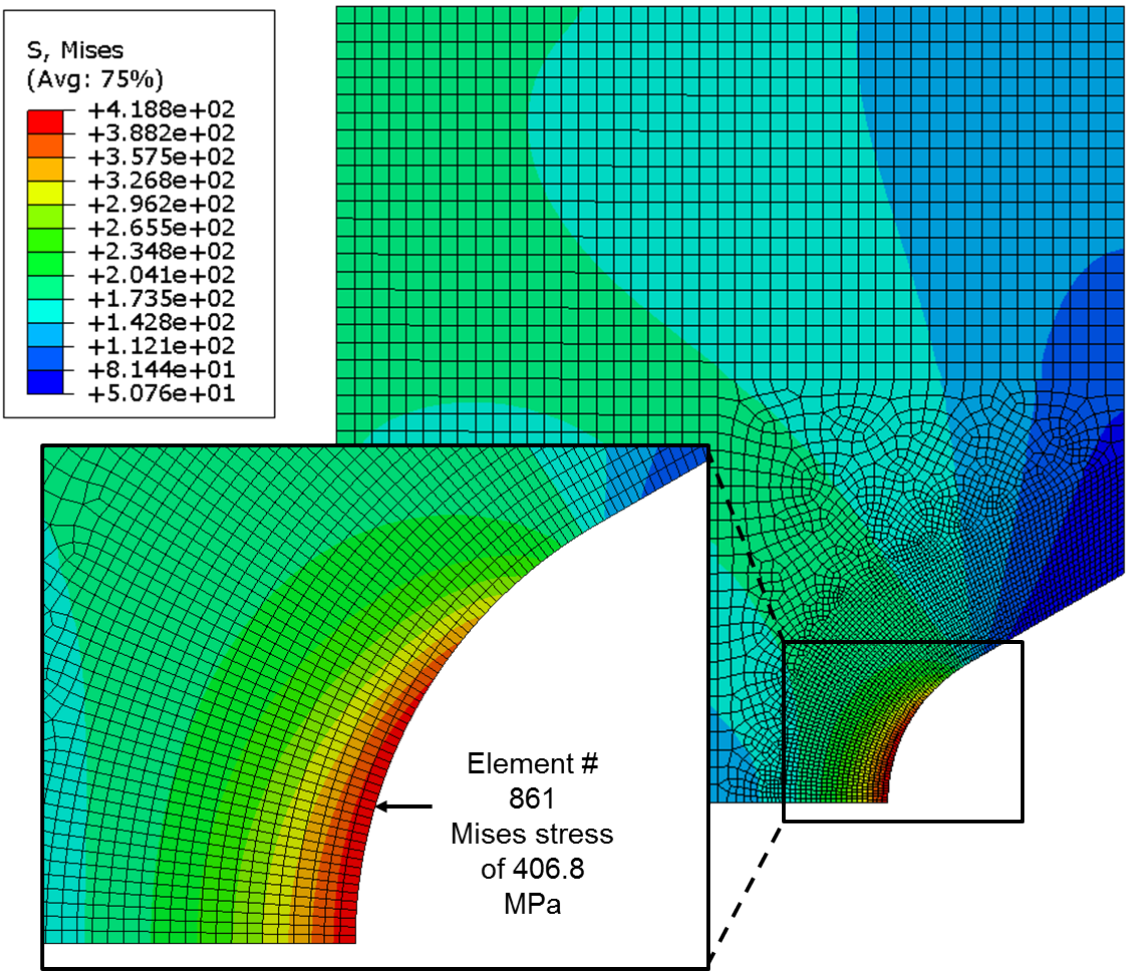

Figure 4.17: Location of element with maximum Mises stress at third reversal, 950°C, $R_\sigma = -1$, $\sigma_a = 250$ MPa

A comparison of these methods is shown in Figures 4.18 and 4.19. Figure 4.18 shows the predicted local response of the element using Neuber's relation with and without modification for plane strain, while Figure 4.19 shows the prediction using Glinka with and without this adjustment. In this case, the Neuber relation with modification for plane strain provides the best approximation to the local response of the critical element. A similar procedure was conducted for a cylindrically notched specimen model of $K_t = 1.7$ at 550°C with 600 MPa net section stress. Results are shown in Figures 4.20 and 4.21, where the Glinka relation with modification for plane strain appears to match more closely.

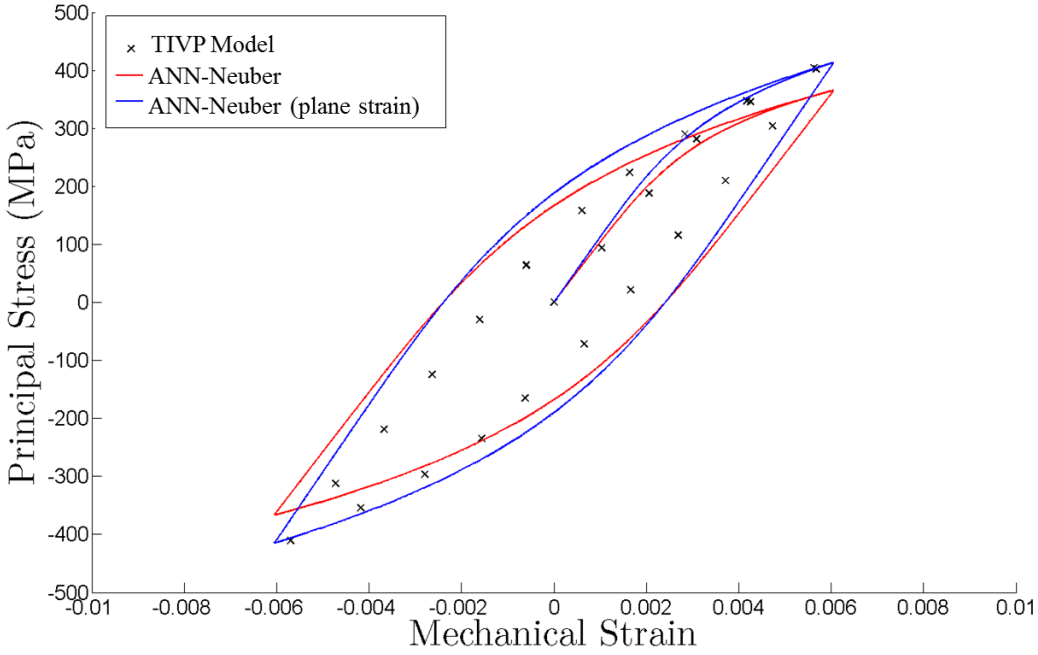

Figure 4.18: Comparison of predicted and actual responses of critical element at third reversal using Neuber relation, 950°C, $R_\sigma = -1$, $\sigma_a = 250$ MPa

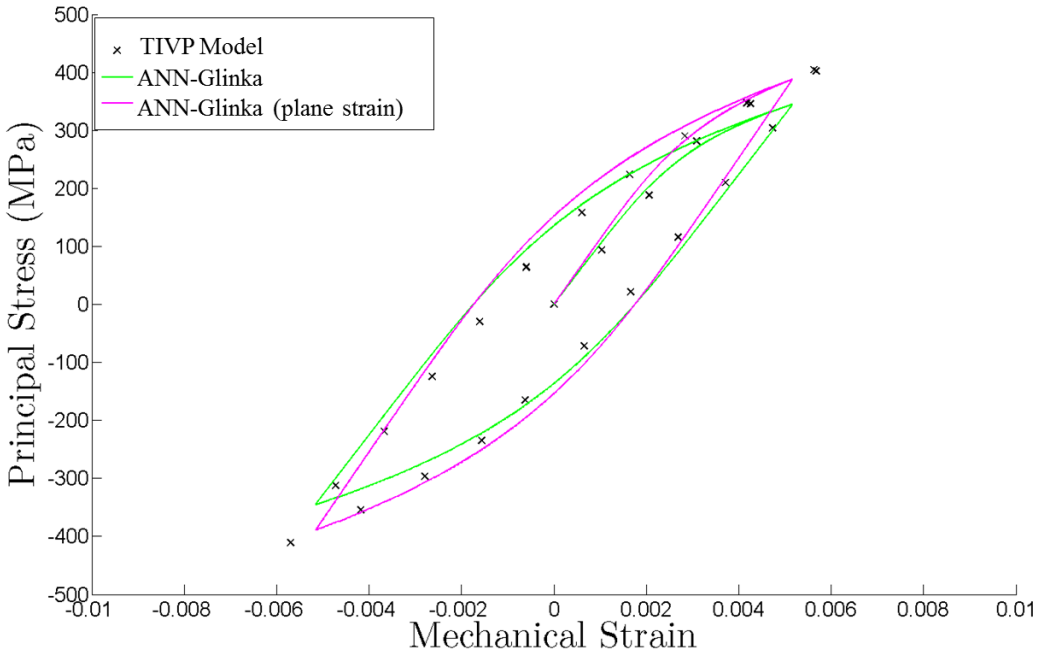

Figure 4.19: Comparison of predicted and actual responses of critical element at third reversal using Glinka relation, 950°C, $R_\sigma = -1$, $\sigma_a = 250$ MPa

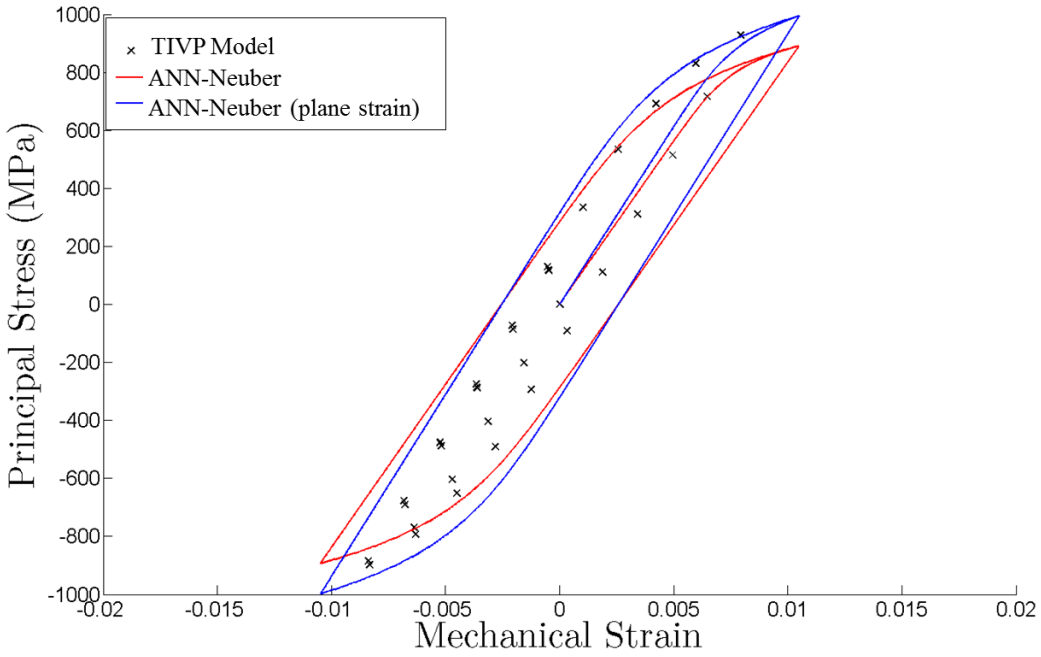

Figure 4.20: Comparison of predicted and actual responses of critical element at third reversal using Neuber relation, 550°C, $R_\sigma = -1$, $\sigma_a = 600$ MPa

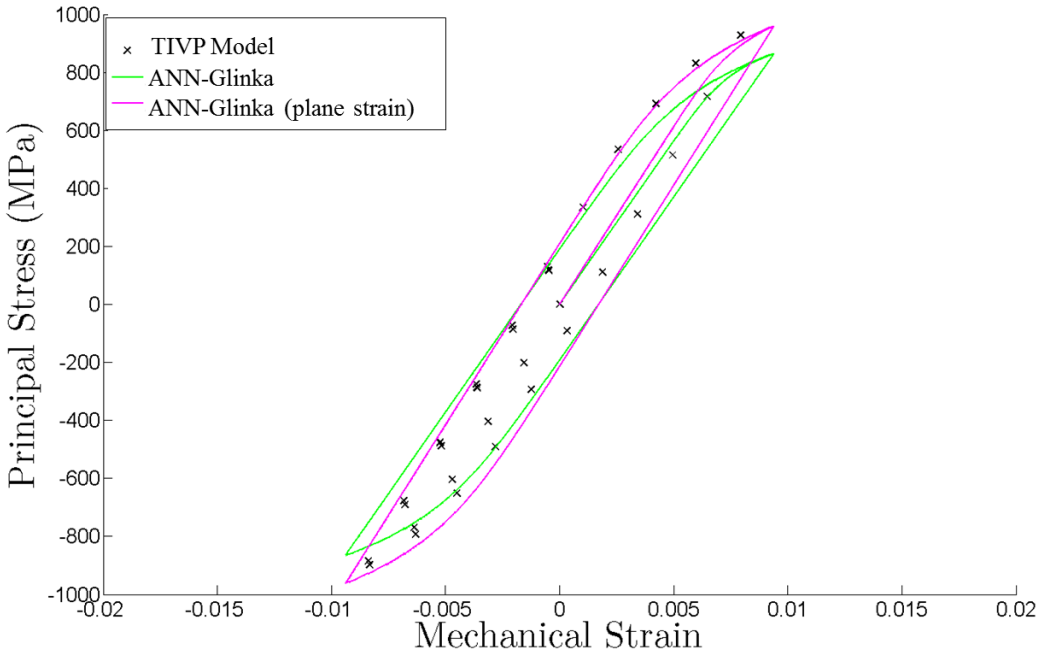

Figure 4.21: Comparison of predicted and actual responses of critical element at third reversal using Glinka relation, 550°C, $R_\sigma = -1$, $\sigma_a = 600$ MPa

For TMF conditions, a similar procedure was conducted, as outlined in Section 4.5, using isothermal stress-strain curves to approximate endpoints of the TMF cycle curves for a critical element. The response of a critical element, along with isothermal predictions at endpoint temperatures, are shown in Figure 4.22 for OP TMF 500-950°C with net section stress amplitude of 300 MPa and $K_t = 2.0$ under completely reversed conditions ($R_\sigma = -1$). Figure 4.23 shows the same comparisons for IP TMF under the same conditions.

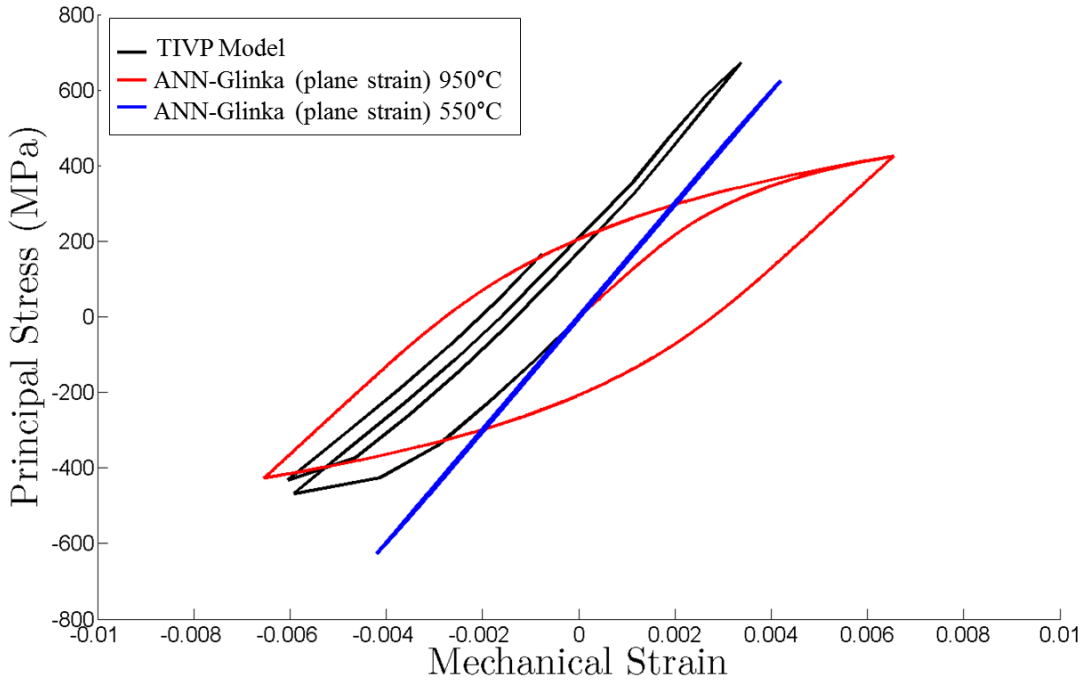

Figure 4.22: Comparison of predicted endpoints and actual response of critical element, OP TMF 500-950°C, $K_t = 2.0$, $R_\sigma = -1$, $\sigma_a = 300$ MPa

Stress levels for this case shown in Figure 4.22 are reasonably well-estimated using the method for completely reversed conditions, although the true ratio R_σ at the critical location is not precisely equal to -1. The predictions do not incorporate ratchetting strain, since the ANN predictions are based on stabilized hysteresis loops. Thus, accuracy will diminish as ratchetting become more and more significant. In the cases presented, it is important to note that the ANN is being compared against a higher-level TIVP model and not against the physically-based CVP model to which it was trained. Thus, any differences in off-axis predictions between the CVP and TIVP models will be implicitly reflected in comparisons

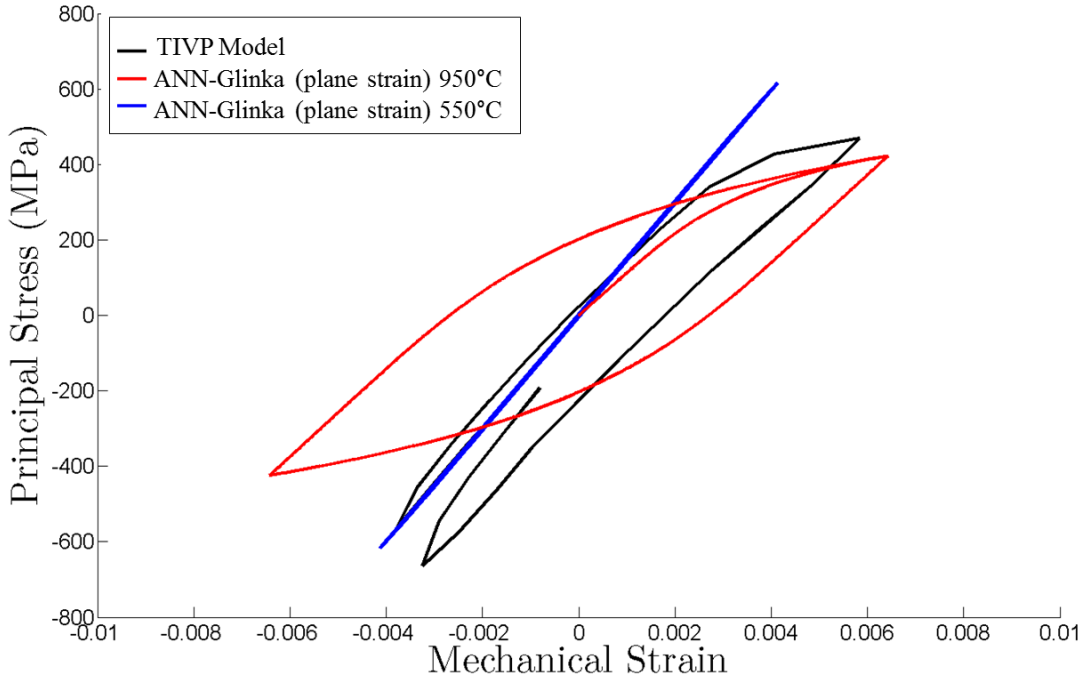

Figure 4.23: Comparison of predicted endpoints and actual response of critical element, IP TMF 500-950°C, $K_t = 2.0$, $R_\sigma = -1$, $\sigma_a = 300$ MPa

between the TIVP and ANN models.

As one moves from a complex physically based model to an extreme reduced order constitutive model of this type, error will inevitably accumulate. Sources of error for this type of model include the degree of fit of the original CVP model to experimental data, the degree of fit of the simple Ramberg-Osgood constitutive relation to CVP simulation data, and the generalization capability of the ANN (i.e. how well the ANN predicts the microstructure-sensitive Ramberg-Osgood parameters). For extension to TMF, the methods outlined earlier deal primarily with typical limiting-case strain ratios, although accounting for other strain ratios may be difficult, as evidenced in the example cases of cylindrically notched specimens under IP and OP conditions.

CHAPTER V

A COMPARATIVE STUDY OF REDUCED ORDER MODELING TECHNIQUES

5.1 Overview

The purpose of this exercise is to demonstrate the capabilities and limitations of the transversely isotropic viscoplasticity (TIVP) model and the extreme reduced order artificial neural network (ANN) model when compared to the more physically-based crystal viscplasticity (CVP) model in a head-to-head comparison. Local responses along a notch root from TIVP and CVP FE simulations are compared to local reponses predicted using the ANN model in conjunction with a Neuber analysis. In this case, a new ANN model was created in a manner similar as before using training data generated by the TIVP model. The complete training set can be found in Appendix B.

5.2 Test case: square plate with circular hole

The component model used for this demonstration case is a square plate with a circular hole at its center, simliar to that presented in Shenoy et al. [6]. The hole has a diameter equivalent to one-tenth of the side length of the plate, whose thickness is one-half the hole diameter. To reduce computational expense, one-fourth of the geometry is modeled in ABAQUS using symmetry boundary conditions and is shown in Figure 5.1. The FE model consists of 2700 three-dimensional, 8-noded C3D8 linear brick elements and 3856 nodes. The $\langle 001 \rangle$ direction of solidification is aligned with the global Z-axis in this model.

In order to simulate the behavior of the entire plate, the two smaller surfaces of the plate model nearest the hole feature (i.e those corresponding to interior surfaces of the entire plate) are assigned symmetric boundary conditions in their respective normal directions. For the first simulation at 950°C, the top surface of the plate is displaced an amount of 0.1 mm corresponding to a nominal strain based on the net section of 0.33% over a time step of 33

seconds, corresponding to an effective nominal strain rate of 10^{-4} s^{-1}.

The second simulation is conducted at 750°C, where the top surface was displaced an amount corresonding to 0.51% nominal strain at the same rate. All other surfaces are traction-free.

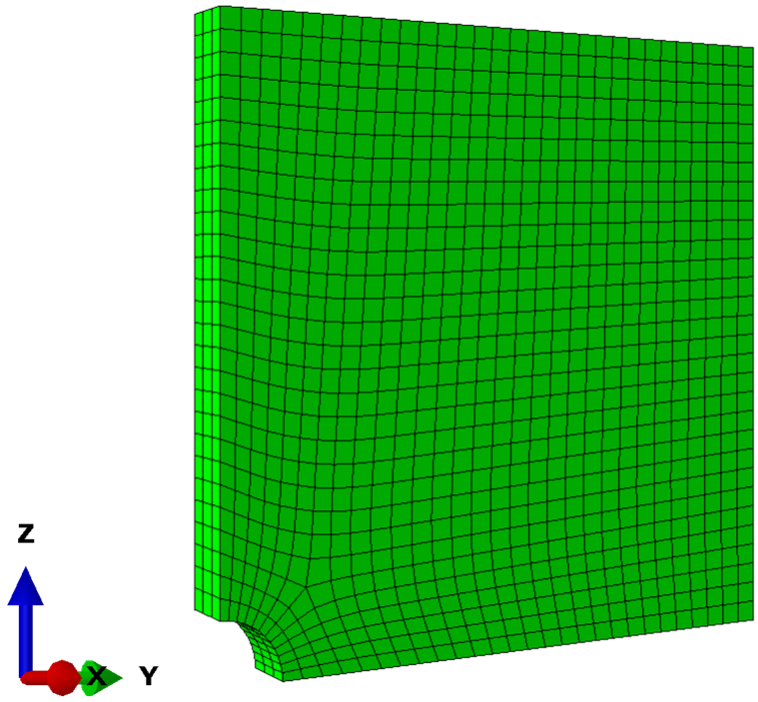

Figure 5.1: Square plate with circular hole at center (one-fourth symmetry model)

5.3 Results

The plate model is run in ABAQUS using both the CVP multi-grain (MG), CVP single crystal (SX) and TIVP material models at 750°C and 950°C. Figures 5.2 through 5.7 show the predictions for the CVP (SX) and TIVP models at 950°C. For the lower temperature of 750°C, predictions are shown in Figures 5.8 through 5.13. Runtimes for both simulations using each UMAT are given in Table 5.1.

Table 5.1: Runtimes for CVP and TIVP with plate model

Model	Temp. (°C)	Runtime (s)	Speed factor relative to CVP (MG)
CVP (MG)	750	72060	1
CVP (SX)	750	16140	4.5
TIVP	750	901	80.0
ANN	750	102	706.5
CVP (MG)	950	62639	1
CVP (SX)	950	14176	4.4
TIVP	950	673	93.1
ANN	950	79	792.9

*Note: MG - multi-grain, SX - single crystal

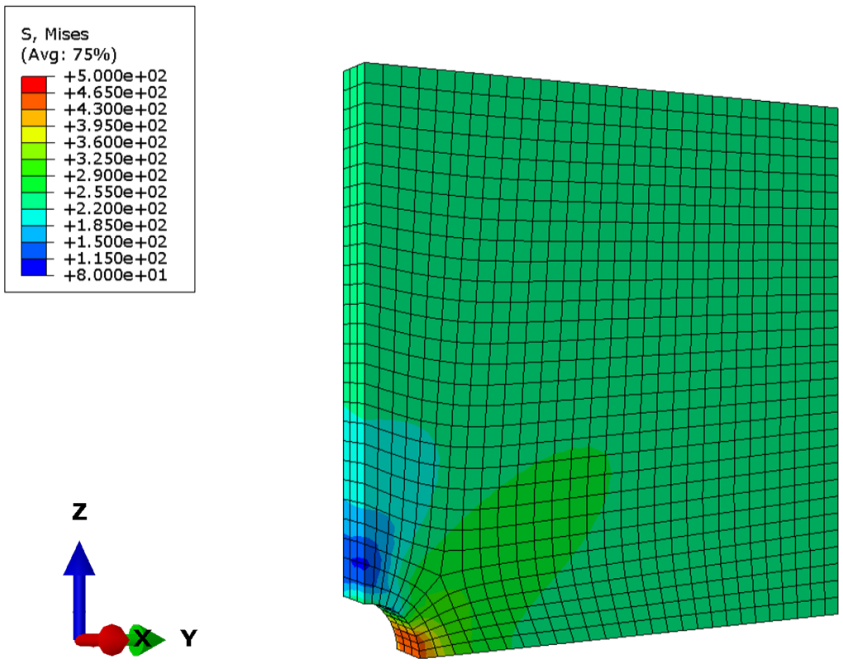

Figure 5.2: CVP (SX) Mises stress (MPa) after tensile loading to 0.33% nominal strain at 10^{-4} s^{-1}, 950°C

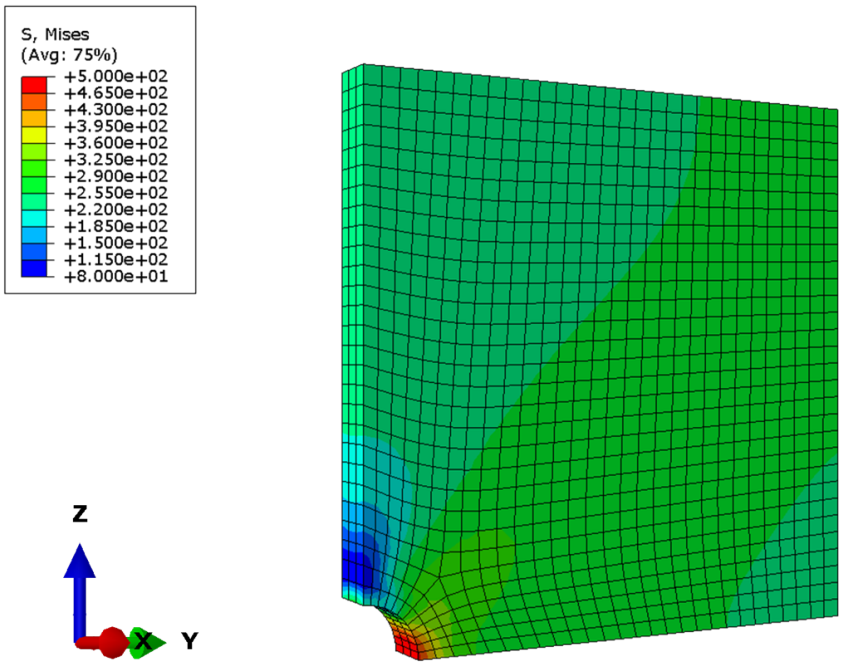

Figure 5.3: TIVP Mises stress (MPa) after tensile loading to 0.33% nominal strain at 10^{-4} s^{-1}, 950°C

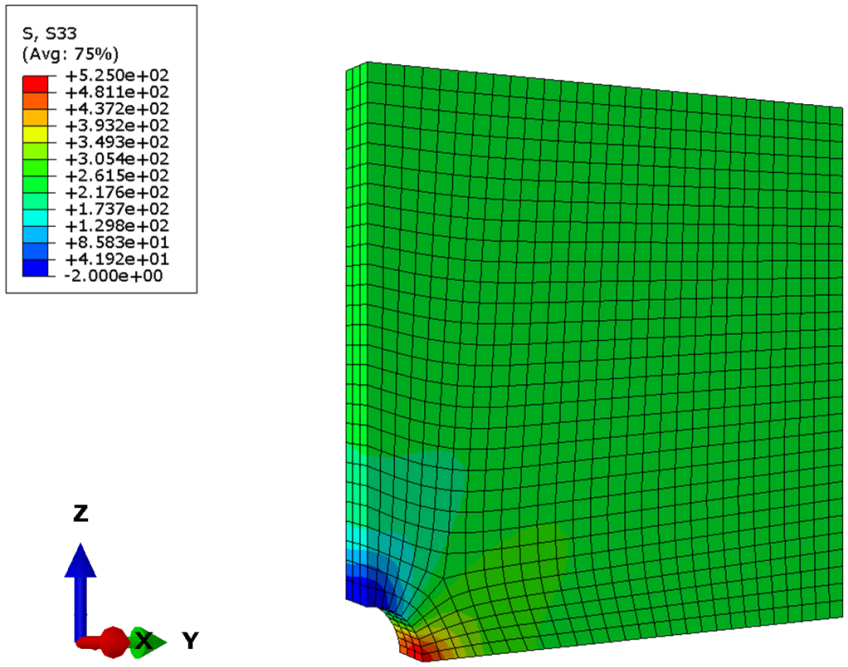

Figure 5.4: CVP (SX) Normal stress (MPa) in Z-direction after tensile loading to 0.33% nominal strain at 10^{-4} s^{-1}, 950°C

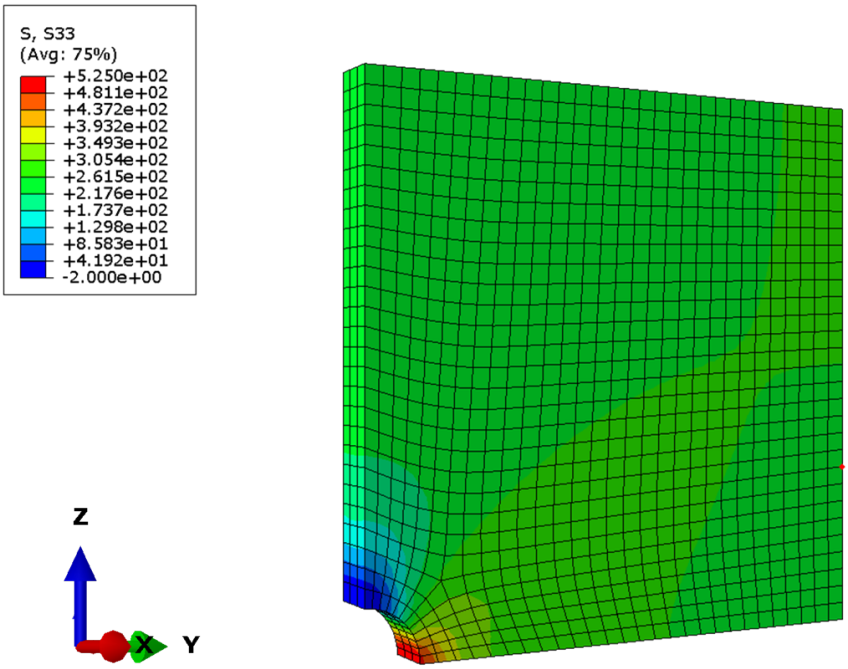

Figure 5.5: TIVP: Normal stress (MPa) in Z-direction after tensile loading to 0.33% nominal strain at 10^{-4} s^{-1}, 950°C

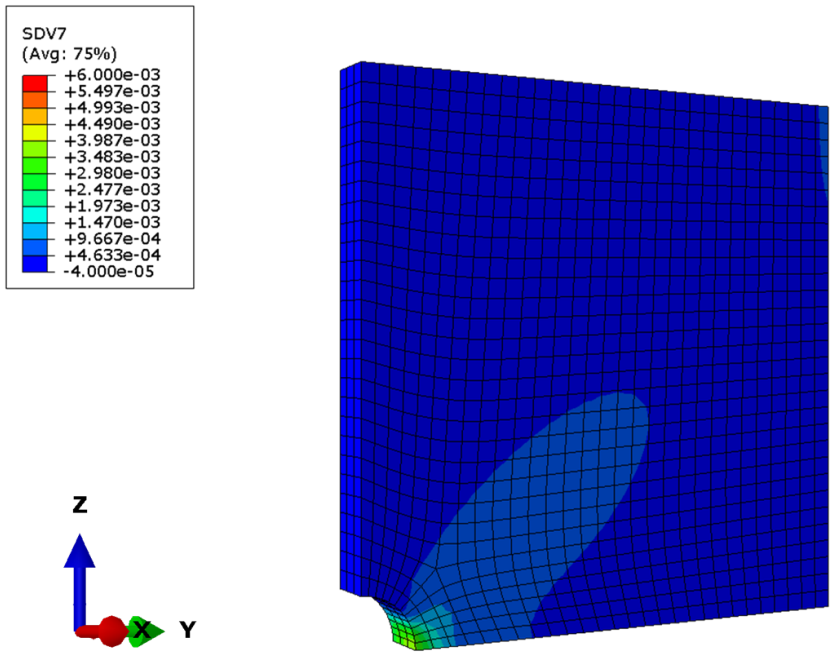

Figure 5.6: CVP (SX) Plastic strain in Z-direction after tensile loading to 0.33% nominal strain at 10^{-4} s^{-1}, 950°C

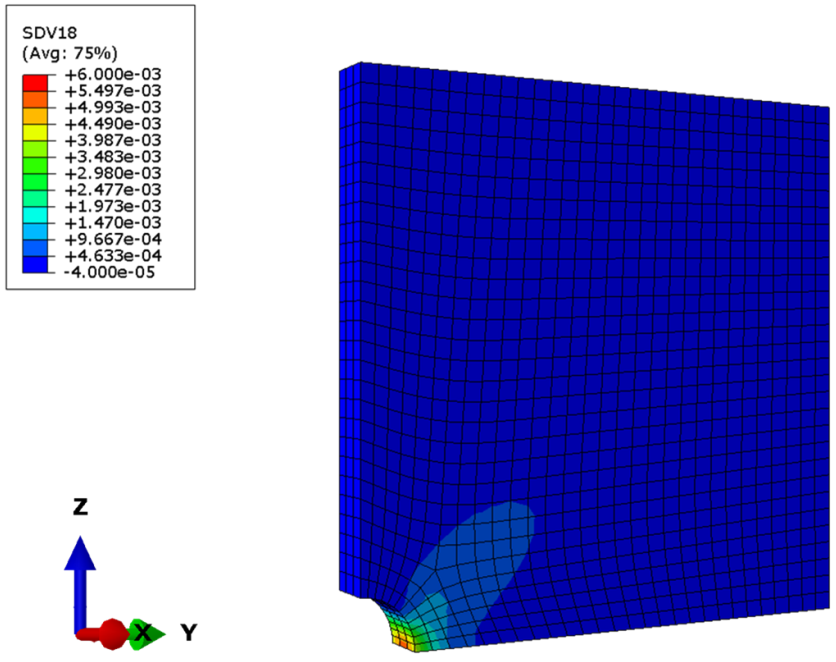

Figure 5.7: TIVP: Plastic strain in Z-direction after tensile loading to 0.33% nominal strain at 10^{-4} s^{-1}, 950°C

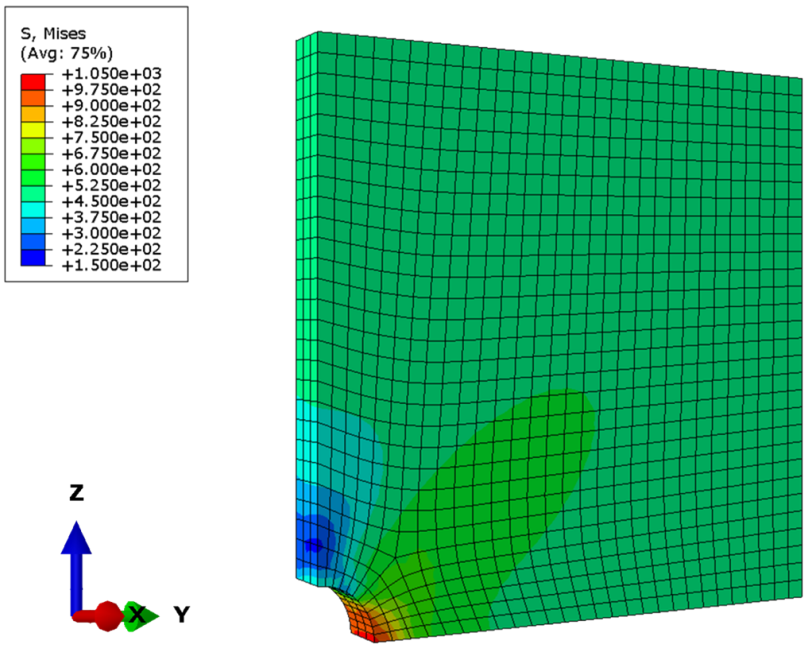

Figure 5.8: CVP (SX) Mises stress (MPa) after tensile loading to 0.51% nominal strain at 10^{-4} s^{-1}, 750°C

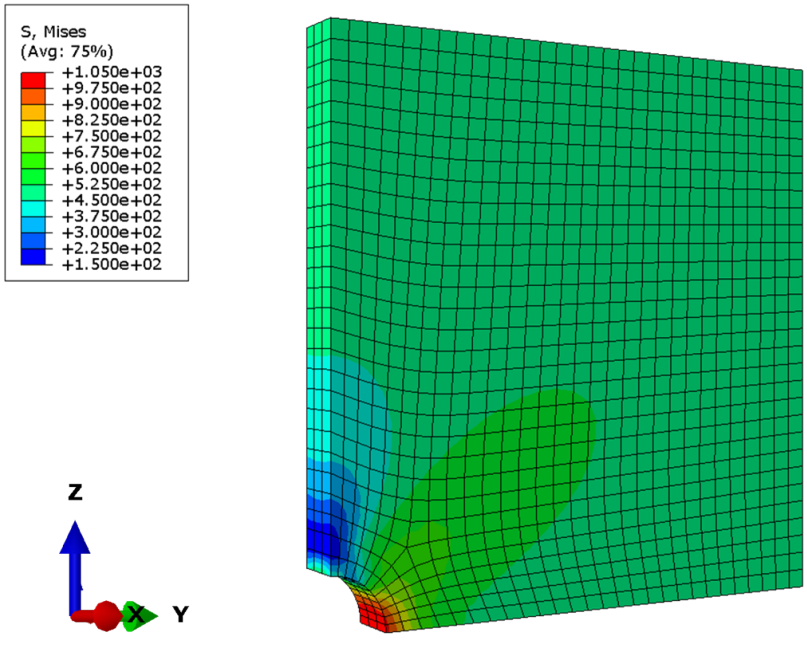

Figure 5.9: TIVP: Mises stress (MPa) after tensile loading to 0.51% nominal strain at 10^{-4} s^{-1}, 750°C

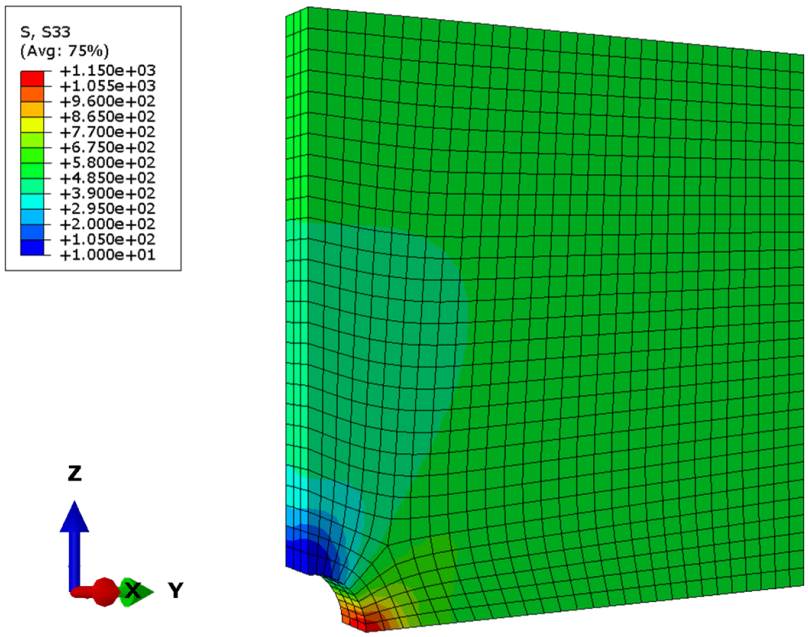

Figure 5.10: CVP (SX) Normal stress (MPa) in Z-direction after tensile loading to 0.51% nominal strain at 10^{-4} s^{-1}, 750°C

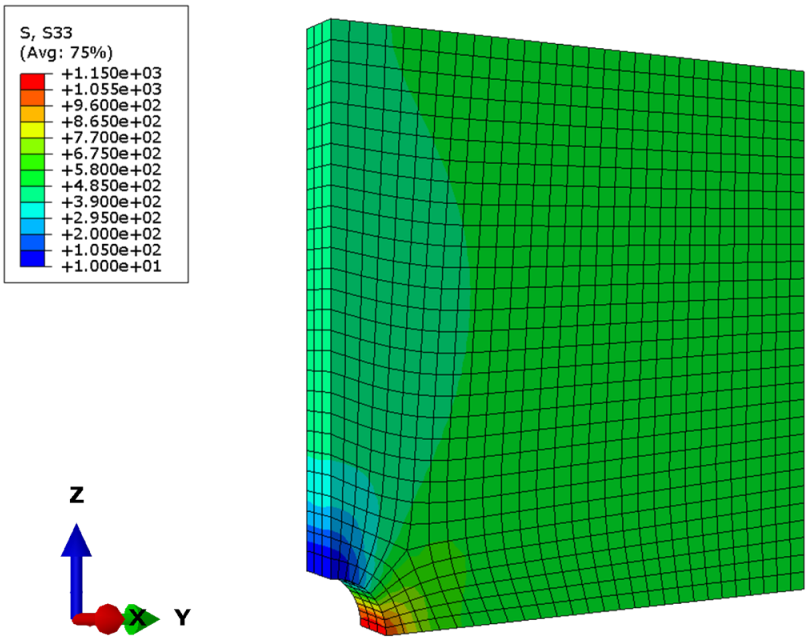

Figure 5.11: TIVP: Normal stress (MPa) in Z-direction after tensile loading to 0.51% nominal strain at 10^{-4} s^{-1}, 750°C

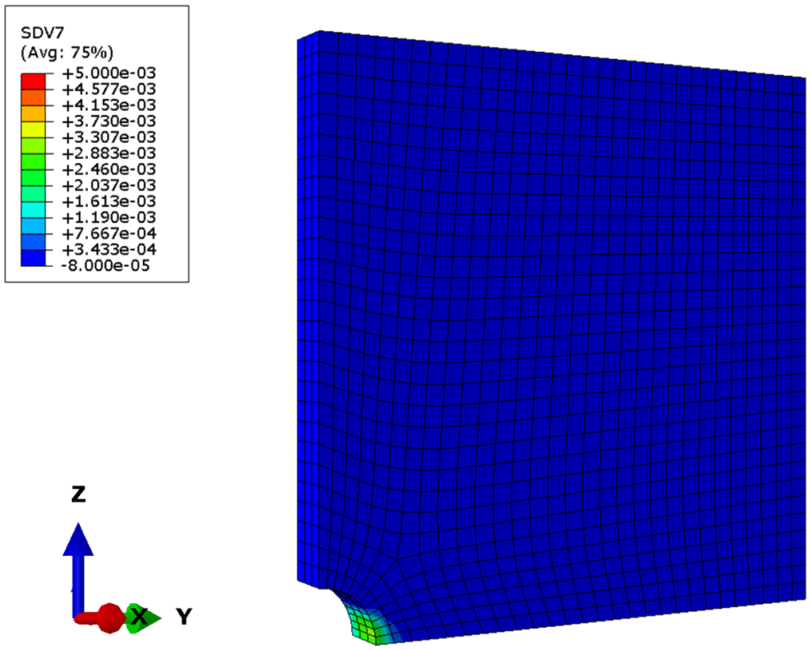

Figure 5.12: CVP (SX) Plastic strain in Z-direction after tensile loading to 0.51% nominal strain at 10^{-4} s^{-1}, 750°C

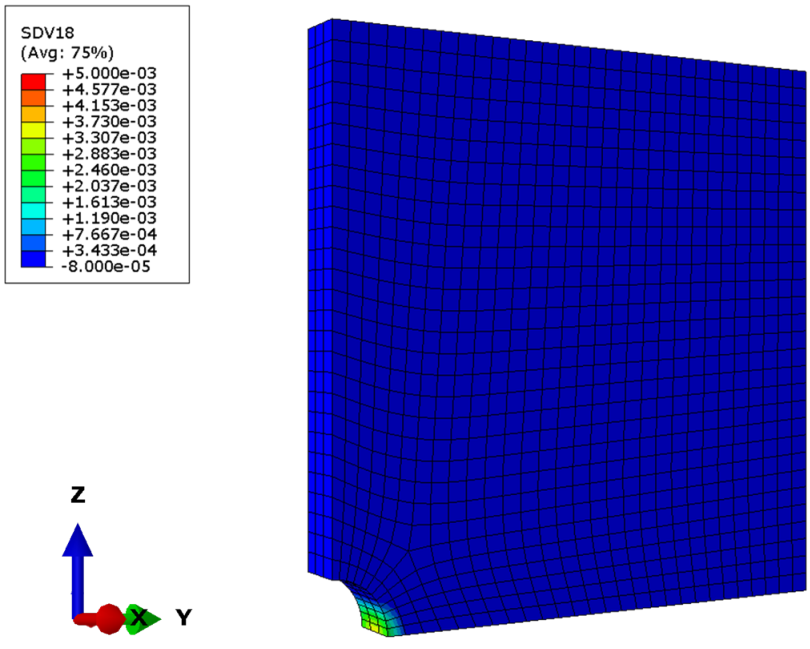

Figure 5.13: TIVP: Plastic strain in Z-direction after tensile loading to 0.51% nominal strain at 10^{-4} s^{-1}, 750°C

5.4 Local response comparison

In order to verify the approach of estimating local responses, the new ANN model was compared to the TIVP model to which it was trained at various element positions on the along the notch surface. A more refined mesh was used for this comparison to obtain reliable results. The ANN model prediction of the notch root response shows good agreement with the TIVP model, shown in Figures 5.15 for 950°C and Figure 5.16 for 750°C. To obtain these curves, a purely elastic analysis is conducted to the same nominal strain value, and the elastic stresses are used in a Neuber analysis. Additionally, other elements along the notch surface are compared. Figure 5.14 identifies elements along the notch surface evaluated in the analysis.

.

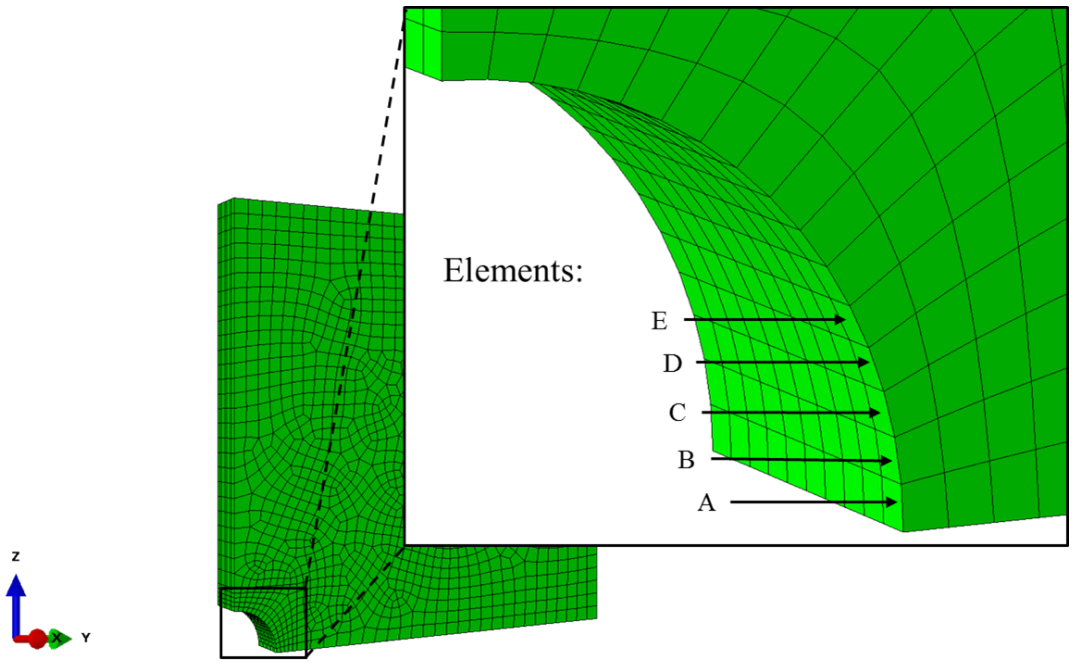

Figure 5.14: Nomenclature for notch surface elements

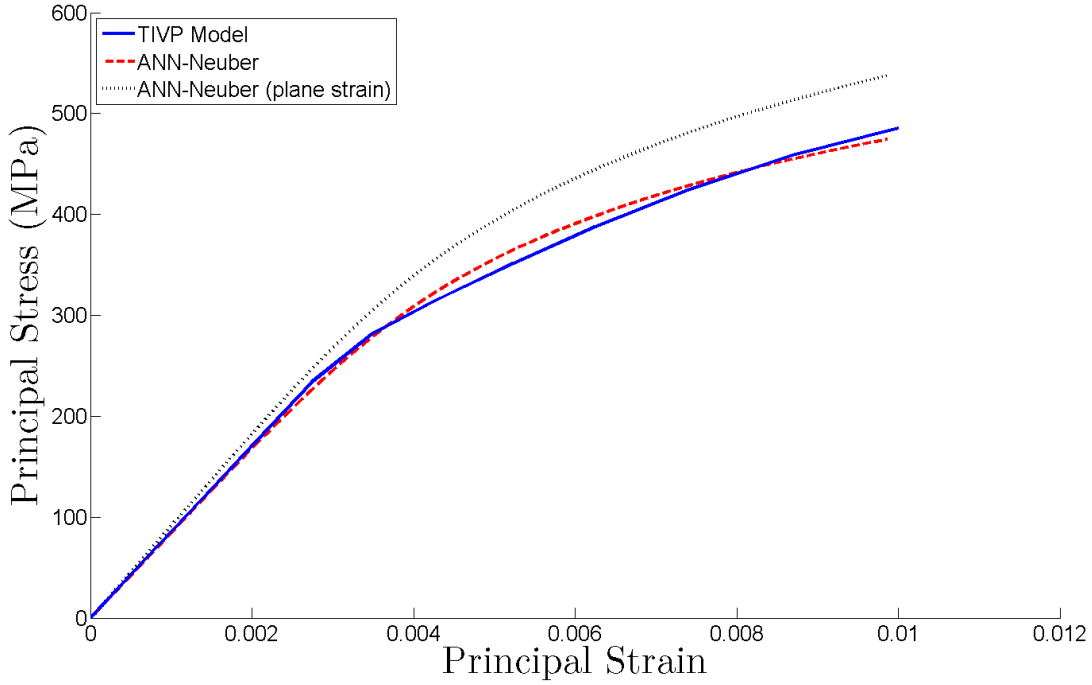

Figure 5.15: Comparison of notch root (Element A) reponses and ANN predictions, 950°C

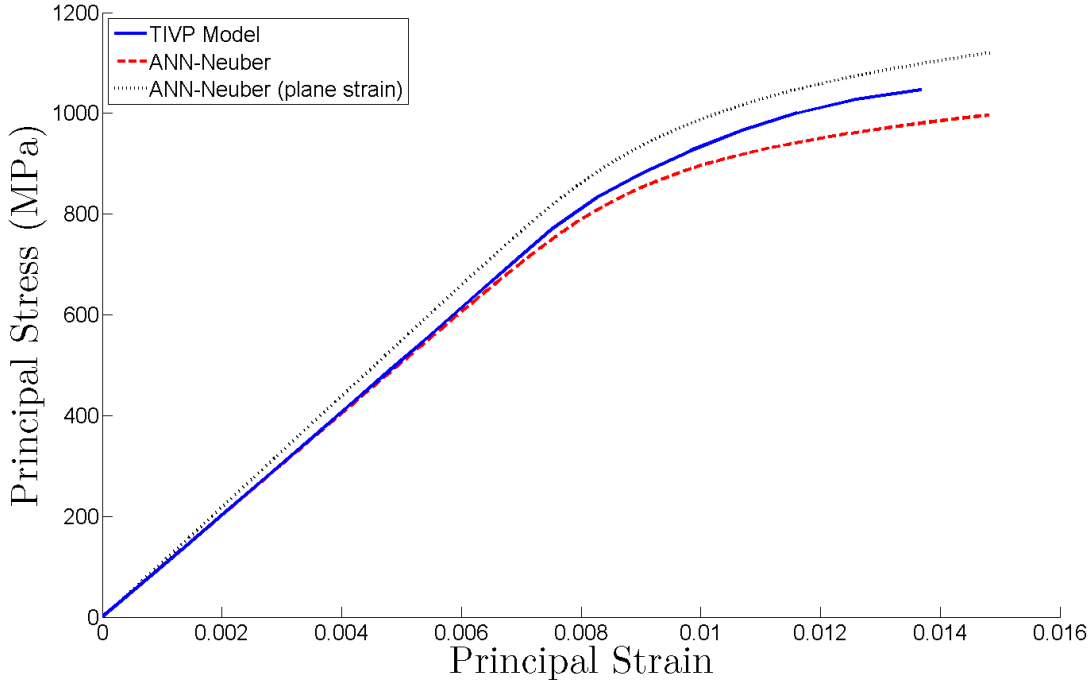

Figure 5.16: Comparison of notch root (Element A) reponses and ANN predictions, 750°C

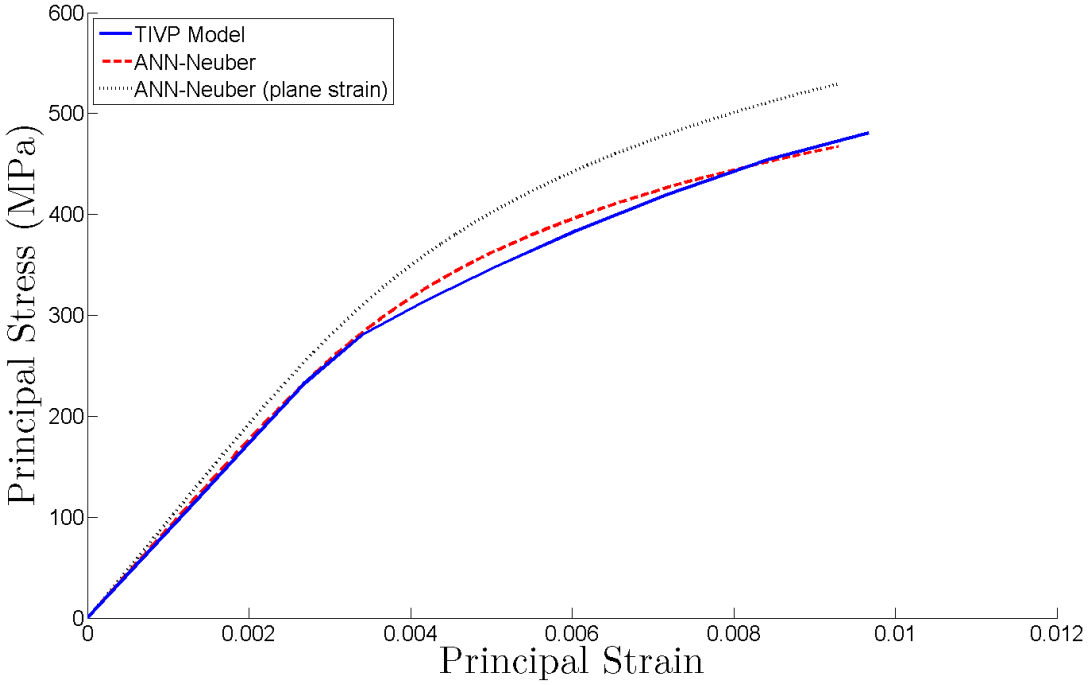

Figure 5.17: Comparison of Element B reponses and ANN predictions, 950°C

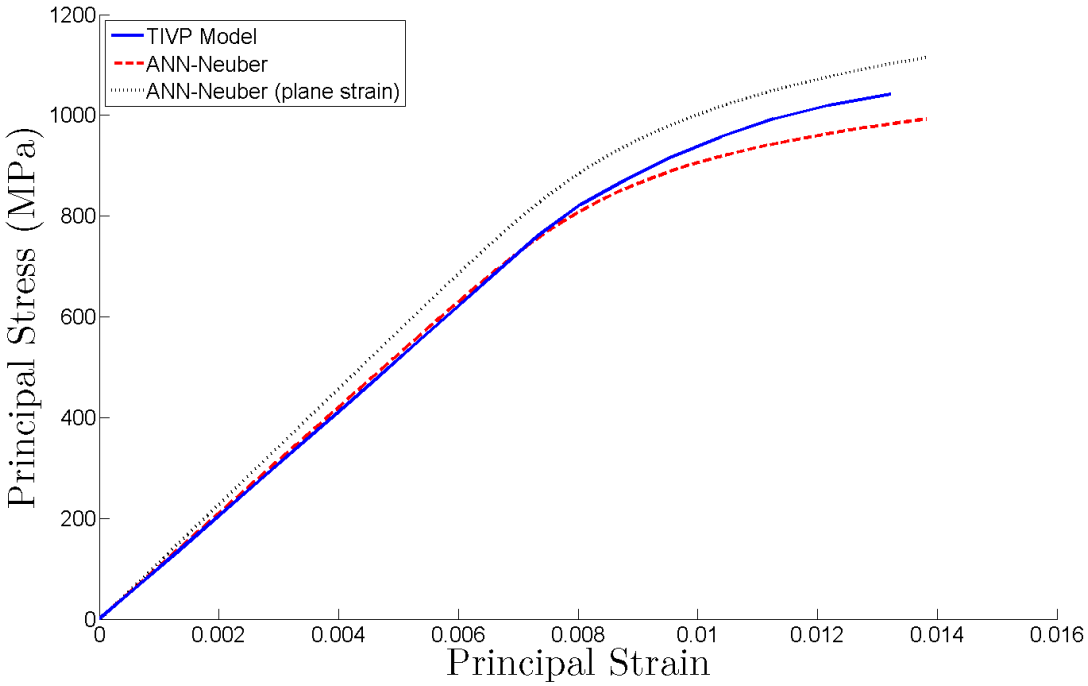

Figure 5.18: Comparison of Element B reponses and ANN predictions, 750°C

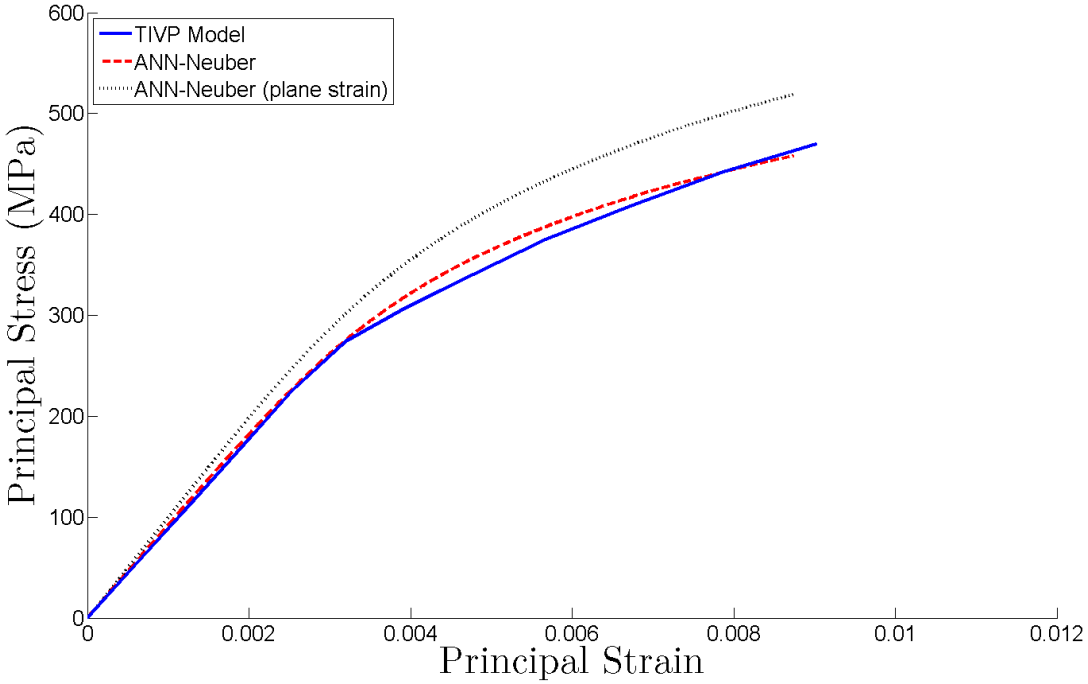

Figure 5.19: Comparison of Element C reponses and ANN predictions, 950°C

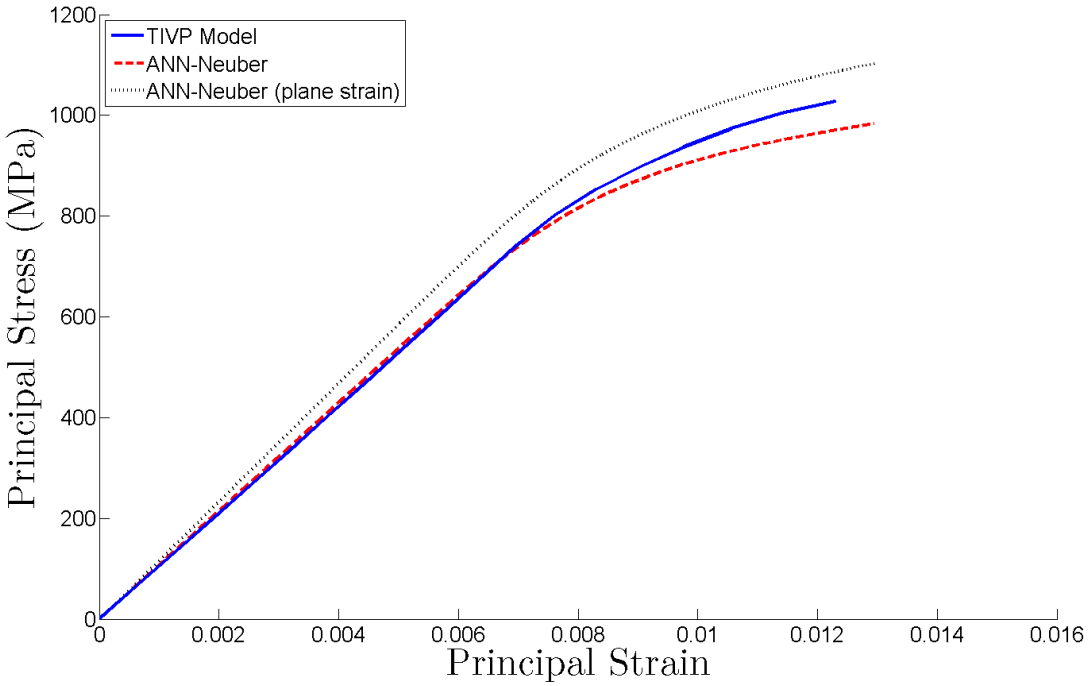

Figure 5.20: Comparison of Element C reponses and ANN predictions, 750°C

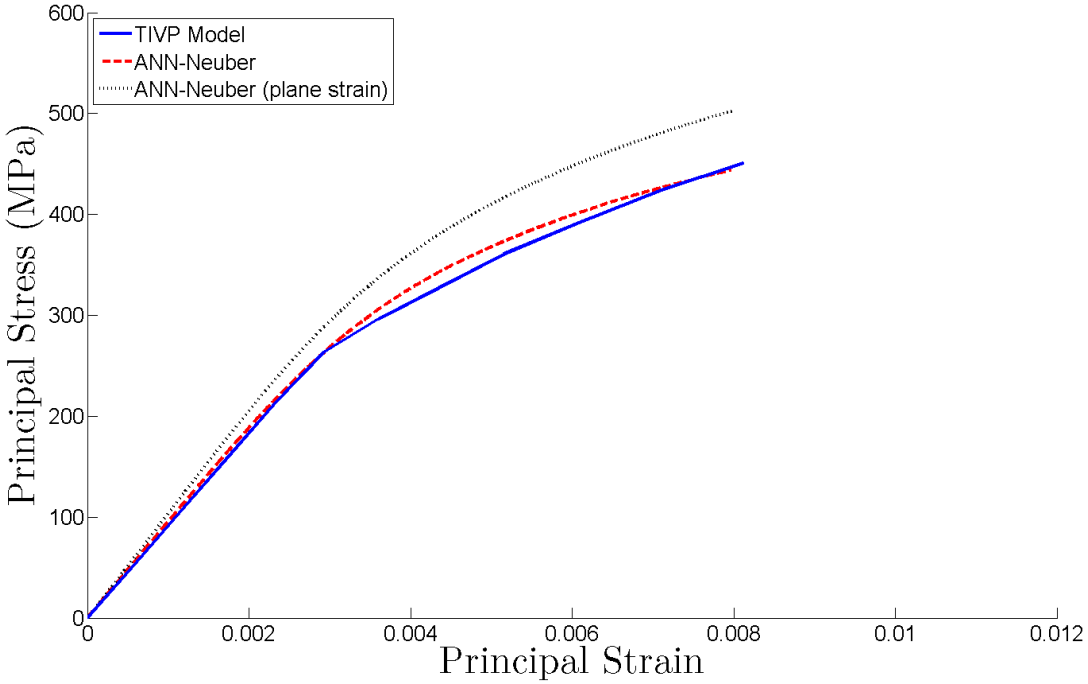

Figure 5.21: Comparison of Element D reponses and ANN predictions, 950°C

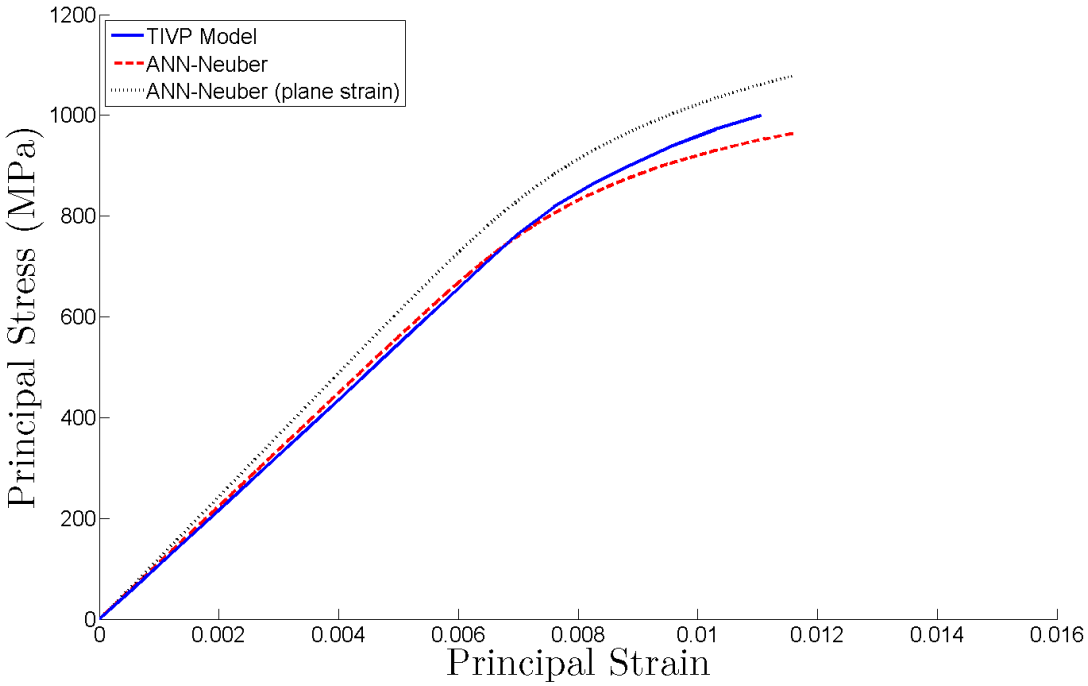

Figure 5.22: Comparison of Element D reponses and ANN predictions, 750°C

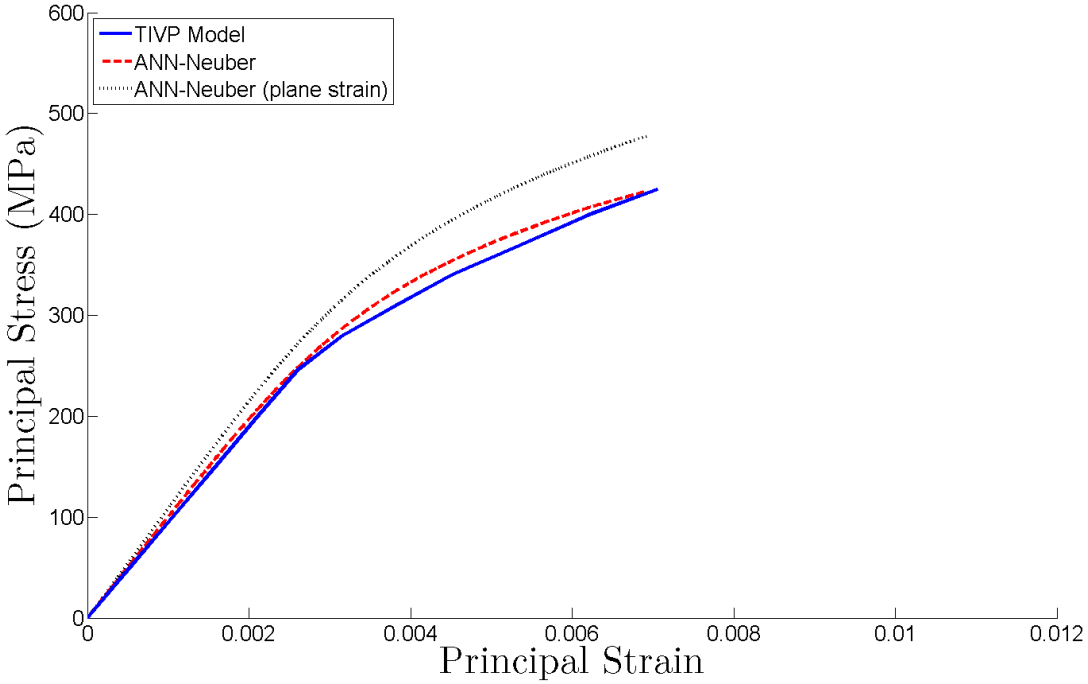

Figure 5.23: Comparison of Element E reponses and ANN predictions, 950°C

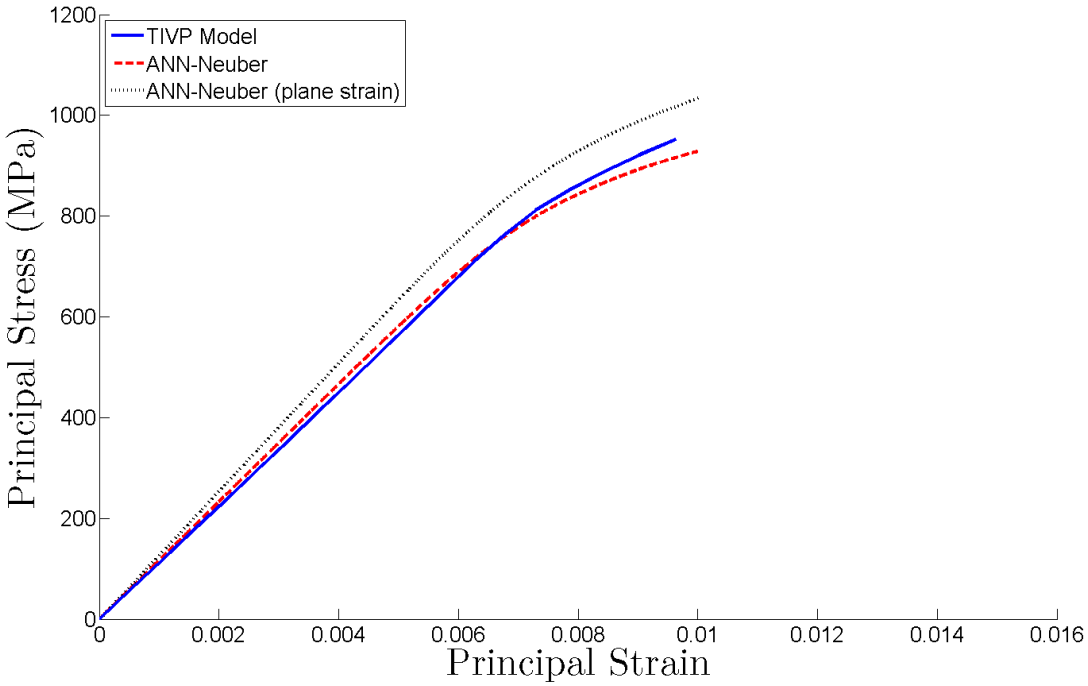

Figure 5.24: Comparison of Element E reponses and ANN predictions, 750°C

It is evident that there are noticeable, although small, differences between the ANN model and the TIVP model to which it was trained. These differences probably arise from error associated with the ability of the ANN to generalize the Ramberg-Osgood parameters for arbitrary off-axis orientations. The responses of the elements are best characterized by plane stress, which is expected with the elements on the thin plate model surface. Element responses under more complex states of stress will not be captured well by the ANN model, since it is trained using TIVP simulations under plane stress conditions. This is an additional limitation of the ANN model. However, while it is less accurate than the CVP and TIVP models, the ANN model is able to generate approximate stress-strain curves almost instantaneously, given the elastic stresses from a purely elastic FE simulation, and thus provides a drastic reduction in computational cost when compared to the CVP and TIVP models, as shown in Table 5.1.

CHAPTER VI

CONCLUSIONS

The results of this research are as follows:

1. **Calibrate a transversely isotropic viscoplasticity (TIVP) model to capture the response of a DS Ni-base superalloy for isothermal, thermomechanical, and creep conditions.**

    - The TIVP model, previously developed for a similar DS Ni-base superalloy, was calibrated to CM247LC-DS from 20-1050°C using isothermal uniaxial test data and simulations conducted with the CVP model.
    - The TIVP model, a unified creep-plasticity model implemented as a User MATerial subroutine (UMAT) for ABAQUS, is able to capture rate dependent stress-strain behavior under isothermal and thermomechanical conditions over the temperature range to which it was calibrated.
    - The TIVP model is also able to capture secondary creep behavior and stress relaxation at higher temperatures.

2. **Develop an extreme reduced order constitutive model to rapidly approximate DS Ni-base superalloy behavior under thermomechanical loading conditions.**

    - An artificial neural network (ANN) was trained using data generated by a CVP model in which temperature, strain rate, and material off-axis orientation were varied independently. The results were fitted to a simple 1-D Ramberg-Osgood relation, and the Ramberg-Osgood parameters and their corresponding temperatures, strain rates, and material orientations were then used to construct a training set for the ANN.

- Given inputs of temperature, strain rate, and material orientation from the DS axis, the trained ANN model is able to generate instantaneously Ramberg-Osgood parameters which capture material behavior at arbitrary temperatures, strain rates, and material orientations within the domain of the training set.
- The rapid first-order approximation produced by the ANN model shows good agreement with isothermal CVP predictions and experimental data, and is able to be extended to TMF in a limited manner, particularly using isothermal curves and effective Young's moduli to approximate the endpoints of stabilized hysteresis loops.

3. **Compare the reduced order and extreme reduced order constitutive models to the more complex crystal viscoplasticity (CVP) model in terms of relative accuracy and computational expense.**
   - The TIVP model shows excellent speed benefits, around an order of magnitude, when compared to the single crystal and multi-grain CVP models while still providing a high degree of accuracy.
   - The training process was repeated using the TIVP model to construct a new, different ANN model. The new ANN model provides a first-order approximation of material response almost instantaneously, given results from a purely elastic analysis.
   - While less accurate and not implemented as a user subroutine for finite element codes, the ANN modeling technique shows promise in certain phases of design where approximations of local responses at stress concentrators are desired and speed is of primary importance rather than accuracy.

CHAPTER VII

RECOMMENDATIONS

There are several steps that could be taken to extend this research and to improve the reduced order modeling techniques described in this work. The following recommendations are presented.

Microstructure sensitivity

Although quantification of microstructure is not a trivial task, it is possible that some sort of aspect ratio describing precipitate morphology could be used to characterize the microstructure at a given state. The addition of microstructure sensitivity to the TIVP and ANN models would be a natural extension of this work. This would perhaps require the need of a microstructure-sensitive CVP model to account for microstructure evolution with the effects of time, temperature, and stress. The advanced CVP model could then be used to calibrate a lower level TIVP model, and additional internal state variables could be defined in the TIVP model to reflect the evolution of model parameters. In addition, the microstructure-sensitive CVP model could be used to construct a new training set for an ANN that would further take into account microstructure evolution through adding microstructural parameters as inputs.

Improved ANN Training

One benefit of artificial neural networks is the ability to generalize well even with limited training data. Reducing the training set for the ANN would allow new training sets to be comstructed more rapidly, which would be beneficial when the model used to train the ANN is updated (i.e. a newer version of the CVP is released). Also, a more optimal ANN architecture could be determined, which may reduce memory and time required for training and increase performance. Many other variations in training could be explored, including other training functions or techniques to improve generalization such as early stopping.

Damage Model

A damage model could be incorporated into the TIVP model in order to capture tertiary creep. This would result in better creep characterization and improved creep predictions at longer durations, which could be useful in predicting creep behavior of a blade component after an extended period of service, although the useful life of the component may have been exhausted at this point. A fully 3-D anisotropic damage model was implemented during previous work on a similar DS Ni-base superalloy [41] and captured tertiary creep response reasonably well at various temperatures and stress levels.

APPENDIX A

TIVP CALIBRATION CURVES

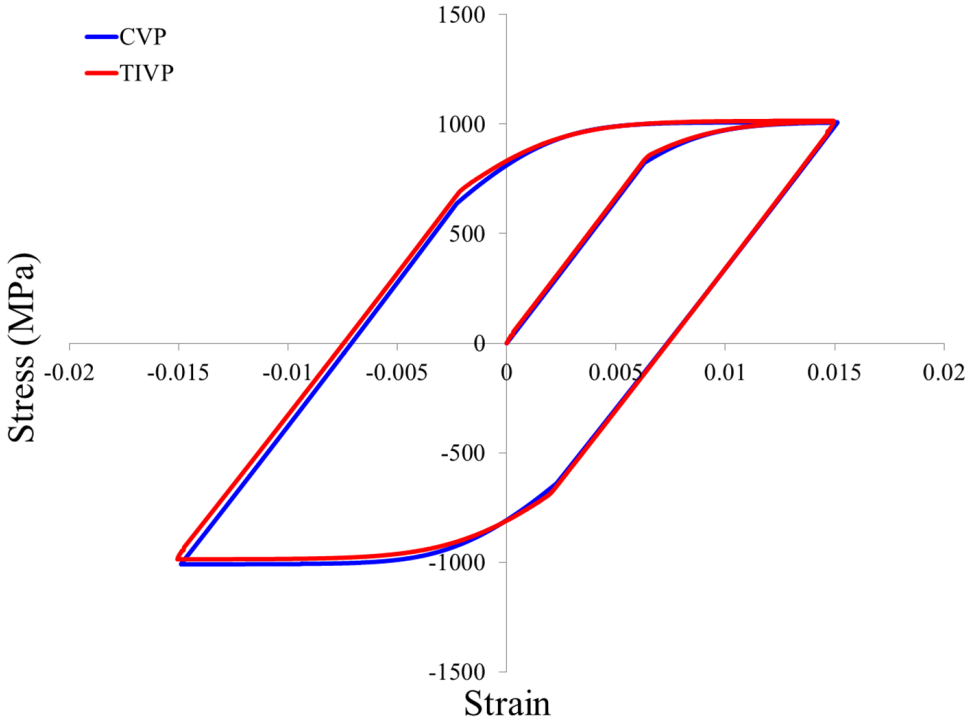

Figure A.1: TIVP model calibration curve for 20°C, longitudinal orientation

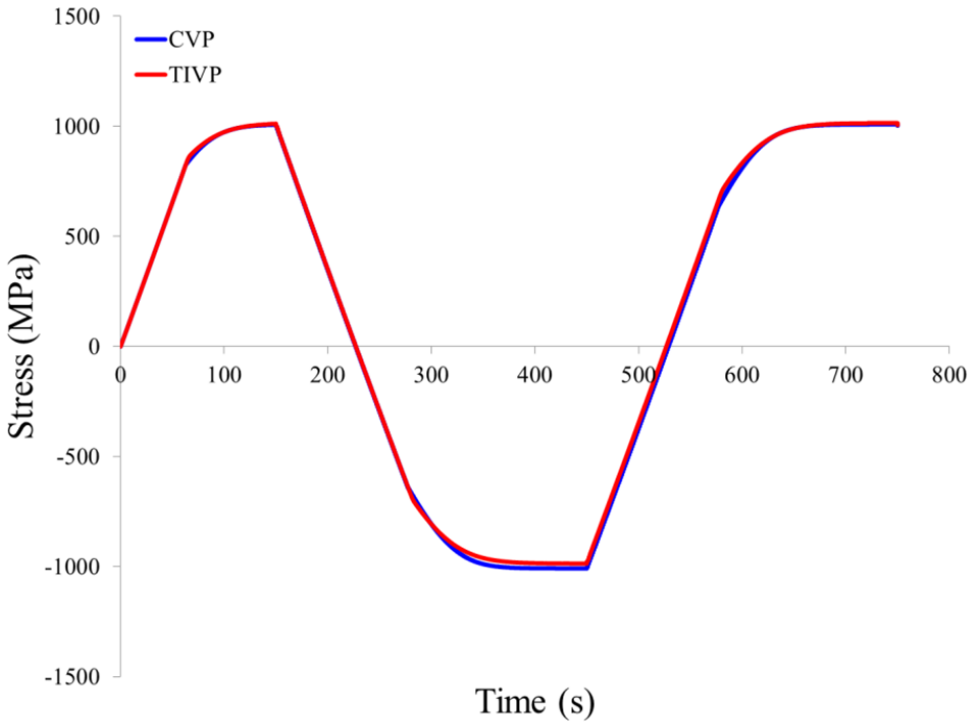

Figure A.2: TIVP model calibration curve for 20°C, longitudinal orientation

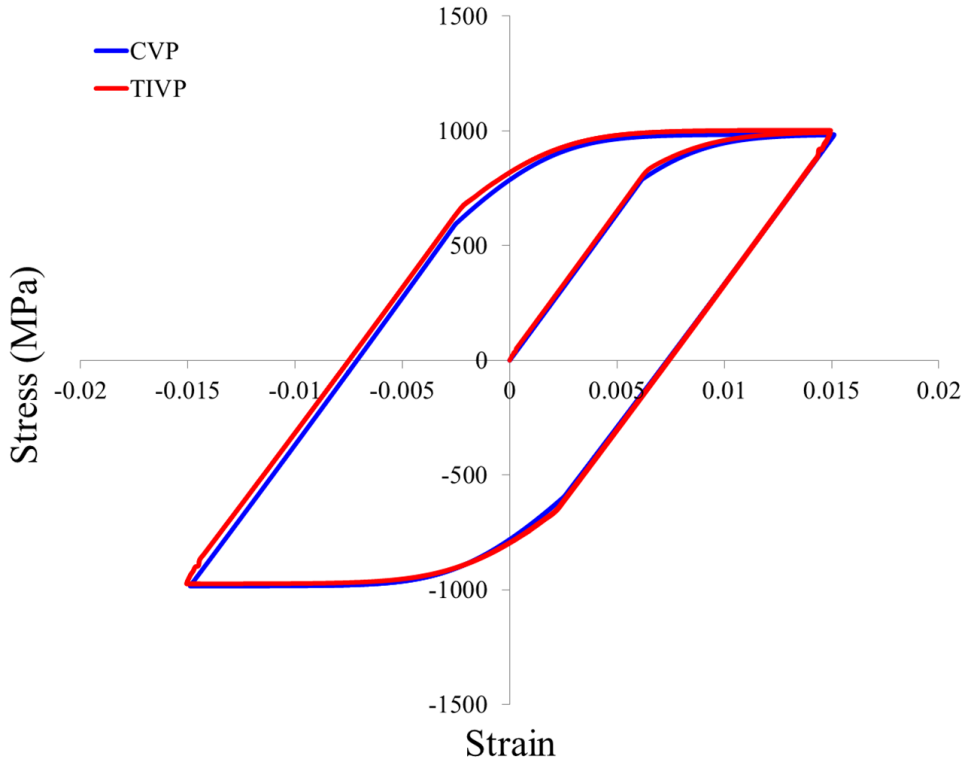

Figure A.3: TIVP model calibration curve for 150°C, longitudinal orientation

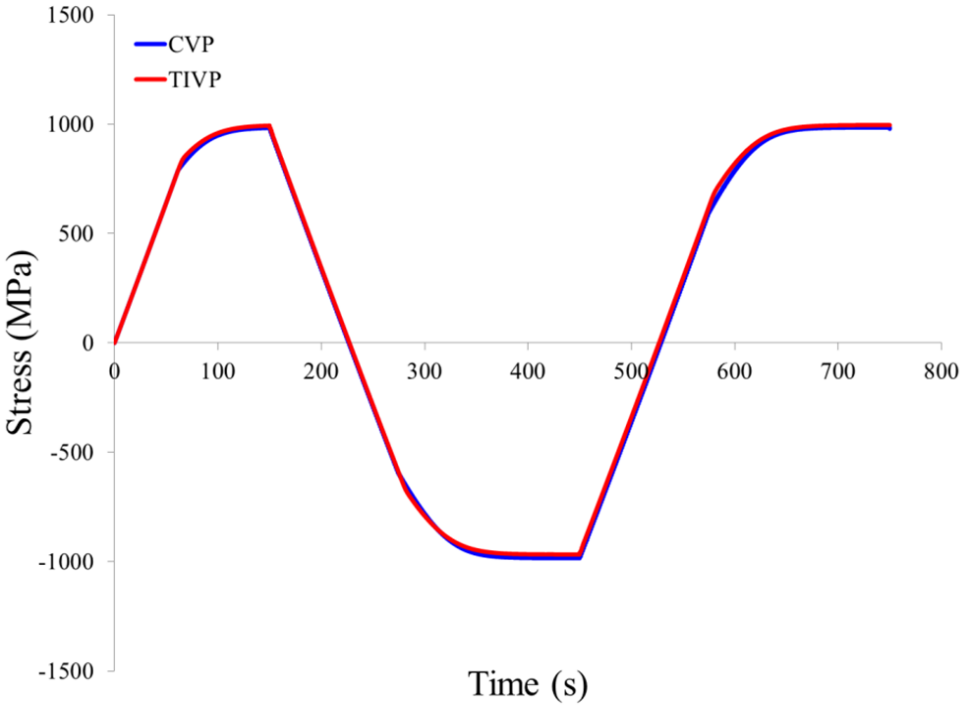

Figure A.4: TIVP model calibration curve for 150°C, longitudinal orientation

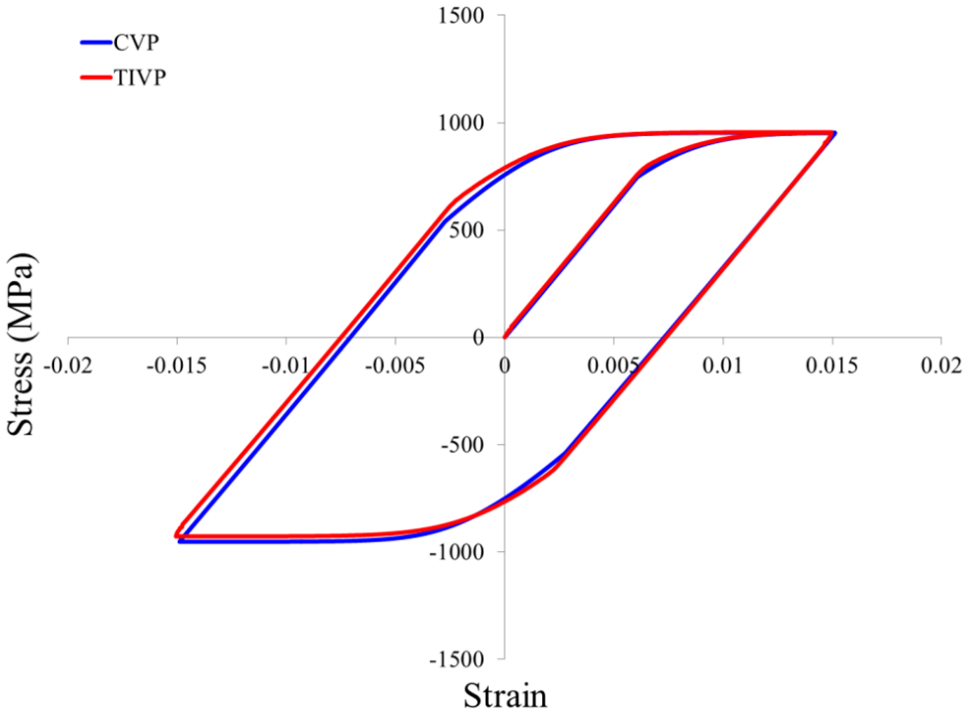

Figure A.5: TIVP model calibration curve for 300°C, longitudinal orientation

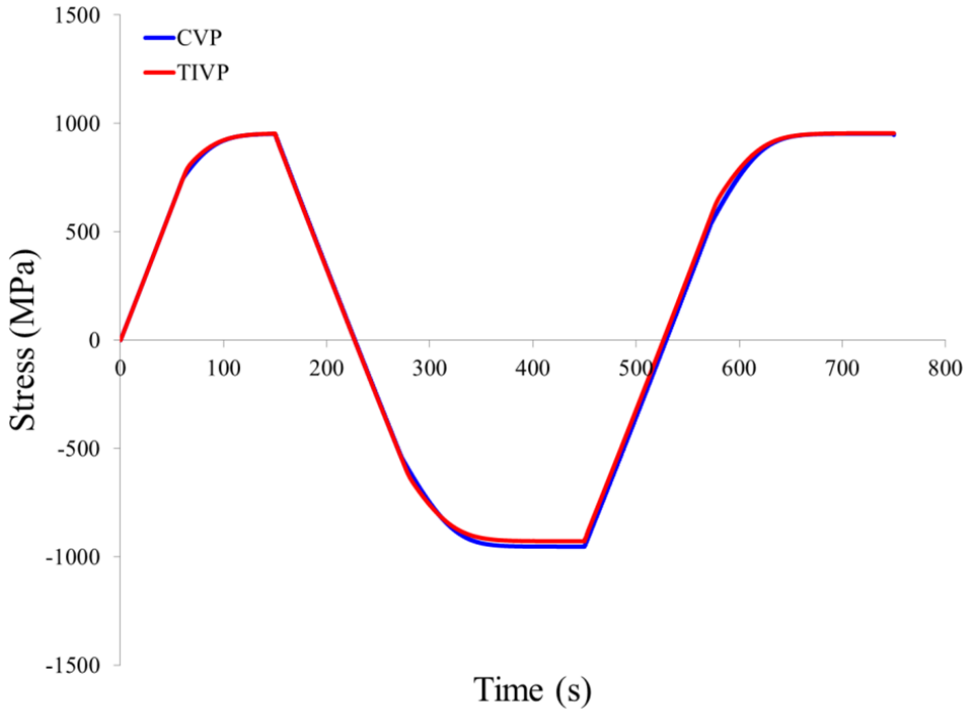

Figure A.6: TIVP model calibration curve for 300°C, longitudinal orientation

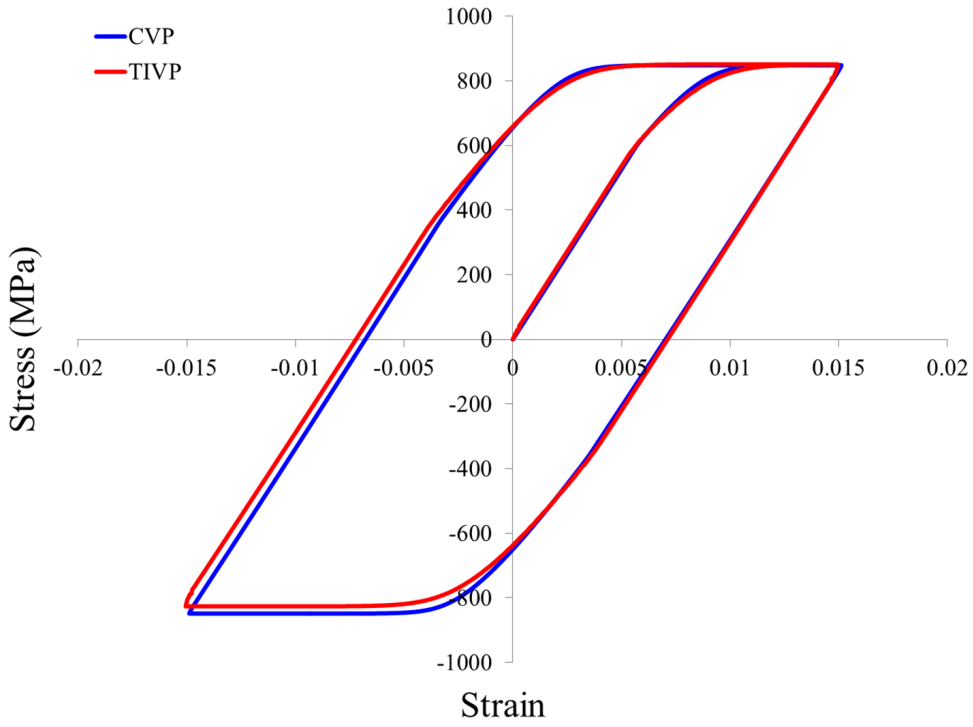

Figure A.7: TIVP model calibration curve for 650°C, longitudinal orientation

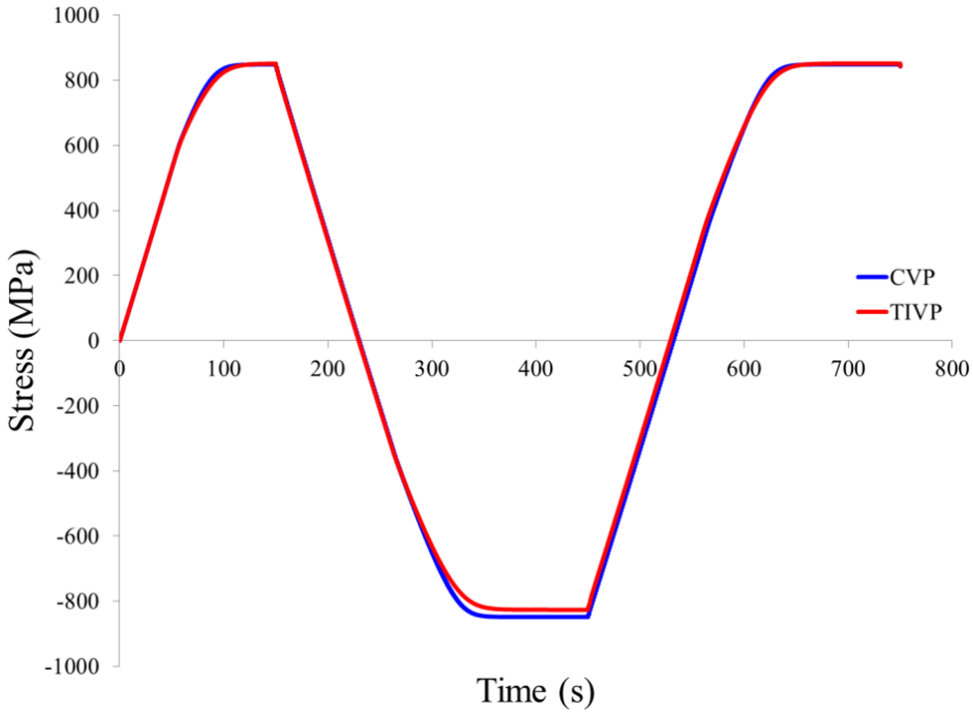

Figure A.8: TIVP model calibration curve for 650°C, longitudinal orientation

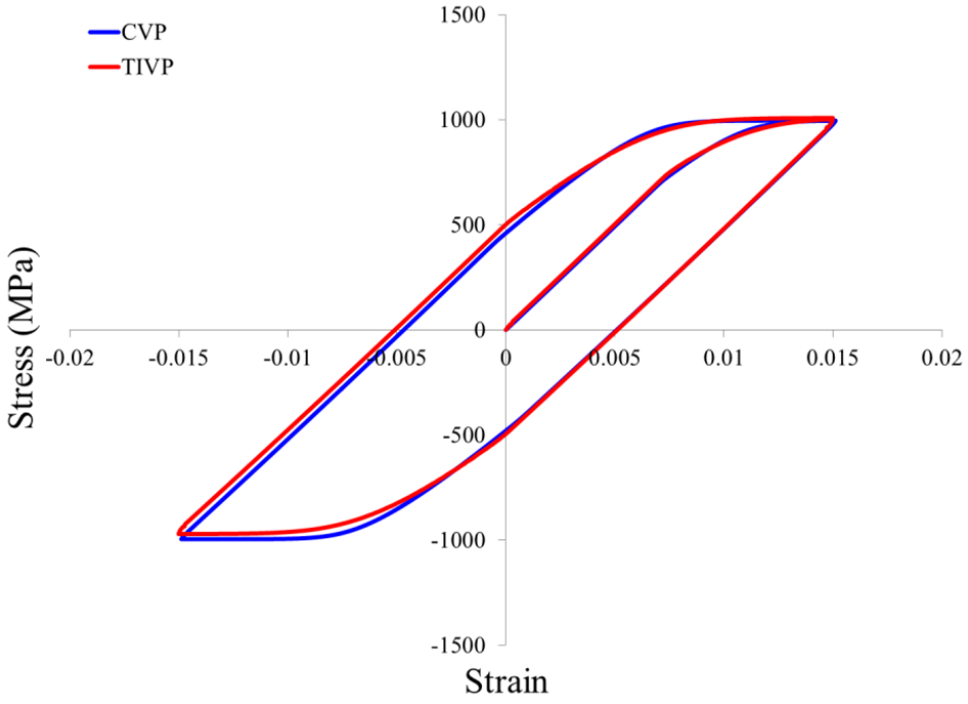

Figure A.9: TIVP model calibration curve for 750°C, longitudinal orientation

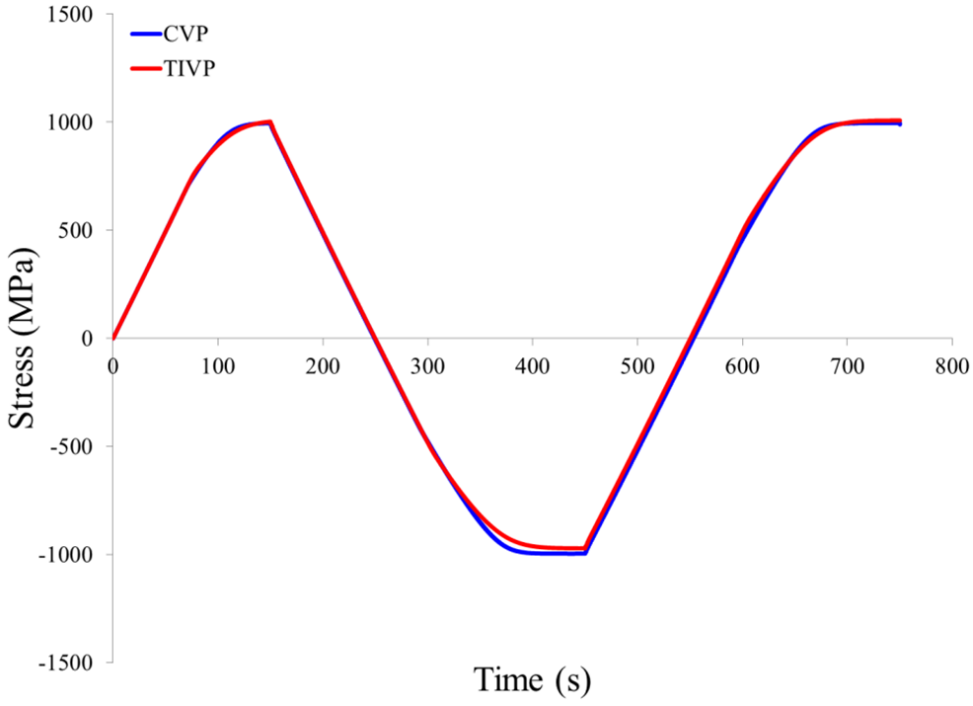

Figure A.10: TIVP model calibration curve for 750°C, longitudinal orientation

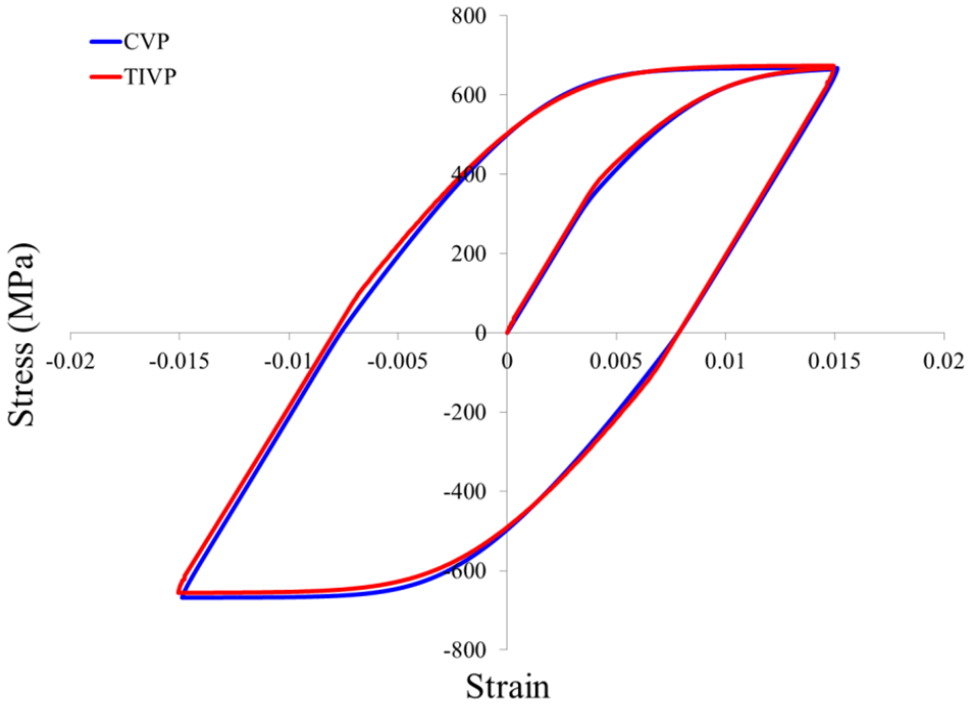

Figure A.11: TIVP model calibration curve for 850°C, longitudinal orientation

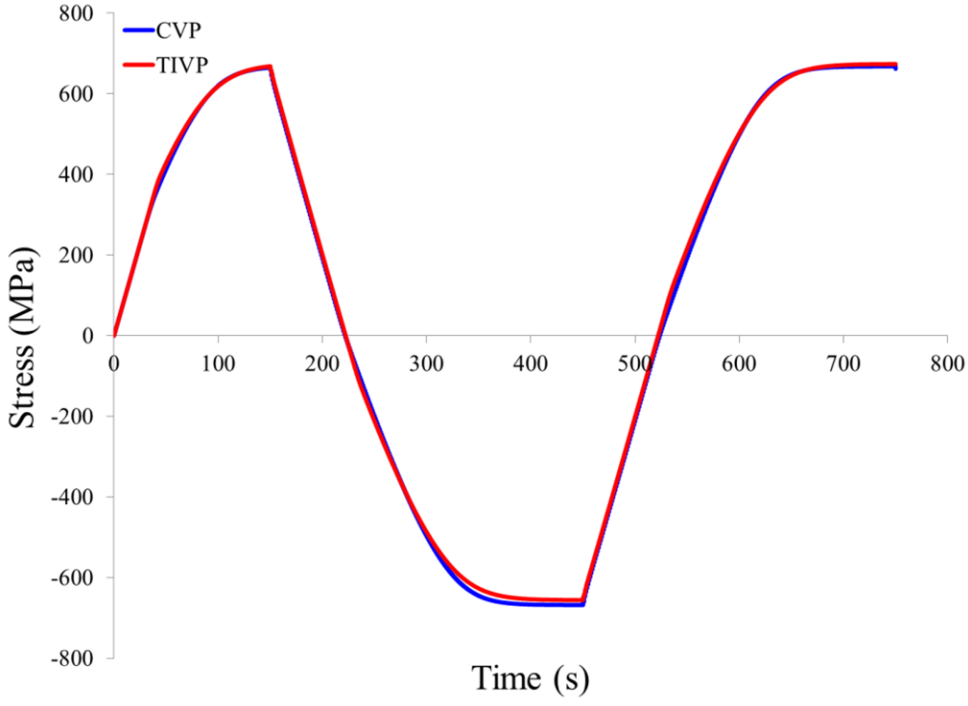

Figure A.12: TIVP model calibration curve for 850°C, longitudinal orientation

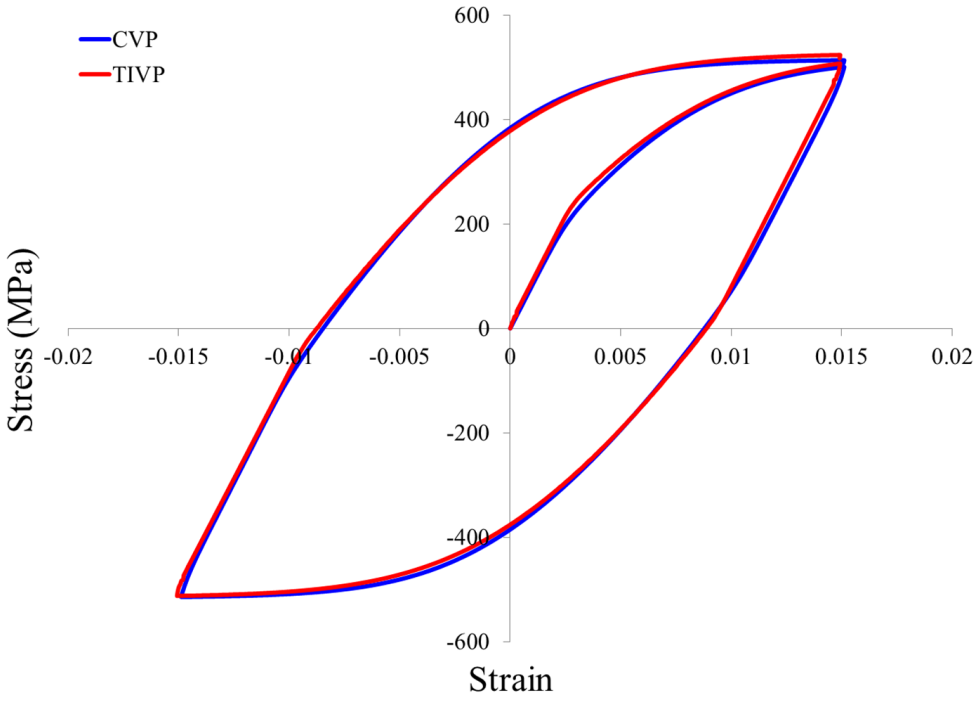

Figure A.13: TIVP model calibration curve for 950°C, longitudinal orientation

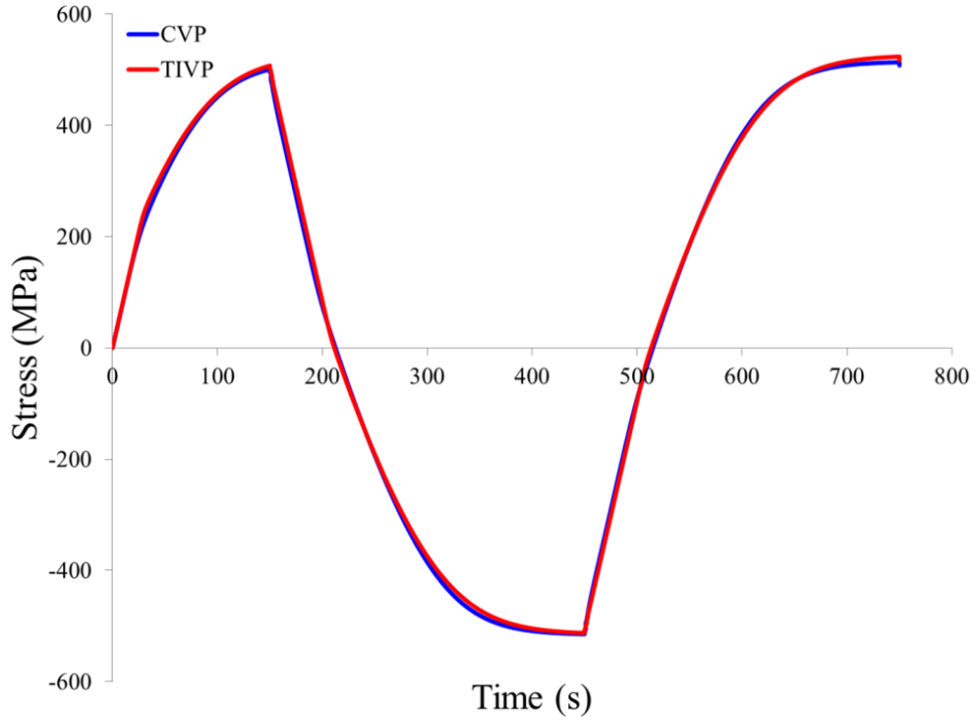

Figure A.14: TIVP model calibration curve for 950°C, longitudinal orientation

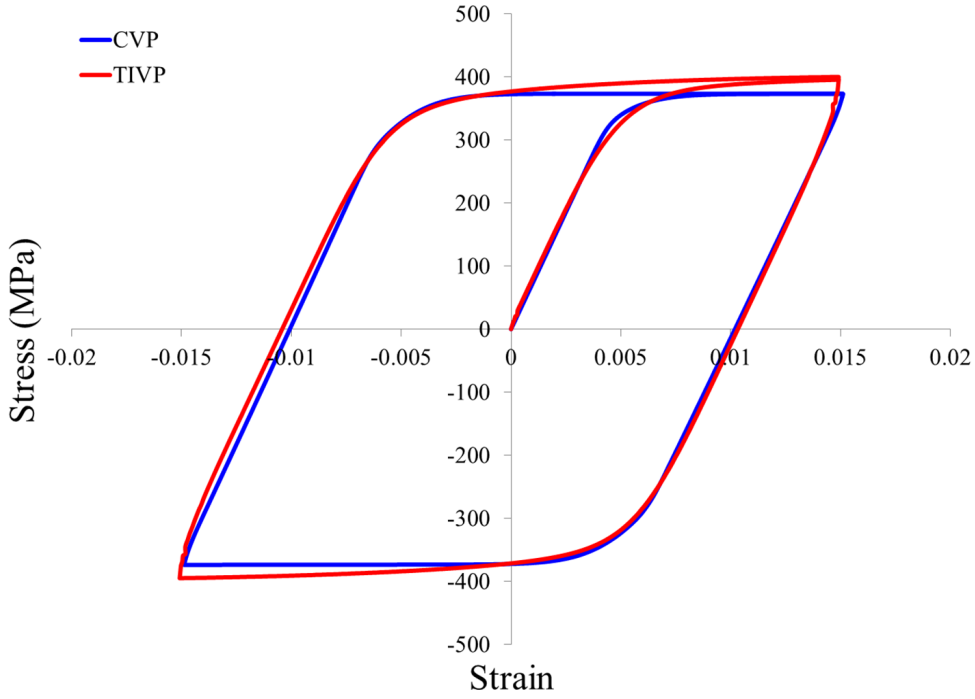

Figure A.15: TIVP model calibration curve for 1050°C, longitudinal orientation

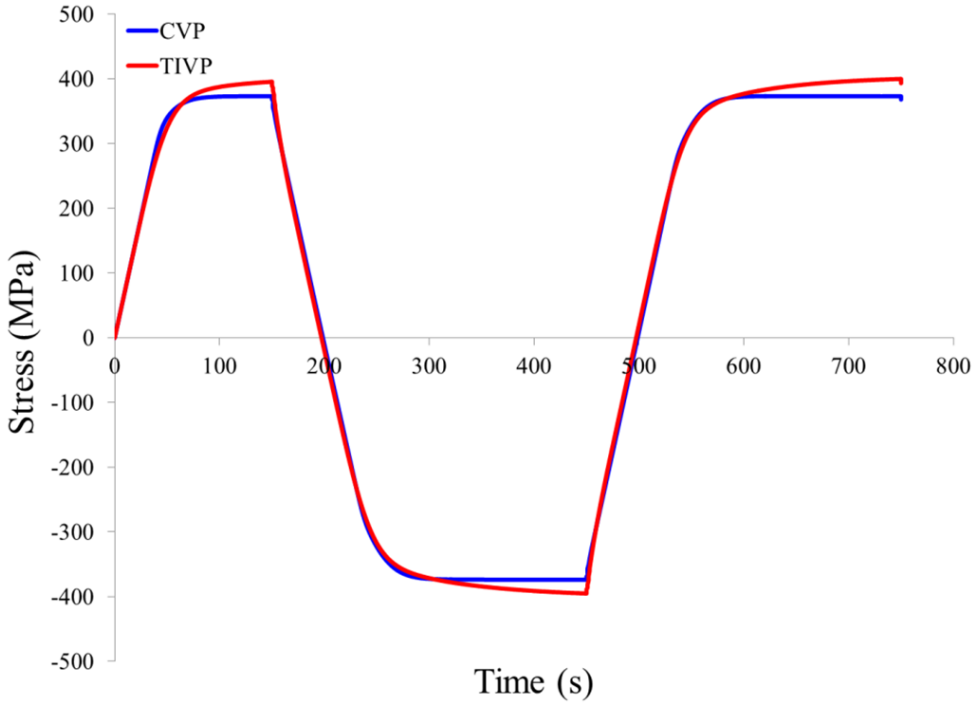

Figure A.16: TIVP model calibration curve for 1050°C, longitudinal orientation

APPENDIX B

ANN TRAINING DATA FROM TIVP

Temperature (°C)	**Log($\dot{\epsilon}$)**	**θ(°)**	***E* (MPa)**	***K* (MPa)**	***n* (unitless)**
20	-3	0	130537	1241.87	0.0394
20	-3	5	133429	1263.22	0.0426
20	-3	10	141951	1353.27	0.0549
20	-3	15	155500	1446.22	0.0676
20	-3	20	173484	1499.07	0.0753
20	-3	25	194642	1508.77	0.0778
20	-3	30	217270	1463.72	0.0738
20	-3	35	239017	1403.29	0.0677
20	-3	40	257269	1360.43	0.0636
20	-3	45	269520	1342.60	0.0629
20	-3	50	273922	1302.28	0.0597
20	-3	55	269971	1278.71	0.0589
20	-3	60	258541	1261.65	0.0589
20	-3	65	241980	1240.29	0.0583
20	-3	70	223217	1228.90	0.0589
20	-3	75	205382	1202.57	0.0569
20	-3	80	190955	1182.63	0.0552
20	-3	85	181591	1165.61	0.0534
20	-3	90	178329	1156.46	0.0523
150	-3	0	127417	1256.13	0.0422
150	-3	5	130431	1265.36	0.0440
150	-3	10	138616	1356.03	0.0562
150	-3	15	151824	1460.74	0.0701
150	-3	20	169357	1508.31	0.0773
150	-3	25	189936	1510.47	0.0789
150	-3	30	211841	1471.12	0.0755

Temperature (°C)	**Log($\dot{\epsilon}$)**	**θ(°)**	***E* (MPa)**	***K* (MPa)**	***n* (unitless)**
150	-3	35	232859	1406.37	0.0689
150	-3	40	250488	1352.97	0.0634
150	-3	45	262249	1325.81	0.0615
150	-3	50	266397	1307.93	0.0611
150	-3	55	262467	1283.48	0.0601
150	-3	60	251255	1264.84	0.0600
150	-3	65	235076	1241.31	0.0593
150	-3	70	216907	1226.18	0.0594
150	-3	75	199573	1202.09	0.0577
150	-3	80	185537	1177.28	0.0554
150	-3	85	176478	1165.89	0.0544
150	-3	90	173323	1156.37	0.0533
300	-3	0	122701	1252.54	0.0463
300	-3	5	125411	1270.88	0.0491
300	-3	10	133337	1331.03	0.0578
300	-3	15	146022	1434.83	0.0716
300	-3	20	162840	1491.71	0.0798
300	-3	25	182590	1494.44	0.0815
300	-3	30	203570	1443.34	0.0767
300	-3	35	223680	1391.95	0.0715
300	-3	40	240453	1346.24	0.0670
300	-3	45	251594	1320.47	0.0652
300	-3	50	255387	1289.10	0.0630
300	-3	55	251434	1264.09	0.0619
300	-3	60	240612	1247.69	0.0621
300	-3	65	225033	1228.50	0.0619
300	-3	70	207564	1203.78	0.0607
300	-3	75	190896	1184.06	0.0596
300	-3	80	177455	1168.81	0.0586
300	-3	85	168750	1155.66	0.0574
300	-3	90	165760	1146.88	0.0564

Temperature (°C)	**Log($\dot{\epsilon}$)**	**θ(°)**	**E (MPa)**	**K (MPa)**	**n (unitless)**
450	-3	0	116280	1309.66	0.0686
450	-3	5	118843	1322.04	0.0707
450	-3	10	126327	1370.66	0.0777
450	-3	15	138449	1458.01	0.0893
450	-3	20	154418	1515.99	0.0972
450	-3	25	173235	1515.18	0.0982
450	-3	30	193143	1481.92	0.0951
450	-3	35	211393	1424.65	0.0890
450	-3	40	224039	1370.70	0.0829
450	-3	45	231615	1325.89	0.0782
450	-3	50	234268	1297.09	0.0762
450	-3	55	226419	1257.35	0.0727
450	-3	60	219932	1249.81	0.0744
450	-3	65	211397	1264.60	0.0795
450	-3	70	196083	1247.78	0.0795
450	-3	75	180286	1223.41	0.0779
450	-3	80	167431	1207.91	0.0769
450	-3	85	159175	1187.35	0.0747
450	-3	90	156364	1186.95	0.0748
600	-3	0	108209	1453.69	0.0863
600	-3	5	110662	1473.09	0.0890
600	-3	10	117740	1513.08	0.0948
600	-3	15	129154	1596.55	0.1050
600	-3	20	144186	1647.26	0.1115
600	-3	25	161862	1650.66	0.1128
600	-3	30	180473	1617.87	0.1098
600	-3	35	197207	1546.59	0.1023
600	-3	40	208940	1466.46	0.0935
600	-3	45	216334	1418.94	0.0886
600	-3	50	218360	1381.20	0.0855
600	-3	55	212623	1346.53	0.0830

Temperature (°C)	**Log($\dot{\epsilon}$)**	**θ(°)**	**E (MPa)**	**K (MPa)**	**n (unitless)**
600	-3	60	205907	1348.67	0.0859
600	-3	65	196841	1370.84	0.0917
600	-3	70	182612	1371.63	0.0941
600	-3	75	167751	1348.76	0.0929
600	-3	80	155631	1330.06	0.0915
600	-3	85	147848	1314.63	0.0901
600	-3	90	145119	1304.83	0.0890
750	-3	0	98562	1309.64	0.0503
750	-3	5	100874	1347.72	0.0549
750	-3	10	107478	1467.27	0.0683
750	-3	15	118067	1642.44	0.0864
750	-3	20	132079	1762.20	0.0985
750	-3	25	148482	1810.98	0.1032
750	-3	30	165920	1795.43	0.1018
750	-3	35	182561	1731.81	0.0956
750	-3	40	196432	1679.11	0.0905
750	-3	45	205515	1637.62	0.0869
750	-3	50	208401	1619.24	0.0861
750	-3	55	204784	1609.98	0.0867
750	-3	60	195441	1596.28	0.0872
750	-3	65	182216	1586.29	0.0881
750	-3	70	167465	1567.08	0.0877
750	-3	75	153435	1540.11	0.0860
750	-3	80	142102	1511.79	0.0836
750	-3	85	134825	1494.93	0.0819
750	-3	90	132354	1487.31	0.0811
900	-3	0	86954	1306.42	0.1520
900	-3	5	88977	1307.35	0.1526
900	-3	10	94968	1366.63	0.1609
900	-3	15	104628	1407.63	0.1669
900	-3	20	117379	1453.78	0.1728

Temperature (°C)	**Log($\dot{\epsilon}$)**	**θ(°)**	**E (MPa)**	**K (MPa)**	**n (unitless)**
900	-3	25	132345	1459.36	0.1732
900	-3	30	148277	1445.24	0.1708
900	-3	35	163553	1429.52	0.1680
900	-3	40	176236	1415.10	0.1654
900	-3	45	184580	1414.31	0.1649
900	-3	50	187290	1395.96	0.1627
900	-3	55	183936	1409.10	0.1648
900	-3	60	175289	1399.42	0.1644
900	-3	65	163128	1416.71	0.1673
900	-3	70	149561	1401.38	0.1661
900	-3	75	136696	1407.59	0.1670
900	-3	80	126308	1378.18	0.1633
900	-3	85	119622	1379.39	0.1630
900	-3	90	117320	1364.30	0.1610
1050	-3	0	74323	1429.66	0.1333
1050	-3	5	76110	1420.31	0.1331
1050	-3	10	81271	1389.55	0.1315
1050	-3	15	89312	1326.37	0.1255
1050	-3	20	99561	1244.48	0.1154
1050	-3	25	110760	1133.57	0.0988
1050	-3	30	121864	1027.90	0.0806
1050	-3	35	131740	937.39	0.0631
1050	-3	40	139519	872.27	0.0494
1050	-3	45	144403	834.29	0.0410
1050	-3	50	145927	821.87	0.0383
1050	-3	55	144055	832.96	0.0411
1050	-3	60	139290	866.35	0.0488
1050	-3	65	132323	920.39	0.0603
1050	-3	70	123894	989.62	0.0737
1050	-3	75	115461	1073.85	0.0881
1050	-3	80	107584	1135.35	0.0973

Temperature (°C)	**Log($\dot{\epsilon}$)**	**θ(°)**	**E (MPa)**	**K (MPa)**	**n (unitless)**
1050	-3	85	102122	1170.17	0.1018
1050	-3	90	100212	1184.16	0.1035
20	-4	0	129963	1232.65	0.0405
20	-4	5	132721	1245.21	0.0426
20	-4	10	141142	1322.12	0.0535
20	-4	15	154689	1421.58	0.0671
20	-4	20	172609	1480.65	0.0756
20	-4	25	193632	1474.66	0.0764
20	-4	30	216110	1442.86	0.0738
20	-4	35	237757	1380.22	0.0673
20	-4	40	256750	1351.73	0.0646
20	-4	45	268284	1323.86	0.0630
20	-4	50	272704	1282.83	0.0596
20	-4	55	268722	1261.02	0.0588
20	-4	60	257294	1233.01	0.0572
20	-4	65	240748	1230.39	0.0594
20	-4	70	222098	1189.71	0.0558
20	-4	75	204359	1182.77	0.0566
20	-4	80	189924	1163.83	0.0549
20	-4	85	180612	1147.67	0.0532
20	-4	90	177436	1139.46	0.0522
150	-4	0	126984	1234.52	0.0431
150	-4	5	129749	1247.21	0.0453
150	-4	10	137903	1321.25	0.0558
150	-4	15	151074	1414.85	0.0687
150	-4	20	168413	1465.77	0.0763
150	-4	25	188874	1467.59	0.0779
150	-4	30	210719	1433.06	0.0749
150	-4	35	231692	1374.72	0.0688
150	-4	40	249284	1327.88	0.0641
150	-4	45	261085	1307.40	0.0630

Temperature (°C)	**Log($\dot{\epsilon}$)**	$\boldsymbol{\theta}(^\circ)$	$\boldsymbol{E}$ **(MPa)**	$\boldsymbol{K}$ **(MPa)**	$\boldsymbol{n}$ **(unitless)**
150	-4	50	265211	1288.31	0.0624
150	-4	55	261234	1264.09	0.0614
150	-4	60	250062	1244.80	0.0612
150	-4	65	233933	1218.74	0.0600
150	-4	70	215789	1203.83	0.0601
150	-4	75	198568	1181.73	0.0587
150	-4	80	184547	1158.88	0.0566
150	-4	85	175550	1138.49	0.0543
150	-4	90	172519	1140.13	0.0548
300	-4	0	122095	1224.41	0.0480
300	-4	5	124795	1239.16	0.0504
300	-4	10	132628	1288.85	0.0580
300	-4	15	145252	1382.92	0.0711
300	-4	20	161981	1441.16	0.0796
300	-4	25	181586	1440.55	0.0809
300	-4	30	202468	1402.52	0.0775
300	-4	35	222549	1349.35	0.0719
300	-4	40	239343	1310.79	0.0681
300	-4	45	250506	1289.12	0.0668
300	-4	50	254298	1257.92	0.0645
300	-4	55	250359	1233.28	0.0634
300	-4	60	239494	1215.81	0.0634
300	-4	65	223957	1195.82	0.0631
300	-4	70	206520	1178.39	0.0628
300	-4	75	189953	1153.65	0.0609
300	-4	80	176488	1131.40	0.0589
300	-4	85	167875	1119.81	0.0578
300	-4	90	164927	1119.99	0.0581
450	-4	0	115616	1271.04	0.0698
450	-4	5	118228	1283.79	0.0720
450	-4	10	125678	1320.30	0.0778

Temperature (°C)	**Log($\dot{\epsilon}$)**	$\boldsymbol{\theta}(^\circ)$	$\boldsymbol{E}$ **(MPa)**	$\boldsymbol{K}$ **(MPa)**	$\boldsymbol{n}$ **(unitless)**
450	-4	15	137704	1410.90	0.0901
450	-4	20	153603	1457.61	0.0969
450	-4	25	172239	1460.35	0.0982
450	-4	30	192148	1432.92	0.0957
450	-4	35	211179	1393.31	0.0916
450	-4	40	227041	1357.51	0.0880
450	-4	45	237506	1322.86	0.0848
450	-4	50	241014	1298.53	0.0834
450	-4	55	237070	1273.53	0.0822
450	-4	60	226697	1256.54	0.0824
450	-4	65	211776	1236.58	0.0821
450	-4	70	195157	1213.89	0.0812
450	-4	75	179387	1190.25	0.0796
450	-4	80	166597	1168.73	0.0777
450	-4	85	158357	1155.05	0.0764
450	-4	90	155520	1147.06	0.0754
600	-4	0	107627	1394.13	0.0872
600	-4	5	110041	1406.77	0.0893
600	-4	10	117087	1461.54	0.0968
600	-4	15	128449	1526.07	0.1054
600	-4	20	143428	1570.19	0.1114
600	-4	25	160999	1579.48	0.1132
600	-4	30	179621	1553.36	0.1109
600	-4	35	197516	1506.68	0.1060
600	-4	40	212413	1464.27	0.1017
600	-4	45	222173	1430.55	0.0988
600	-4	50	225351	1395.65	0.0961
600	-4	55	221572	1377.93	0.0960
600	-4	60	211647	1356.16	0.0957
600	-4	65	197522	1338.73	0.0959
600	-4	70	181821	1323.28	0.0961

Temperature (°C)	**Log($\dot{\epsilon}$)**	$\boldsymbol{\theta}(^\circ)$	$\boldsymbol{E}$ **(MPa)**	$\boldsymbol{K}$ **(MPa)**	$\boldsymbol{n}$ **(unitless)**
600	-4	75	166861	1298.03	0.0944
600	-4	80	154815	1274.00	0.0923
600	-4	85	147042	1257.50	0.0907
600	-4	90	144449	1250.73	0.0900
750	-4	0	98158	1304.68	0.0551
750	-4	5	100286	1348.67	0.0602
750	-4	10	106892	1445.95	0.0717
750	-4	15	117375	1598.79	0.0882
750	-4	20	131348	1701.65	0.0991
750	-4	25	147718	1731.56	0.1025
750	-4	30	165046	1722.64	0.1016
750	-4	35	181673	1667.25	0.0961
750	-4	40	195453	1624.68	0.0918
750	-4	45	204581	1591.85	0.0890
750	-4	50	207452	1573.50	0.0881
750	-4	55	203859	1549.78	0.0872
750	-4	60	194521	1547.44	0.0889
750	-4	65	181348	1535.74	0.0895
750	-4	70	166605	1516.91	0.0891
750	-4	75	152602	1495.06	0.0878
750	-4	80	141340	1460.55	0.0846
750	-4	85	134091	1447.53	0.0833
750	-4	90	131692	1443.95	0.0829
900	-4	0	87026	1320.06	0.1648
900	-4	5	88952	1333.56	0.1668
900	-4	10	94940	1368.04	0.1722
900	-4	15	104675	1410.83	0.1784
900	-4	20	117422	1455.78	0.1842
900	-4	25	132395	1466.10	0.1852
900	-4	30	148354	1440.71	0.1816
900	-4	35	163617	1419.00	0.1781

Temperature (°C)	**Log($\dot{\epsilon}$)**	$\boldsymbol{\theta}(^\circ)$	$\boldsymbol{E}$ **(MPa)**	$\boldsymbol{K}$ **(MPa)**	$\boldsymbol{n}$ **(unitless)**
900	-4	40	176288	1401.22	0.1751
900	-4	45	184623	1398.90	0.1744
900	-4	50	187355	1405.90	0.1754
900	-4	55	183976	1393.54	0.1743
900	-4	60	175363	1386.35	0.1742
900	-4	65	163191	1410.66	0.1780
900	-4	70	149618	1404.60	0.1778
900	-4	75	136658	1394.62	0.1767
900	-4	80	126238	1377.92	0.1745
900	-4	85	119579	1361.88	0.1721
900	-4	90	117349	1382.73	0.1745
1050	-4	0	74210	678.96	0.0994
1050	-4	5	76009	678.41	0.0998
1050	-4	10	81367	680.44	0.1017
1050	-4	15	89959	672.28	0.1010
1050	-4	20	100994	649.66	0.0959
1050	-4	25	113834	616.65	0.0869
1050	-4	30	127279	575.73	0.0744
1050	-4	35	139907	537.28	0.0616
1050	-4	40	150292	506.49	0.0507
1050	-4	45	157057	489.32	0.0443
1050	-4	50	159280	482.18	0.0417
1050	-4	55	156671	487.86	0.0442
1050	-4	60	149766	500.79	0.0494
1050	-4	65	139992	522.40	0.0575
1050	-4	70	129532	547.03	0.0662
1050	-4	75	118540	564.81	0.0720
1050	-4	80	109367	572.61	0.0742
1050	-4	85	103439	581.18	0.0764
1050	-4	90	101164	577.13	0.0751
20	-5	0	129754	1220.11	0.0412

Temperature (°C)	**Log($\dot{\epsilon}$)**	$\boldsymbol{\theta}(^\circ)$	$\boldsymbol{E}$ **(MPa)**	$\boldsymbol{K}$ **(MPa)**	$\boldsymbol{n}$ **(unitless)**
20	-5	5	132597	1235.05	0.0437
20	-5	10	140902	1301.21	0.0534
20	-5	15	154477	1408.39	0.0680
20	-5	20	172333	1462.17	0.0760
20	-5	25	193438	1463.17	0.0775
20	-5	30	215891	1426.32	0.0743
20	-5	35	237540	1370.97	0.0688
20	-5	40	255745	1326.39	0.0642
20	-5	45	268004	1310.87	0.0637
20	-5	50	272459	1268.97	0.0603
20	-5	55	268515	1246.92	0.0595
20	-5	60	257039	1234.68	0.0601
20	-5	65	240510	1217.53	0.0602
20	-5	70	221844	1194.36	0.0591
20	-5	75	204143	1172.72	0.0576
20	-5	80	189704	1153.50	0.0559
20	-5	85	180523	1138.96	0.0545
20	-5	90	177310	1130.20	0.0534
150	-5	0	126891	1223.39	0.0454
150	-5	5	129560	1231.21	0.0469
150	-5	10	137665	1295.72	0.0564
150	-5	15	150821	1387.59	0.0693
150	-5	20	168256	1440.58	0.0772
150	-5	25	188703	1439.96	0.0785
150	-5	30	210487	1403.95	0.0753
150	-5	35	231458	1354.93	0.0703
150	-5	40	249066	1312.02	0.0660
150	-5	45	260800	1293.72	0.0651
150	-5	50	264964	1262.88	0.0629
150	-5	55	260967	1238.54	0.0618
150	-5	60	249780	1220.18	0.0617

Temperature (°C)	**Log($\dot{\epsilon}$)**	$\boldsymbol{\theta}(^\circ)$	$\boldsymbol{E}$ **(MPa)**	$\boldsymbol{K}$ **(MPa)**	$\boldsymbol{n}$ **(unitless)**
150	-5	65	233694	1203.74	0.0619
150	-5	70	215568	1180.85	0.0608
150	-5	75	198342	1161.01	0.0596
150	-5	80	184383	1141.17	0.0579
150	-5	85	175337	1119.47	0.0554
150	-5	90	172314	1121.34	0.0559
300	-5	0	121988	1198.91	0.0501
300	-5	5	124602	1208.05	0.0518
300	-5	10	132402	1250.54	0.0586
300	-5	15	145052	1348.54	0.0725
300	-5	20	161770	1404.76	0.0810
300	-5	25	181359	1406.38	0.0825
300	-5	30	202284	1363.39	0.0783
300	-5	35	222290	1318.55	0.0736
300	-5	40	239101	1283.78	0.0702
300	-5	45	250261	1263.43	0.0690
300	-5	50	254169	1232.92	0.0667
300	-5	55	250068	1207.78	0.0655
300	-5	60	239212	1190.19	0.0655
300	-5	65	223709	1170.38	0.0651
300	-5	70	206287	1146.18	0.0637
300	-5	75	189751	1123.03	0.0621
300	-5	80	176303	1102.93	0.0602
300	-5	85	167659	1092.38	0.0593
300	-5	90	164765	1085.28	0.0585
450	-5	0	115634	1237.38	0.0717
450	-5	5	118041	1250.91	0.0739
450	-5	10	125495	1292.14	0.0804
450	-5	15	137561	1373.63	0.0918
450	-5	20	153439	1423.70	0.0991
450	-5	25	172098	1426.71	0.1005

Temperature (°C)	**Log($\dot{\epsilon}$)**	**θ(°)**	**E (MPa)**	**K (MPa)**	**n (unitless)**
450	-5	30	191913	1394.53	0.0973
450	-5	35	210922	1356.64	0.0932
450	-5	40	226775	1322.15	0.0896
450	-5	45	237241	1297.70	0.0877
450	-5	50	240811	1273.34	0.0862
450	-5	55	236866	1248.69	0.0850
450	-5	60	226430	1230.93	0.0851
450	-5	65	211598	1204.40	0.0838
450	-5	70	194927	1181.95	0.0829
450	-5	75	179103	1158.91	0.0813
450	-5	80	166380	1139.34	0.0797
450	-5	85	158134	1125.90	0.0783
450	-5	90	155401	1119.85	0.0777
600	-5	0	107608	1360.17	0.0909
600	-5	5	109888	1373.44	0.0930
600	-5	10	116926	1416.29	0.0993
600	-5	15	128235	1476.85	0.1076
600	-5	20	143240	1523.34	0.1140
600	-5	25	160783	1535.71	0.1161
600	-5	30	179453	1510.80	0.1138
600	-5	35	197324	1466.67	0.1091
600	-5	40	212207	1427.29	0.1050
600	-5	45	221961	1394.64	0.1020
600	-5	50	225170	1366.24	0.1001
600	-5	55	221396	1342.96	0.0993
600	-5	60	211451	1325.86	0.0995
600	-5	65	197364	1303.54	0.0990
600	-5	70	181599	1281.81	0.0983
600	-5	75	166685	1258.00	0.0969
600	-5	80	154633	1234.66	0.0948
600	-5	85	146916	1219.47	0.0933

Temperature (°C)	**Log($\dot{\epsilon}$)**	**θ(°)**	***E* (MPa)**	***K* (MPa)**	***n* (unitless)**
600	-5	90	144276	1212.23	0.0925
750	-5	0	98033	1311.42	0.0611
750	-5	5	100181	1350.21	0.0657
750	-5	10	106695	1428.82	0.0754
750	-5	15	117234	1570.49	0.0913
750	-5	20	131160	1701.14	0.1050
750	-5	25	147491	1694.23	0.1050
750	-5	30	164901	1675.23	0.1032
750	-5	35	181474	1628.66	0.0985
750	-5	40	195298	1591.17	0.0947
750	-5	45	204350	1558.77	0.0918
750	-5	50	207268	1540.27	0.0909
750	-5	55	203665	1516.98	0.0900
750	-5	60	194346	1514.32	0.0917
750	-5	65	181127	1490.15	0.0909
750	-5	70	166434	1475.41	0.0909
750	-5	75	152459	1459.75	0.0902
750	-5	80	141176	1431.20	0.0875
750	-5	85	133967	1408.64	0.0852
750	-5	90	131507	1403.71	0.0846
900	-5	0	86901	1316.45	0.1751
900	-5	5	88838	1323.55	0.1764
900	-5	10	94849	1367.84	0.1830
900	-5	15	104485	1375.18	0.1852
900	-5	20	117249	1423.21	0.1915
900	-5	25	132236	1417.66	0.1908
900	-5	30	148155	1404.36	0.1886
900	-5	35	163437	1378.29	0.1846
900	-5	40	176158	1359.03	0.1814
900	-5	45	184500	1353.74	0.1804
900	-5	50	187163	1357.33	0.1810

Temperature (°C)	**Log($\dot{\epsilon}$)**	**θ(°)**	**E (MPa)**	**K (MPa)**	**n (unitless)**
900	-5	55	183826	1347.79	0.1802
900	-5	60	175204	1344.47	0.1805
900	-5	65	163045	1372.55	0.1848
900	-5	70	149371	1373.42	0.1855
900	-5	75	136503	1351.30	0.1828
900	-5	80	126148	1349.83	0.1824
900	-5	85	119453	1342.25	0.1810
900	-5	90	117230	1337.75	0.1803
1050	-5	0	67952	292.68	0.0445
1050	-5	5	75926	332.45	0.0681
1050	-5	10	78533	318.17	0.0605
1050	-5	15	89791	338.47	0.0725
1050	-5	20	100779	330.96	0.0689
1050	-5	25	112244	318.05	0.0617
1050	-5	30	124523	303.17	0.0529
1050	-5	35	135791	288.59	0.0438
1050	-5	40	144826	278.09	0.0369
1050	-5	45	150623	271.04	0.0322
1050	-5	50	152453	268.54	0.0307
1050	-5	55	150210	269.99	0.0320
1050	-5	60	144484	275.00	0.0358
1050	-5	65	136156	281.36	0.0405
1050	-5	70	129054	293.15	0.0484
1050	-5	75	118066	295.31	0.0500
1050	-5	80	109041	297.62	0.0515
1050	-5	85	103309	299.86	0.0528
1050	-5	90	100584	295.50	0.0501
20	-6	0	129732	1212.42	0.0426
20	-6	5	132483	1224.55	0.0447
20	-6	10	140842	1295.13	0.0550
20	-6	15	154362	1386.42	0.0679

Temperature (°C)	**Log($\dot{\epsilon}$)**	**θ(°)**	**E (MPa)**	**K (MPa)**	**n (unitless)**
20	-6	20	172255	1439.72	0.0759
20	-6	25	193291	1439.89	0.0773
20	-6	30	215826	1403.20	0.0741
20	-6	35	237428	1358.37	0.0696
20	-6	40	255640	1310.97	0.0646
20	-6	45	267914	1297.75	0.0645
20	-6	50	272301	1254.09	0.0608
20	-6	55	268371	1254.21	0.0628
20	-6	60	256913	1221.87	0.0607
20	-6	65	240347	1206.31	0.0610
20	-6	70	221727	1186.69	0.0606
20	-6	75	203868	1160.52	0.0583
20	-6	80	189581	1143.95	0.0570
20	-6	85	180347	1128.96	0.0555
20	-6	90	177162	1120.72	0.0544
150	-6	0	126779	1195.92	0.0455
150	-6	5	129479	1217.08	0.0488
150	-6	10	137634	1284.27	0.0587
150	-6	15	150792	1365.71	0.0705
150	-6	20	168149	1413.91	0.0779
150	-6	25	188578	1418.86	0.0799
150	-6	30	210420	1383.86	0.0767
150	-6	35	231310	1336.56	0.0718
150	-6	40	249029	1298.03	0.0680
150	-6	45	260690	1268.85	0.0656
150	-6	50	264925	1250.09	0.0650
150	-6	55	260823	1225.50	0.0639
150	-6	60	249689	1207.18	0.0638
150	-6	65	233563	1180.74	0.0624
150	-6	70	215439	1144.25	0.0593
150	-6	75	198227	1148.71	0.0617

Temperature (°C)	**Log($\dot{\epsilon}$)**	**θ(°)**	**E (MPa)**	**K (MPa)**	**n (unitless)**
150	-6	80	184223	1122.98	0.0591
150	-6	85	175254	1101.85	0.0566
150	-6	90	172219	1103.73	0.0571
300	-6	0	121953	1173.00	0.0520
300	-6	5	124521	1190.95	0.0548
300	-6	10	132345	1225.27	0.0607
300	-6	15	144940	1313.12	0.0736
300	-6	20	161663	1369.41	0.0822
300	-6	25	181277	1369.63	0.0836
300	-6	30	202145	1334.07	0.0801
300	-6	35	222176	1290.66	0.0754
300	-6	40	238958	1258.33	0.0722
300	-6	45	250145	1227.81	0.0696
300	-6	50	254146	1208.74	0.0688
300	-6	55	250011	1183.83	0.0676
300	-6	60	239103	1166.13	0.0675
300	-6	65	223617	1146.72	0.0671
300	-6	70	206171	1124.35	0.0660
300	-6	75	189528	1100.87	0.0642
300	-6	80	176207	1084.37	0.0629
300	-6	85	167591	1066.66	0.0609
300	-6	90	164597	1066.91	0.0611
450	-6	0	115539	1220.55	0.0754
450	-6	5	117989	1233.89	0.0776
450	-6	10	125411	1266.02	0.0830
450	-6	15	137425	1336.30	0.0933
450	-6	20	153351	1389.73	0.1011
450	-6	25	171982	1391.24	0.1022
450	-6	30	191838	1366.77	0.0998
450	-6	35	210799	1330.16	0.0957
450	-6	40	226656	1298.14	0.0924

Temperature (°C)	**Log($\dot{\epsilon}$)**	$\boldsymbol{\theta}(^\circ)$	$\boldsymbol{E}$ **(MPa)**	$\boldsymbol{K}$ **(MPa)**	$\boldsymbol{n}$ **(unitless)**
450	-6	45	237166	1274.38	0.0905
450	-6	50	240782	1250.14	0.0890
450	-6	55	236786	1225.43	0.0878
450	-6	60	226277	1207.07	0.0877
450	-6	65	211442	1180.89	0.0864
450	-6	70	194784	1159.10	0.0855
450	-6	75	178976	1137.23	0.0841
450	-6	80	166283	1112.37	0.0816
450	-6	85	158083	1100.04	0.0805
450	-6	90	155358	1094.50	0.0798
600	-6	0	107544	1327.64	0.0943
600	-6	5	109869	1341.49	0.0965
600	-6	10	116872	1385.91	0.1030
600	-6	15	128162	1434.03	0.1101
600	-6	20	143118	1480.67	0.1166
600	-6	25	160703	1491.17	0.1185
600	-6	30	179387	1473.27	0.1168
600	-6	35	197242	1431.20	0.1121
600	-6	40	212098	1393.79	0.1081
600	-6	45	221855	1362.45	0.1052
600	-6	50	225097	1334.94	0.1034
600	-6	55	221316	1311.55	0.1024
600	-6	60	211402	1294.69	0.1027
600	-6	65	197296	1276.38	0.1027
600	-6	70	181485	1249.90	0.1013
600	-6	75	166565	1226.59	0.0999
600	-6	80	154558	1204.14	0.0979
600	-6	85	146833	1184.72	0.0958
600	-6	90	144194	1177.75	0.0950
750	-6	0	98000	1327.03	0.0678
750	-6	5	100105	1352.63	0.0710

Temperature (°C)	**Log($\dot{\epsilon}$)**	$\boldsymbol{\theta}(^\circ)$	$\boldsymbol{E}$ **(MPa)**	$\boldsymbol{K}$ **(MPa)**	$\boldsymbol{n}$ **(unitless)**
750	-6	10	106639	1412.86	0.0790
750	-6	15	117173	1562.17	0.0959
750	-6	20	131087	1663.66	0.1071
750	-6	25	147435	1674.28	0.1088
750	-6	30	164762	1639.09	0.1054
750	-6	35	181382	1594.39	0.1007
750	-6	40	195233	1559.31	0.0971
750	-6	45	204336	1528.16	0.0943
750	-6	50	207135	1507.26	0.0931
750	-6	55	203628	1485.54	0.0924
750	-6	60	194240	1482.22	0.0939
750	-6	65	181048	1459.61	0.0933
750	-6	70	166330	1447.31	0.0935
750	-6	75	152344	1422.72	0.0918
750	-6	80	141130	1401.87	0.0899
750	-6	85	133881	1381.51	0.0877
750	-6	90	131486	1380.63	0.0877
900	-6	0	86862	1070.96	0.1578
900	-6	5	88812	1089.32	0.1611
900	-6	10	94791	1104.41	0.1646
900	-6	15	104415	1111.33	0.1670
900	-6	20	117168	1122.54	0.1695
900	-6	25	132187	1114.71	0.1686
900	-6	30	148083	1088.07	0.1641
900	-6	35	163357	1056.88	0.1585
900	-6	40	176105	1044.67	0.1560
900	-6	45	184361	1020.99	0.1518
900	-6	50	187105	1019.02	0.1516
900	-6	55	183667	1015.51	0.1515
900	-6	60	175125	1031.34	0.1548
900	-6	65	162985	1041.34	0.1572

Temperature (°C)	**Log($\dot{\epsilon}$)**	**θ(°)**	***E* (MPa)**	***K* (MPa)**	***n* (unitless)**
900	-6	70	149309	1039.15	0.1572
900	-6	75	136427	1049.28	0.1589
900	-6	80	126055	1041.26	0.1573
900	-6	85	119369	1040.89	0.1569
900	-6	90	117176	1040.64	0.1567
1050	-6	0	73601	185.55	0.0521
1050	-6	5	75894	187.28	0.0540
1050	-6	10	79641	187.00	0.0538
1050	-6	15	86158	186.73	0.0538
1050	-6	20	95369	185.87	0.0531
1050	-6	25	106330	182.88	0.0502
1050	-6	30	125220	181.96	0.0495
1050	-6	35	136610	177.11	0.0445
1050	-6	40	145770	173.34	0.0406
1050	-6	45	151620	170.96	0.0381
1050	-6	50	153460	170.04	0.0374
1050	-6	55	151210	170.29	0.0380
1050	-6	60	145430	171.57	0.0398
1050	-6	65	137000	173.44	0.0422
1050	-6	70	130140	176.69	0.0460
1050	-6	75	115630	175.50	0.0449
1050	-6	80	107690	175.88	0.0455
1050	-6	85	102780	175.78	0.0455
1050	-6	90	98722	174.21	0.0438
20	-8	0	129670	1194.70	0.0450
20	-8	5	132442	1206.21	0.0470
20	-8	10	140792	1267.09	0.0563
20	-8	15	154363	1359.68	0.0695
20	-8	20	172198	1413.19	0.0776
20	-8	25	193255	1408.90	0.0786
20	-8	30	215697	1374.83	0.0755

Temperature (°C)	**Log($\dot{\epsilon}$)**	**θ(°)**	***E* (MPa)**	***K* (MPa)**	***n* (unitless)**
20	-8	35	237365	1333.91	0.0714
20	-8	40	255610	1287.93	0.0666
20	-8	45	267847	1274.05	0.0664
20	-8	50	272224	1254.82	0.0656
20	-8	55	268231	1213.77	0.0621
20	-8	60	256815	1211.33	0.0643
20	-8	65	240342	1150.67	0.0579
20	-8	70	221719	1162.68	0.0619
20	-8	75	203890	1138.65	0.0601
20	-8	80	189530	1114.60	0.0576
20	-8	85	180271	1101.65	0.0563
20	-8	90	177259	1096.75	0.0558
150	-8	0	126746	1170.72	0.0494
150	-8	5	129429	1187.93	0.0522
150	-8	10	137560	1241.67	0.0606
150	-8	15	150696	1316.23	0.0719
150	-8	20	168145	1371.00	0.0803
150	-8	25	188463	1370.25	0.0815
150	-8	30	210298	1340.92	0.0789
150	-8	35	231222	1297.40	0.0742
150	-8	40	248959	1261.51	0.0706
150	-8	45	260555	1231.56	0.0681
150	-8	50	264858	1213.72	0.0675
150	-8	55	260813	1189.29	0.0663
150	-8	60	249632	1172.04	0.0663
150	-8	65	233509	1154.97	0.0662
150	-8	70	215405	1127.30	0.0643
150	-8	75	198081	1108.17	0.0632
150	-8	80	184169	1087.42	0.0612
150	-8	85	175196	1076.29	0.0602
150	-8	90	172264	1070.89	0.0596

Temperature (°C)	**Log($\dot{\epsilon}$)**	**θ(°)**	**E (MPa)**	**K (MPa)**	**n (unitless)**
300	-8	0	121867	1124.62	0.0556
300	-8	5	124487	1140.37	0.0583
300	-8	10	132292	1181.61	0.0653
300	-8	15	144912	1262.36	0.0777
300	-8	20	161571	1306.21	0.0850
300	-8	25	181224	1308.96	0.0866
300	-8	30	202108	1277.95	0.0834
300	-8	35	222140	1240.07	0.0792
300	-8	40	238887	1210.69	0.0763
300	-8	45	250012	1191.56	0.0751
300	-8	50	253828	1160.11	0.0724
300	-8	55	249910	1136.78	0.0713
300	-8	60	239050	1120.41	0.0713
300	-8	65	223493	1101.74	0.0710
300	-8	70	206085	1077.31	0.0694
300	-8	75	189576	1055.98	0.0678
300	-8	80	176134	1039.79	0.0665
300	-8	85	167525	1024.34	0.0647
300	-8	90	164648	1018.78	0.0641
450	-8	0	115505	1170.05	0.0800
450	-8	5	117935	1179.45	0.0817
450	-8	10	125384	1214.27	0.0875
450	-8	15	137377	1279.77	0.0975
450	-8	20	153301	1334.98	0.1057
450	-8	25	171884	1338.45	0.1070
450	-8	30	191711	1309.38	0.1038
450	-8	35	210694	1282.33	0.1007
450	-8	40	226612	1253.88	0.0977
450	-8	45	237138	1230.72	0.0957
450	-8	50	240638	1205.87	0.0940
450	-8	55	236679	1181.66	0.0928

Temperature (°C)	**Log($\dot{\epsilon}$)**	**θ(°)**	**E (MPa)**	**K (MPa)**	**n (unitless)**
450	-8	60	226304	1164.54	0.0928
450	-8	65	211407	1138.70	0.0915
450	-8	70	194736	1117.78	0.0907
450	-8	75	178932	1091.61	0.0885
450	-8	80	166220	1068.55	0.0862
450	-8	85	158031	1051.97	0.0843
450	-8	90	155289	1046.33	0.0837
600	-8	0	107526	1275.52	0.1014
600	-8	5	109819	1284.23	0.1029
600	-8	10	116821	1327.22	0.1094
600	-8	15	128122	1370.51	0.1160
600	-8	20	143069	1418.40	0.1228
600	-8	25	160676	1425.83	0.1242
600	-8	30	179267	1406.11	0.1221
600	-8	35	197155	1374.41	0.1184
600	-8	40	211946	1340.04	0.1146
600	-8	45	221788	1311.26	0.1118
600	-8	50	225037	1284.48	0.1099
600	-8	55	221131	1264.16	0.1093
600	-8	60	211267	1243.36	0.1090
600	-8	65	197197	1224.47	0.1089
600	-8	70	181502	1200.03	0.1078
600	-8	75	166541	1172.67	0.1057
600	-8	80	154498	1146.64	0.1031
600	-8	85	146765	1130.61	0.1014
600	-8	90	144180	1124.73	0.1008
750	-8	0	97941	1318.94	0.0759
750	-8	5	100109	1341.25	0.0790
750	-8	10	106960	1413.80	0.0886
750	-8	15	117129	1524.86	0.1018
750	-8	20	130997	1627.38	0.1134

Temperature (°C)	**Log($\dot{\epsilon}$)**	**θ(°)**	**E (MPa)**	**K (MPa)**	**n (unitless)**
750	-8	25	147400	1642.85	0.1156
750	-8	30	164709	1582.07	0.1095
750	-8	35	181267	1550.03	0.1060
750	-8	40	195087	1506.62	0.1014
750	-8	45	204202	1475.95	0.0986
750	-8	50	207151	1456.59	0.0976
750	-8	55	203515	1446.53	0.0981
750	-8	60	194203	1432.27	0.0983
750	-8	65	180944	1421.99	0.0991
750	-8	70	166219	1401.34	0.0983
750	-8	75	152294	1374.08	0.0962
750	-8	80	141074	1361.24	0.0952
750	-8	85	133866	1335.16	0.0923
750	-8	90	131444	1334.57	0.0923
900	-8	0	86836	291.71	0.0179
900	-8	5	88785	292.95	0.0188
900	-8	10	94775	298.45	0.0225
900	-8	15	104396	305.64	0.0272
900	-8	20	117120	307.33	0.0287
900	-8	25	132140	306.42	0.0285
900	-8	30	148058	298.58	0.0241
900	-8	35	163318	286.63	0.0174
900	-8	40	176008	279.48	0.0133
900	-8	45	184293	274.38	0.0104
900	-8	50	187080	272.27	0.0091
900	-8	55	183673	273.87	0.0105
900	-8	60	175047	276.76	0.0127
900	-8	65	162868	280.72	0.0153
900	-8	70	149240	284.09	0.0176
900	-8	75	136393	283.62	0.0175
900	-8	80	126038	281.80	0.0165

Temperature (°C)	**Log($\dot{\epsilon}$)**	$\boldsymbol{\theta}(^\circ)$	$\boldsymbol{E}$ **(MPa)**	$\boldsymbol{K}$ **(MPa)**	$\boldsymbol{n}$ **(unitless)**
900	-8	85	119353	280.27	0.0155
900	-8	90	117148	279.13	0.0148
1050	-8	0	73976	60.44	0.0172
1050	-8	5	75831	60.62	0.0178
1050	-8	10	77514	60.64	0.0179
1050	-8	15	86306	60.91	0.0189
1050	-8	20	94405	60.70	0.0184
1050	-8	25	110760	60.69	0.0186
1050	-8	30	128690	60.34	0.0177
1050	-8	35	142030	59.79	0.0162
1050	-8	40	153130	59.23	0.0148
1050	-8	45	160380	58.87	0.0139
1050	-8	50	162790	58.63	0.0135
1050	-8	55	159970	58.60	0.0137
1050	-8	60	152600	58.64	0.0142
1050	-8	65	138730	58.64	0.0145
1050	-8	70	129670	58.78	0.0152
1050	-8	75	118750	58.86	0.0157
1050	-8	80	109380	58.70	0.0154
1050	-8	85	103070	58.46	0.0147
1050	-8	90	100280	58.44	0.0147

REFERENCES

[1] JPEG Image, September 2012. cited 2/1/2013. http://www.alstom.com/press-centre.

[2] W. Esser, "Directional Solidification of Blades for Industrial Gas Turbines," in *Materials for Advanced Power Engineering, Part I* (D. C. et al., ed.), pp. 641–659, Kluwer Academic Publishers, 1994.

[3] K. Harris, "High ductility nickel alloy directional casting of parts for high temperature and stress operation," tech. rep., Cannon-Muskegon Corporation: United States, 1984.

[4] R. A. Kupkovits, "Thermomechanical Fatigue Behavior of the Directionally-Solidified Ni-base Superalloy CM247LC," Master's Thesis, Georgia Institute of Technology, Atlanta, GA, 2008.

[5] A. P. Gordon, *Crack Initiation Modeling of a Directionally Solidified Ni-base Superalloy.* Ph.D. Dissertation, Georgia Institute of Technology, Atlanta, GA, 2006.

[6] M. M. Shenoy, D. L. McDowell, and R. W. Neu, "Transversely Isotropic Viscoplasticity Model for a Directionally Solidified Ni-base Superalloy," *International Journal of Plasticity*, vol. 22, no. 12, pp. 2301–2326, 2006.

[7] R. Neu and H. Sehitoglu, "Thermomechanical Fatigue, Oxidation, and Creep: Part I. Damage Mechanisms.," *Metallurgical and Materials Transactions A*, vol. 20, no. 9, p. 1755, 1989.

[8] H. Sehitoglu and D. A. Boismier, "Thermo-Mechanical Fatigue of Mar-M247: Part 2- Life Prediction," *Journal of Engineering Materials and Technology*, vol. 112, no. 1, p. 80, 1990.

[9] R. L. Amaro, *Thermomechanical Fatigue Crack Formation in a Single Crystal Ni-base Superalloy.* Ph.D. Dissertation, Georgia Institute of Technology, Atlanta, GA, 2011.

[10] H. Neuber, *Theory of Notch Stresses: Principles for Exact Calculation of Strength with Reference to Strutural Form and Material.* Springer Verlag, 2nd ed., 1958.

[11] W. Ramberg and W. R. Osgood, "Description of Stress Strain Curves by Three Parameters," *National Advisory Committee for Aeronautics (NACA), Technical Note 902*, 1943.

[12] J. A. Bannantine, J. Comer, and J. L. Handrock, *Fundamentals of Metal Fatigue Analysis.* Prentice Hall, 1990.

[13] K. Molski and G. Glinka, "A Method of Elastic-Plastic Stress and Strain Calculation at a Notch Root," *Materials Science and Engineering*, vol. 50, pp. 93 – 100, 1981.

[14] G. Glinka, W. Ott, and H. Nowack, "Elastoplastic Plane Strain Analysis of Stresses and Strains at the Notch Root," *Journal of Engineering Materials and Technology*, vol. 110, pp. 195 – 204, 1988.

[15] J. Sharpe, W.N., C. Yang, and R. Tregoning, "An Evaluation of the Neuber and Glinka Relations for Monotonic Loading," *Transactions of the ASME. Journal of Applied Mechanics*, vol. 59, no. 2, 1992.

[16] Z. J. Moore, "Life Modeling of Notched CM247LC DS Nickel-base Superalloy," Master's Thesis, Georgia Institute of Technology, Atlanta, GA, 2008.

[17] R. Mucke and O.-E. Bernhardi, "A Constitutive Model for Anisotropic Materials Based on Neubers Rule.," *Computer Methods in Applied Mechanics and Engineering*, vol. 192, pp. 4237 – 4255, 2003.

[18] "Abaqus v6.11-1," 2011.

[19] M. Chaudonneret and J. Culie, "Adaptation of Neuber's Theory for Stress Concentration in Viscoplasticity.," *Recherche Aerospatiale*, no. 4, pp. 243 – 250, 1985.

[20] J. Chaboche, "Constitutive Equations for Cyclic Plasticity and Cyclic Viscoplasticity.," *International Journal of Plasticity*, vol. 5, pp. 247 – 302, 1989.

[21] A. A. Moftakhar, G. Glinka, D. Scarth, and D. Kawa, "Multiaxial Stress-Strain Creep Analysis for Notches.," *ASTM STP 1184*, pp. 230–243, 1994.

[22] A. Moftakhar, A. Buczynski, and G. Glinka, "Calculation of Elasto-Plastic Strains and Stresses in Notches under Multiaxial Loading.," *International Journal of Fracture*, vol. 70, no. 4, p. 357, 1995.

[23] P. Fernandez-Zelaia, "Thermomechanical Fatigue Crack Formation in Nickel-Base Superalloys at Notches," Master's Thesis, Georgia Institute of Technology, Atlanta, GA, 2012.

[24] L. F. Coffin Jr., "Study of the Effects of Cyclic Thermal Stresses on a Ductile Metal.," *Transactions of the American Society of Mechanical Engineers*, vol. 76, pp. 931 – 950, 1954.

[25] W. Ostergren, "A Damage Function and Associated Failure Equations for Predicting Hold Time and Frequency Effects in Elevated Temperature, Low Cycle Fatigue.," *Journal of Testing and Evaluation*, vol. 4, no. 5, p. 1, 1976.

[26] S. Y. Zamrik and M. L. Renauld, "Thermo-mechanical Out-of-Phase Fatigue Life of Overlay Coated IN-738LC Gas Turbine Material.," *ASTM STP 1371*, pp. 119 – 137, 2000.

[27] D. McDowell, S. Antolovich, and R. Oehmke, "Mechanistic Considerations for TMF Life Prediction of Nickel-base Superalloys.," in *Nuclear Engineering and Design*, vol. 133, pp. 383 – 399, 1992.

[28] H. Sehitoglu, "Thermo-mechanical Fatigue Life Prediction Methods.," *Advances in Fatigue Lifetime Predictive Techniques, ASTM STP 1122*, pp. 47 – 76, 1992.

[29] R. Neu and H. Sehitoglu, "Thermomechanical Fatigue, Oxidation, and Creep: Part II. Life Prediction.," *Metallurgical and Materials Transactions A*, vol. 20, no. 9, p. 1769, 1989.

[30] F. R. Larson and J. Miller, "Time-Temperature Relationship for Rupture and Creep Stresses.," *Transactions of the American Society of Mechanical Engineers*, vol. 74, pp. 765 – 771, 1952.

[31] P. Domas and S. D. Antolovich, "A Mechanistically Based Model for high temperature notched lcf of rene 80.," *Engineering Fracture Mechanics*, vol. 21, no. 1, pp. 203 – 214, 1985.

[32] R. Mucke and H. Kiewel, "Nonlocal Cyclic Life Prediction for Gas Turbine Components with Sharply Notched Geometries.," *Journal of Engineering for Gas Turbines and Power-Transactions of the ASME*, vol. 130, no. 1, 2008.

[33] D. Taylor, "The Theory of Critical Distances.," *Engineering Fracture Mechanics*, vol. 75, no. Critical Distance Theories of Fracture, pp. 1696 – 1705, 2007.

[34] R. Peterson, *Metal Fatigue*, vol. 3. McGraw-Hill New York, 1959.

[35] L. Susmel and D. Taylor, "A Novel Formulation of the Theory of Critical Distances to Estimate Lifetime of Notched Components in the Medium-Cycle Fatigue Regime.," *Fatigue & Fracture of Engineering Materials & Structures*, vol. 30, no. 7, pp. 567 – 581, 2007.

[36] L. Susmel and D. Taylor, "An Elasto-Plastic Reformulation of the Theory of Critical Distances to Estimate Lifetime of Notched Components Failing in the Low/Medium-Cycle Fatigue Regime.," *Journal of Engineering Materials and Technology-Transactions of the ASME*, vol. 132, no. 2, 2010.

[37] P. Domas and S. Antolovich, "An Integrated Local Energy Density Approach to Notch Low Cycle Fatigue Life Prediction.," *Engineering Fracture Mechanics*, vol. 21, pp. 187 – 202, 1985.

[38] A. Fatemi and D. Socie, "A Critical Plane Approach to Multiaxial Fatigue Damage Including Out-of-Phase Loading.," *Fatigue & Fracture of Engineering Materials & Structures*, vol. 11, no. 3, pp. 149 – 165, 1988.

[39] P. Fernandez-Zelaia and R. Neu, "Influence of Notch Severity on Thermomechanical Fatigue Life of a Directionally-Solidified Ni-base Superalloy," *Fatigue and Fracture of Materials and Structures*, submitted for publication. 2013.

[40] R. D. McGinty, *Multiscale Representation of Polycrystalline Inelasticity.* Ph.D. Dissertation, Georgia Institute of Technology, Atlanta, GA, 2001.

[41] M. M. Shenoy, *Constitutive Modeling and Life Prediction in Nickel-Base Superalloys.* Ph.D. Dissertation, Georgia Institute of Technology, Atlanta, GA, 2006.

[42] D. L. McDowell, "Viscoplasticity of Heterogeneous Metallic Materials.," *Materials Science & Engineering R*, vol. 62, pp. 67 – 123, 2008.

[43] E. H. Lee, "Elastic-Plastic Deformation at Finite Strains.," *Journal of Applied Mechanics*, vol. 36, pp. 1 – 6, 1969.

[44] S. R. Kalidindi, H. K. Duvvuru, and M. Knezevic, "Spectral Calibration of Crystal Plasticity Models," *Acta Materialia*, vol. 54, no. 7, pp. 1795 – 1804, 2006.

[45] M. Knezevic, H. F. Al-Harbi, and S. R. Kalidindi, "Crystal Plasticity Simulations using Discrete Fourier Transforms.," *Acta Materialia*, vol. 57, pp. 1777 – 1784, 2009.

[46] M. Knezevic, S. R. Kalidindi, and D. Fullwood, "Computationally Efficient Database and Spectral Interpolation for Fully Plastic Taylor-type Crystal Plasticity Calculations of Face-Centered Cubic Polycrystals," *International Journal of Plasticity*, vol. 24, no. 7, pp. 1264 – 1276, 2008.

[47] N. Huber and C. Tsakmakis, "A Neural Network tool for Identifying the Material Parameters of a Finite Deformation Viscoplasticity Model with Static Recovery," *Computer Methods in Applied Mechanics and Engineering*, vol. 191, no. 35, pp. 353 – 384, 2001.

[48] G. Yagawa and H. Okuda, "Neural Networks in Computational Mechanics," *Archives of Computational Methods in Engineering*, vol. 3, pp. 435–512, 1996.

[49] J. A. Anderson and E. Rosenfeld, *Neurocomputing: Foundations of Research.* The MIT Press, 1988.

[50] C. Lau, *Neural Networks : Theoretical Foundations and Analysis / edited by Clifford Lau.* New York : IEEE Press, c1992., 1992.

[51] S. Jung and J. Ghaboussi, "Neural Network Constitutive Model for Rate-Dependent Materials," *Computers & Structures*, vol. 84, no. 1516, pp. 955 – 963, 2006.

[52] M. Al-Haik, H. Garmestani, and I. Navon, "Truncated-Newton Training Algorithm for Neurocomputational Viscoplastic Model.," *Computer Methods in Applied Mechanics and Engineering*, vol. 192, pp. 2249 – 2267, 2003.

[53] M. Al-Haik, H. Garmestani, and A. Savran, "Explicit and Implicit Viscoplastic Models for Polymeric Composite.," *International Journal of Plasticity*, vol. 20, pp. 1875 – 1907, 2004.

[54] G. Liang and K. Chandrashekhara, "Neural Network Based Constitutive Model for Elastomeric Foams," *Engineering Structures*, vol. 30, no. 7, pp. 2002 – 2011, 2008.

[55] R. Ghajar, N. Naserifar, H. Sadati, and J. Alizadeh K, "A Neural Network Approach for Predicting Steel Properties Characterizing Cyclic Ramberg–Osgood Equation," *Fatigue & Fracture of Engineering Materials & Structures*, vol. 34, no. 7, pp. 534–544, 2011.

[56] V. K. Gupta, N. Kwatra, and S. Ray, "Artificial Neural Network Modeling of Creep Behavior in a Rotating Composite Disc," *Engineering Computations*, vol. 24, no. 2, pp. 151–151–151, 2007.

[57] M. Shenoy, Y. Tjiptowidjojo, and D. McDowell, "Microstructure-Sensitive Modeling of Polycrystalline IN 100.," *International Journal of Plasticity*, vol. 24, no. 10, pp. 1694 – 1730, 2008.

[58] R. Skelton, "The Determination of Hysteresis Loops in Thermomechanical Fatigue Using Isothermal Stress-Strain Data.," *Fatigue & Fracture of Engineering Materials & Structures*, vol. 17, no. 4, pp. 479 – 496, 1994.

[59] R. P. Skelton, G. Webster, B. de Mestral, and C. Wang, "Modelling Thermo-mechanical Fatigue Hysteresis Loops from Isothermal Cyclic Data," *ASTM STP 1371*, pp. 69–84, 2000.

[60] M. Kirka and R. Neu. Unpublished.

[61] T. Hasebe, M. Sakane, and M. Ohnami, "Elastic Anisotropy of Directionally Solidified Superalloy," *Journal of Engineering Materials and Technology*, vol. 114, no. 2, pp. 141–146, 1992.

[62] D. Robinson and W. Binienda, "Model of Viscoplasticity for Transversely Isotropic Inelastically Compressible Solids," *Journal of Engineering Mechanics*, vol. 127, no. 6, pp. 567–573, 2001.

[63] G. L. Erickson and K. Harris, *DS and SX Superalloys for Industrial Gas Turbines*. Liege, Belgium: Kluwer Academic Publisher's Group, 1994.

[64] M. Zhang, *Crystal Plasticity Modeling of Ti-6Al-4V and its Application in Cyclic and Fretting Fatigue Analysis*. Ph.D. Dissertation, Georgia Institute of Technology, Atlanta, GA, April 2008.

[65] E. S. Alley, *Influence of Microstructure in Rolling Contact Fatigue of Bearing Steels with Inclusions*. PhD thesis, Georgia Institute of Technology, Atlanta, GA, May 2009.

[66] B. Sumpter and D. Noid, "Potential Energy Surfaces for Macromolecules - a Neural Network Technique.," *Chemical Physics Letters*, vol. 192, no. 5-6, pp. 455 – 462, 1992.

[67] K. Genel, "Application of Artificial Neural Network for Predicting Strain-life Fatigue Properties of Steels on the Basis of Tensile Tests," *International Journal of Fatigue*, vol. 26, no. 10, pp. 1027–1035, 2004.

[68] J. Y. Kang, B. I. Choi, and H. J. Lee, "Application of Artificial Neural Network for Predicting Plane Strain Fracture Toughness Using Tensile Test Results," *Fatigue & Fracture of Engineering Materials & Structures*, vol. 29, no. 4, pp. 321–329, 2006.

[69] M. Janezic, J. Klemenc, and M. Fajdiga, "A Neural-Network Approach to Describe the Scatter of Cyclic StressStrain Curves," *Materials and Design*, vol. 31, pp. 438–448, 2009.

[70] K. Hornik, M. Stinchcombe, and H. White, "Multilayer Feedforward Networks are Universal Approximators," *Neural Networks*, vol. 2, no. 5, pp. 359 – 366, 1989.

[71] "Matlab v. r2010b," The MathWorks: Natick, MA. 2010.

[72] N. E. Dowling, *Mechanical Behavior of Materials*. Prentice Hall, 1 ed., 1993.

[73] G. P. Zhang, "Avoiding Pitfalls in Neural Network Research," *Systems, Man, and Cybernetics, Part C: Applications and Reviews, IEEE Transactions on*, vol. 37, no. 1, pp. 3–16, 2007.

[74] D. E. Rumelhart, G. E. Hinton, and R. J. Williams, "Learning Representations by Back-Propagating Errors.," *Nature*, vol. 323, no. 6088, pp. 533 – 536, 1986.

[75] D. Mackay, "Bayesian Interpolation," *Neural Computation*, vol. 4, no. 3, pp. 415 – 447, 1992.

[76] J. Smrekar, M. Assadi, M. Fast, I. Ku °trin, and S. De, "Development of Artificial Neural Network Model for a Coal-Fired Boiler Using Real Plant Data," *Energy*, vol. 34, no. 2, pp. 144–152, 2009.

[77] P. B. Cachim, "Using Artificial Neural Networks for Calculation of Temperatures in Timber Under Fire Loading," *Construction and Building Materials*, vol. 25, no. 11, pp. 4175–4180, 2011.

[78] M. Klesnil and P. Luk, *Fatigue of Metallic Materials / Mirko Klesnil and Petr Luk.* Materials science monographs: v. 7, Amsterdam ; New York : Elsevier Scientific Pub. Co. ; New York : distribution for the U.S.A. and Canada, Elsevier/North Holland, 1980., 1980.

[79] N. Hong and L. Shaobo, "Biaxial Stress Fatigue Life Prediction by the Local Strain Method.," *International Journal of Fatigue*, vol. 19, no. 6, pp. 517 – 522, 1997.

[80] P. Ferreira, J. Pinho-da Cruz, and F. Teixeira-Dias, "Finite Element and Local Strain Approach Stress-Strain Predictions in Notched AlCu4.5Mn Specimens (portuguese).," *Iberoamerican Journal of Engineering Mechanics*, vol. 10, no. 1, p. 93, 2006.

[81] N. Dowling, W. Brose, and W. Wilson, "Notched Member Fatigue Life Predictions by the Local Strain Approach.," *Adv. Eng. Fatigue Under Complex Loading*, vol. 6, pp. 55 – 84, 1977.